Testing the Predictive Capability of the High-Fidelity Generalized Method of Cells Using an Efficient Reformulation

Yogesh Bansal and Marek-Jerzy Pindera
University of Virginia, Charlottesville, Virginia

The NASA STI Program Office . . . in Profile

Since its founding, NASA has been dedicated to the advancement of aeronautics and space science. The NASA Scientific and Technical Information (STI) Program Office plays a key part in helping NASA maintain this important role.

The NASA STI Program Office is operated by Langley Research Center, the Lead Center for NASA's scientific and technical information. The NASA STI Program Office provides access to the NASA STI Database, the largest collection of aeronautical and space science STI in the world. The Program Office is also NASA's institutional mechanism for disseminating the results of its research and development activities. These results are published by NASA in the NASA STI Report Series, which includes the following report types:

- TECHNICAL PUBLICATION. Reports of completed research or a major significant phase of research that present the results of NASA programs and include extensive data or theoretical analysis. Includes compilations of significant scientific and technical data and information deemed to be of continuing reference value. NASA's counterpart of peer-reviewed formal professional papers but has less stringent limitations on manuscript length and extent of graphic presentations.

- TECHNICAL MEMORANDUM. Scientific and technical findings that are preliminary or of specialized interest, e.g., quick release reports, working papers, and bibliographies that contain minimal annotation. Does not contain extensive analysis.

- CONTRACTOR REPORT. Scientific and technical findings by NASA-sponsored contractors and grantees.

- CONFERENCE PUBLICATION. Collected papers from scientific and technical conferences, symposia, seminars, or other meetings sponsored or cosponsored by NASA.

- SPECIAL PUBLICATION. Scientific, technical, or historical information from NASA programs, projects, and missions, often concerned with subjects having substantial public interest.

- TECHNICAL TRANSLATION. English-language translations of foreign scientific and technical material pertinent to NASA's mission.

Specialized services that complement the STI Program Office's diverse offerings include creating custom thesauri, building customized databases, organizing and publishing research results . . . even providing videos.

For more information about the NASA STI Program Office, see the following:

- Access the NASA STI Program Home Page at *http://www.sti.nasa.gov*

- E-mail your question via the Internet to help@sti.nasa.gov

- Fax your question to the NASA Access Help Desk at 301–621–0134

- Telephone the NASA Access Help Desk at 301–621–0390

- Write to:
  NASA Access Help Desk
  NASA Center for AeroSpace Information
  7121 Standard Drive
  Hanover, MD 21076

NASA/CR—2004-213043

Testing the Predictive Capability of the High-Fidelity Generalized Method of Cells Using an Efficient Reformulation

Yogesh Bansal and Marek-Jerzy Pindera
University of Virginia, Charlottesville, Virginia

National Aeronautics and
Space Administration

Glenn Research Center

April 2004

Acknowledgments

Testing the Predictive Capability of the High-Fidelity Generalized Method of Cells Using an Efficient Reformulation

Yogesh Bansal and Marek-Jerzy Pindera
University of Virginia
Charlottesville, VA 22904

Abstract

The High-Fidelity Generalized Method of Cells is a new micromechanics model for unidirectionally reinforced periodic multiphase materials that was developed to overcome the shortcomings of the original Generalized Method of Cells. The high-fidelity version combines the basic elements of the *higher-order theory for functionally graded materials* with the *homogenization theory* framework, together with a volume discretization approach similar to that employed in the original model. The use of a higher-order displacement field approximation in the individual subcells of a repeating unit cell representative of a periodic material provides the necessary shear coupling absent in the original model, which in turn dramatically improves the accuracy of the local stress and strain fields and, in certain cases, the effective moduli. Herein, we test the predictive capability of the high-fidelity model in estimating the elastic moduli of periodic composites characterized by repeating unit cells obtained by rotation of an infinite square fiber array through an angle about the fiber axis. Such repeating unit cells, which typically possess no apparent planes of material symmetry, may contain a few or many fibers, depending on the rotation angle. In order to analyze such multi-inclusion repeating unit cells efficiently, the high-fidelity micromechanics model's framework is reformulated using the approach previously employed by the authors in reformulating the higher-order theory for functionally graded materials. The excellent agreement with the corresponding results obtained from the standard transformation equations confirms the new model's predictive capability for a class of periodic composites characterized by non-standard, multi-inclusion repeating unit cells lacking planes of material symmetry. Comparison of the effective moduli and local stress fields with the corresponding results obtained from the original Generalized Method of Cells confirms the need for the new high-fidelity model, and dramatically highlights the original model's shortcomings for a certain class of unidirectional composites.

1 Introduction

Micromechanical modeling techniques make it possible to efficiently analyze, relative to the actual synthesis and experimental characterization of new material designs, the manner in which different microstructural details affect the average and local responses of multiphase materials. This is important in the development of optimum material architectures for specific applications which may require many iterations. Many micromechanical techniques have been developed during the past several decades and these include simple Voigt and Reuss hypotheses, self-consistent schemes and their generalizations, differential schemes, concentric cylinder models, bounding techniques, and approximate or numerical analyses of periodic arrays of inclusions or fibers in the surrounding matrix phase (see, for instance, the monographs by Christensen [1], Aboudi [2], Nemat-Nasser and Hori [3], Kalamkarov and Kolpakov [4], and Markov and Preziosi [5]).

The Generalized Method of Cells (GMC) is an approximate micromechanical model for the response of multiphase periodic composites in the elastic and inelastic regimes. It was originally developed by Paley and Aboudi [6] using the original Method of Cells proposed by Aboudi [2] as a basis, and subsequently extended by Aboudi and others (cf. review article by Aboudi [7]). GMC has been made computationally efficient by Pindera and Bednarcyk [8] for unidirectionally reinforced composites, and by Bednarcyk and Pindera [9] for composites with three-dimensional reinforcement, through reformulations which take advantage of the method's lack of shear coupling discussed in more detail below. These reformulated versions, which provide the enabling technology for efficient analysis of periodic composites with detailed (i.e. realistic) microstructural representation, are currently employed in NASA's software called **MAC/GMC** [10].

GMC is based on a geometric model of a rectangular repeating unit cell representative of the modeled multiphase material's periodic microstructure. To mimic the given microstructure, the repeating unit cell is discretized into subcells wherein the displacement field is approximated by a linear representation based on local coordinates centered at the subcell's midpoint. An averaging procedure that involves the enforcement of interfacial displacement and traction continuity conditions between the individual subcells applied in a surface-average sense, and periodicity conditions between adjacent repeating unit cells, establishes the effective or homogenized properties of the composite in terms of Hill's strain concentration factors [11], and geometric and material properties of the individual subcells.

As demonstrated in previous studies on unidirectional metal matrix composites, GMC is typically quite accurate at the macro-level under most (but not all) loading situations, but generally not very accurate at the micro-level. This is due to the absence of so-called shear coupling which provides the required bridge between macroscopically applied normal (shear) stresses and the resulting microscopic shear (normal) stresses necessary for an accurate estimate of micro-level quantities. This absence is due to the linear displacement field approximation within each subcell, which produces constant strain and stress fields, and also to the manner of applying traction continuity

conditions in a surface-average sense at the interfaces separating adjacent subcells. This leads to constant traction components along the rows and columns of the repeating unit cell, resulting in inaccurate local stress fields. Despite this limitation, GMC and its earlier version have been successfully employed to predict the initial yield surfaces and subsequent macroscopic response of unidirectional metal matrix composites under different types of loading and with different fiber arrays characterized by material planes of symmetry (cf. Pindera and Aboudi [12], Pindera et al. [13], and Arnold et al. [14] for earlier investigations, and more recently Iyer et al. [15] and Arnold et al. [16]). As demonstrated by Arnold et al. [14] and Iyer et al. [15], the success of GMC in predicting the response of metal matrix composites with relatively small constituent elastic moduli mismatch is its ability to reproduce with reasonable accuracy the second stress deviator which controls the evolution of inelastic strains in the matrix phase, despite poor estimates of the individual stress components. The computational efficiency of the reformulated GMC makes it an attractive tool for stand-alone applications as well as applications which utilize GMC as a subroutine in large-scale structural mechanics analyses, provided that the method is employed within its limits of applicability and its limitations are recognized as discussed below.

There are several consequences of the shear-coupling's absence which must be recognized. First, the constant tractions within each row and column of subcells, which result from the application of traction continuity at the interfaces separating adjacent subcells in a surface-average sense, dictate that the greatest normal or shear traction component in the pertinent direction is directly influenced by the most compliant subcell. If the modulus of such subcell happens to be zero, as may occur in the presence of porosity, then the normal/shear traction associated with the unit normal along the direction of travel will be zero, rendering the row/column containing this subcell ineffective in supporting the load. The normal/shear stress re-introduction into such row/column of subcells does not occur precisely because of the absence of shear coupling (in contrast to the shear lag-type analysis employed to explain the re-introduction of load into a broken fiber away from its ends). In particular, the presence of porosity however small in a given plane of subcells ensures that the transverse shear stress cannot be supported in the entire plane. Thus for a unidirectional composite with a unidirectional porosity in place of a fiber, the transverse shear modulus will be zero according to GMC. The same anomaly occurs in the presence of a disbond across an interface separating two subcells. The above arguments obviously carry over to subcells with very small moduli relative to other subcells. Modeling the response of unidirectional composites with debonded fiber/matrix interfaces, discontinuous fiber composites as well as woven composites using GMC requires special modifications which mitigate the absence of shear coupling, as recently discussed by Bednarcyk and Arnold [17], Pahr and Arnold [18], and Bednarcyk and Arnold [19]. Alternatively, a new but more computationally demanding model discussed below, which is also available in **MAC/GMC**, can be employed to circumvent the above limitations, Bednarcyk and Arnold [10].

Further, GMC-based analysis of repeating unit cells that do not have two orthogonal planes of material symmetry aligned with the cell's coordinate system in the investigated plane is not admis-

sible. This is because GMC cannot accommodate material microstructures leading to anisotropic effective properties when the individual phases are orthotropic or isotropic. At most, orthotropic effective properties can be predicted which require planes of material symmetry when the individual phases are orthotropic/isotropic. This is also a direct result of the absence of shear coupling in the formulation. Anisotropic effective properties are predicted only when the individual phases are anisotropic. Analysis of repeating unit cells that lack planes of material symmetry erroneously produces orthotropic properties and therefore is not admissible. We note that this shortcoming has been disregarded by some authors, particularly when applying the method to periodic composites with locally irregular microstructures. This is only valid in a very approximate sense for a sufficient number of inclusions of similar dimensions within the repeating unit cell which produce isotropic effective properties in the plane transverse to the reinforcement direction, Orozco [20].

In order to overcome the above shortcomings, a new micromechanics model has been developed recently by Aboudi et al. [21,22,23] for the response of multiphase materials with arbitrary periodic microstructures, named High-Fidelity Generalized Method of Cells (HFGMC) in part because it employs a similar volume discretization as the original GMC. The model's analytical framework is based on the homogenization theory, but the method of solution for the local displacement and stress fields within the repeating unit cell utilizes concepts previously employed in constructing the higher-order theory for functionally graded materials [24]. The homogenization theory is used to construct a higher-order displacement field approximation at the local microstructural level of a periodic multiphase material in a consistent fashion, and to derive the governing field equations and the boundary conditions that the displacement field must satisfy. The actual solution for the local displacement, strain and stress fields follows the above-mentioned higher-order theory. The higher-order displacement field approximation at the local level provides the necessary coupling between the local normal and shear stress fields and the macroscopically applied loading. This coupling dramatically improves the accuracy of estimating the local stress fields relative to GMC, as previously demonstrated for simple periodic microstructures characterized by orthogonal planes of material symmetry through exact analytical and numerical solutions [21,22,23]. It also enables accurate analysis of unidirectional metal matrix composites in the presence of debonded fiber/matrix interfaces in a direct manner, Bednarcyk et al. [25], in contrast with the special modifications introduced into GMC mentioned earlier [17]. Limited data also has been generated for unidirectional composites with locally irregular microstructures using HFGMC, Pindera et al. [26]. It is for such composites that the power of HFGMC becomes evident due to the importance of shear coupling in the presence of locally irregular microstructures as demonstrated by the above study, further highlighting the differences between the two models' predictive capabilities.

Given the past experience, it is expected that the shear-coupling effect will play a key role in correctly capturing the elastic moduli of unidirectional composites with repeating unit cells that lack orthogonal planes of material symmetry due to rotation about the fiber axis, rather than locally irregular microstructural arrangement. Therefore, HFGMC is employed herein to determine the

effective moduli and local stress fields in unidirectional composites characterized by a repeating unit cell with a square fiber array loaded by average stresses that do not coincide with the orthogonal planes of material symmetry. Such a situation arises when a unidirectionally reinforced composite is rotated by an angle about the fiber axis. The repeating unit cell for a particular rotation angle typically may contain a large number of fibers (in contrast with just one for the square array), which makes HFGMC computationally expensive due to large number of rectangular subcells required to model realistic geometric details (such as circular fibers, for instance). Therefore, in order to enable modeling of such multi-inclusion repeating unit cells in sufficient detail, the theoretical framework of the HFGMC micromechanical model is reformulated using the local/global stiffness matrix approach originally proposed by Bufler [27] for the elastic analysis of isotropic layered media, and extended by Pindera [28] to layered anisotropic composites. The same approach has been employed by Bansal and Pindera [29] in reformulating the original higher-order theory for functionally graded materials, resulting in substantial reduction in the governing system of equations.

The predictions of the reformulated HFGMC model for the elastic moduli of two types of unidirectional composites as a function of the rotation angle are compared with the results obtained from the transformation equations for an elastic stiffness matrix of an orthotropic material rotated by an angle about the fiber axis. Such rotation produces an elastic stiffness matrix in the rotated coordinate system that represents a monoclinic material with just one plane of material symmetry (the plane perpendicular to the fiber axis). This provides a critical test on the self-consistency of the newly developed HFGMC model previously untested in this manner. Comparison with the corresponding GMC predictions are also provided to further justify the development of the new model. Towards this end, two types of unidirectional composites with the same inclusion content have been employed in this investigation which are characterized by radically different fiber/matrix moduli ratios representative of a glass/epoxy system and a porous aluminum matrix.

2   Theoretical Framework of the High-Fidelity GMC Model

The theoretical framework of the original version of the High-Fidelity Generalized Method of Cells has been described in detail by Aboudi et al. [21,22,23], and thus only a brief synthesis will be provided herein in order to make it possible to follow the efficient reformulation's derivation. The high-fidelity model combines concepts from the homogenization theory and the higher-order theory for functionally graded materials. The homogenization theory is employed to construct the correct form of the displacement field representation in the discretized domains of the repeating unit cell which represents the periodic material's microstructure; to identify the governing field equations for the local problem of the repeating unit cell; and to construct appropriate boundary conditions. The construction of the displacement field is based on a two-scale expansion of the form:

$$u_i(\mathbf{x}, \mathbf{y}) = u_{0i}(\mathbf{x}, \mathbf{y}) + \delta u_{1i}(\mathbf{x}, \mathbf{y}) + \delta^2 u_{2i}(\mathbf{x}, \mathbf{y}) + ... \tag{1}$$

where $\mathbf{x} = (x_1, x_2, x_3)$ are the global or macroscopic coordinates, $\mathbf{y} = (y_1, y_2, y_3)$ are the local or microscopic coordinates defined with respect to the repeating unit cell, and the different order terms characterized by the powers of δ are $\mathbf{y}$-periodic due to the material's periodicity. The size of the repeating unit cell characterized by the parameter δ is small relative to the overall material dimensions such that $y_i = x_i/\delta$. This suggests that a unit displacement at the local scale corresponds to a displacement on the global scale of the order of δ.

The above displacement field representation, together with the relation $y_i = x_i/\delta$ between the two spatial scales, leads to the following strain field decomposition for periodic materials given in terms of the average and fluctuating strains $\bar{\varepsilon}_{ij}(\mathbf{x})$ and $\varepsilon'_{ij}(\mathbf{x}, \mathbf{y})$, respectively

$$\varepsilon_{ij} = \bar{\varepsilon}_{ij}(\mathbf{x}) + \varepsilon'_{ij}(\mathbf{x}, \mathbf{y}) + \mathbf{O}(\delta) \tag{2}$$

The average and fluctuating (local) strains are derived from the corresponding displacement components $\bar{u}_i$ and u'_i

$$\bar{\varepsilon}_{ij}(\mathbf{x}) = \frac{1}{2}(\frac{\partial \bar{u}_i}{\partial x_j} + \frac{\partial \bar{u}_j}{\partial x_i}), \qquad \varepsilon'_{ij}(\mathbf{x}, \mathbf{y}) = \frac{1}{2}(\frac{\partial u'_i}{\partial y_j} + \frac{\partial u'_j}{\partial y_i}) \tag{3}$$

The above strain decomposition makes it possible to express the displacement field in the form

$$u_i(\mathbf{x}, \mathbf{y}) = \bar{\varepsilon}_{ij} x_j + u'_i + \mathbf{O}(\delta^2) \tag{4}$$

where $\bar{\varepsilon}_{ij}$ are the known or applied macroscopic strains. This form is employed in constructing an approximate displacement field for the solution of the cell problem following the methodology of the reformulated higher-order theory for functionally graded materials.

For specified values of the average strains, the unknown fluctuating displacements must satisfy the local stress equilibrium equations subject to periodic boundary conditions imposed on the displacement and traction components that are prescribed at the boundaries of the repeating unit cell. In addition to these boundary conditions, it is also necessary to impose the continuity of displacements and tractions at the internal interfaces between the phases within the repeating unit cell. The manner of determining the fluctuating displacements in the repeating unit cell follows the methodology employed in the higher-order theory for functionally graded materials. The solution is based on satisfying the local stress equilibrium equations in a volumetric sense in the individual subvolumes into which the repeating unit cell is discretized in a manner that mimics the actual microstructure of the periodic multiphase material. In addition, the interfacial displacement and traction continuity conditions are imposed in a surface-average sense at the interfaces separating the individual subvolumes, as are the periodic boundary conditions.

In the original formulation of the high-fidelity theory, a two-level discretization of the repeating unit cell's microstructure was used, involving division into generic cells which were further subdivided into four subcells in the case of periodic materials with continuous reinforcement along a common direction. This two-level discretization process, based on the volume discretization

employed in the original version of the higher-order theory for functionally graded materials, unnecessarily complicated the derivation of the volume-averaged stress equilibrium equations, which were obtained in a circuitous manner by satisfying the different moments of the equilibrium equations. These manipulations, in turn, suggested that the higher-order theory is a variant of a micropolar, micromechanics-based continuum theory, which is not the case. The derivation of the traction continuity conditions between adjacent generic cells was also complicated by the two-level discretization of the repeating unit cell.

The reformulation of the higher-order theory was based on a single-step discretization process involving only subcells as the fundamental building blocks of a functionally graded material's microstructure. This simplification facilitated the construction of a local stiffness matrix relating the surface-averaged displacements to the corresponding surface-averaged tractions of the subcell, with the surface-averaged displacements becoming the fundamental unknown quantities. As a result, the number of equations governing the micro-level displacement and stress fields within the graded material was reduced by as much as 60% upon assembly of the individual local stiffness matrices into the global stiffness matrix [29]. Furthermore, the reformulation simplified the derivation of the governing equations and revealed the higher-order theory to be an approximate elasticity technique involving direct volume-averaging of the stress equilibrium equations in conjunction with the imposition of displacement and traction continuity conditions in a surface-average sense across adjacent subcell faces. Herein, the same approach is employed in reformulating the solution for the local problem of the repeating unit cell within the High-Fidelity GMC framework.

3 Efficient Reformulation of the Cell Problem

The local analysis is performed on the repeating unit cell representative of a periodic material's microstructure in the $x_2 - x_3$ plane, Fig. 1(a), and characterized by continuous reinforcement along the x_1 axis. The periodic microstructure is made up of any number of phases arbitrarily distributed within the repeating unit cell so as to produce fully anisotropic behavior in the $x_2 - x_3$ plane. The repeating unit cell is appropriately discretized into subcells, designated by (β, γ), so as to mimic the material's periodic microstructure, as shown in Fig. 1(b) for the repeating unit cell highlighted in Fig. 1(a). In this case, 100×100 equally dimensioned subcells were used to capture the three reinforcement shapes with sufficient fidelity, noting that such refinement would have been computationally prohibitive in the original formulation. The indices $\beta = 1, ..., N_\beta$ and $\gamma = 1, ..., N_\gamma$, which span the repeating unit cell dimensions along the y_2 and y_3 axes, identify the (β, γ) subcell in the $y_2 - y_3$ plane. The subcell dimensions along the y_2 and y_3 axes are h_β and l_γ, respectively, such that

$$H = \sum_{\beta=1}^{N_\beta} h_\beta \quad \text{and} \quad L = \sum_{\gamma=1}^{N_\gamma} l_\gamma$$

where H and L are the overall repeating unit cells dimensions along these axes.
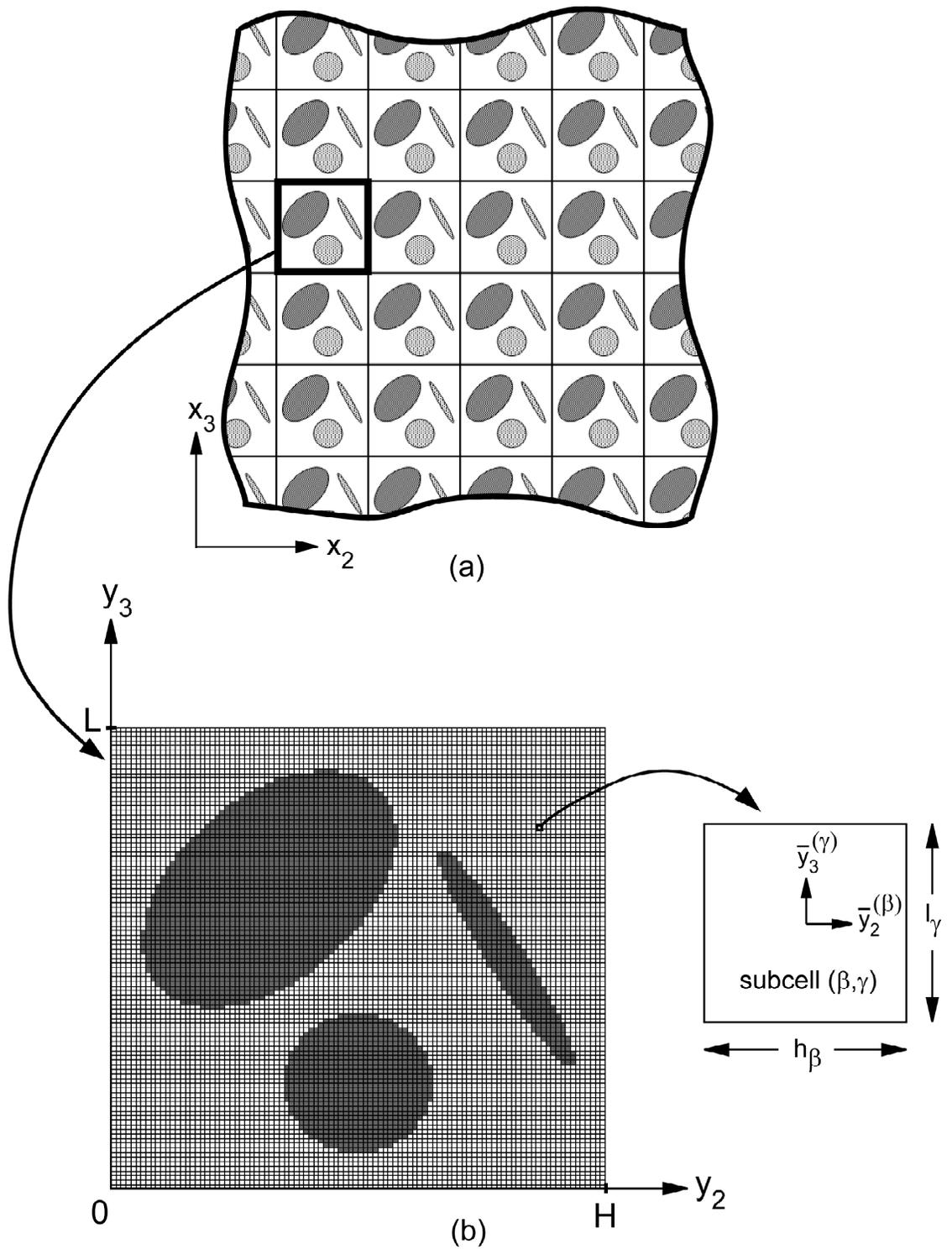
Figure 1. (a) A continuously reinforced multiphase composite with a periodic microstructure in the $x_2 - x_3$ plane constructed with repeating unit cells, (b) discretization of the repeating unit cell into subcells employed in the reformulation of the High-Fidelity GMC.

Following the displacement field representation within the repeating unit cell of a periodic material given by Eq. (4), the displacement field in each (β, γ) subcell is written as follows

$$u_i^{(\beta,\gamma)} = \bar{\varepsilon}_{ij} x_j + u_i'^{(\beta,\gamma)} \tag{5}$$

The fluctuating components $u_i'^{(\beta,\gamma)}$ of the displacement field arise due to the heterogeneity of the medium and are a function of the microscopic (local) coordinates $\bar{\mathbf{y}}^{(\beta,\gamma)} = (\bar{y}_2^{(\beta)}, \bar{y}_3^{(\gamma)})$ attached to the subcell's center as shown in Fig. 1(b). These fluctuating components are approximated in each (β, γ) subcell by the same second-order, Legendre-type polynomial expansion in the local coordinates as that employed in the original formulation

$$
\begin{aligned}
u_i'^{(\beta,\gamma)} &= W_{i(00)}^{(\beta,\gamma)} + \bar{y}_2^{(\beta)} W_{i(10)}^{(\beta,\gamma)} + \bar{y}_3^{(\gamma)} W_{i(01)}^{(\beta,\gamma)} + \\
&\quad \frac{1}{2}(3\bar{y}_2^{(\beta)2} - \frac{h_\beta^2}{4}) W_{i(20)}^{(\beta,\gamma)} + \frac{1}{2}(3\bar{y}_3^{(\gamma)2} - \frac{l_\gamma^2}{4}) W_{i(02)}^{(\beta,\gamma)} \qquad i = 1, 2, 3
\end{aligned} \tag{6}
$$

where $W_{i(mn)}^{(\beta,\gamma)}$ are the unknown microvariables associated with each subcell. Using the above fluctuating field representation, the strain components in each (β, γ) subcell are derived from

$$\varepsilon_{ij}^{(\beta,\gamma)} = \bar{\varepsilon}_{ij} + \frac{1}{2}\left(\frac{\partial u_i'^{(\beta,\gamma)}}{\partial \bar{y}_j^{(\cdot)}} + \frac{\partial u_j'^{(\beta,\gamma)}}{\partial \bar{y}_i^{(\cdot)}}\right) \tag{7}$$

in the form

$$
\begin{aligned}
\varepsilon_{11}^{(\beta,\gamma)} &= \bar{\varepsilon}_{11} \\
\varepsilon_{22}^{(\beta,\gamma)} &= \bar{\varepsilon}_{22} + W_{2(10)}^{(\beta,\gamma)} + 3\bar{y}_2^{(\beta)} W_{2(20)}^{(\beta,\gamma)} \\
\varepsilon_{33}^{(\beta,\gamma)} &= \bar{\varepsilon}_{33} + W_{3(01)}^{(\beta,\gamma)} + 3\bar{y}_3^{(\gamma)} W_{3(02)}^{(\beta,\gamma)} \\
\varepsilon_{12}^{(\beta,\gamma)} &= \bar{\varepsilon}_{12} + \frac{1}{2}[W_{1(10)}^{(\beta,\gamma)} + 3\bar{y}_2^{(\beta)} W_{1(20)}^{(\beta,\gamma)}] \\
\varepsilon_{13}^{(\beta,\gamma)} &= \bar{\varepsilon}_{13} + \frac{1}{2}[W_{1(01)}^{(\beta,\gamma)} + 3\bar{y}_3^{(\gamma)} W_{1(02)}^{(\beta,\gamma)}] \\
\varepsilon_{23}^{(\beta,\gamma)} &= \bar{\varepsilon}_{23} + \frac{1}{2}[W_{2(01)}^{(\beta,\gamma)} + 3\bar{y}_3^{(\gamma)} W_{2(02)}^{(\beta,\gamma)} + W_{3(10)}^{(\beta,\gamma)} + 3\bar{y}_2^{(\beta)} W_{3(20)}^{(\beta,\gamma)}]
\end{aligned} \tag{8}
$$

Using the above relations in the Hooke's law for an orthotropic elastic (β, γ) subcell

$$\sigma_{ij}^{(\beta,\gamma)} = C_{ijkl}^{(\beta,\gamma)} \varepsilon_{kl}^{(\beta,\gamma)} \tag{9}$$

the subcell stress components are then expressed in terms of the unknown microvariables $W_{i(mn)}^{(\beta,\gamma)}$ and the applied macroscopic strains $\bar{\varepsilon}_{ij}$. For an orthotropic subcell, the stiffness tensor elements $C_{ijkl}^{(\beta,\gamma)}$ are characterized by nine independent components in the material principal coordinate system formed by the intersections of three orthogonal planes of material symmetry.

In the original formulation, the unknown microvariables $W_{i(mn)}^{(\beta,\gamma)}$ were determined by satisfying the local stress equilibrium equations in a volumetric sense, and the displacement and traction

continuity conditions between subcells and generic cells, together with the periodic boundary conditions, in a surface-average sense. In the reformulation, the surface-averaged fluctuating displacement components become the fundamental unknowns which are related to the surface-averaged tractions through a local subcell matrix constructed in the manner described below.

3.1 Local Stiffness Matrix

The local stiffness matrix for each (β, γ) subcell is constructed by first expressing the tractions defined at the subcell's outer faces in terms of stresses through Cauchy's relations

$$t_i^{\mathbf{n}(\beta,\gamma)} = \sigma_{ji}^{(\beta,\gamma)} n_j^{(\beta,\gamma)} \tag{10}$$

where $n_j^{(\beta,\gamma)}$ are components of the unit normal to a given face of the (β, γ) subcell. The surface-averaged tractions $\bar{\mathbf{t}}^{(\beta,\gamma)}$ are defined at the outer faces of the subcell in the following manner

$$\bar{\mathbf{t}}^{(\beta,\gamma)} = [\bar{t}_1^{2+}, \bar{t}_1^{2-}, \bar{t}_2^{2+}, \bar{t}_2^{2-}, \bar{t}_3^{2+}, \bar{t}_3^{2-}, \bar{t}_1^{3+}, \bar{t}_1^{3-}, \bar{t}_2^{3+}, \bar{t}_2^{3-}, \bar{t}_3^{3+}, \bar{t}_3^{3-}]^{(\beta,\gamma)} \tag{11}$$

where

$$\bar{t}_i^{2\pm(\beta,\gamma)} = \frac{1}{l_\gamma} \int_{-l_\gamma/2}^{l_\gamma/2} t_i^{\mathbf{n}(\beta,\gamma)}(\pm\frac{h_\beta}{2}, \bar{y}_3^{(\gamma)})d\bar{y}_3^{(\gamma)} \tag{12}$$

$$\bar{t}_i^{3\pm(\beta,\gamma)} = \frac{1}{h_\beta} \int_{-h_\beta/2}^{h_\beta/2} t_i^{\mathbf{n}(\beta,\gamma)}(\bar{y}_2^{(\beta)}, \pm\frac{l_\gamma}{2})d\bar{y}_2^{(\beta)} \qquad i = 1, 2, 3 \tag{13}$$

and $j\pm$ $(j = 2, 3)$ denotes the direction of the normal to the positive (+) or negative (-) face of the (β, γ) subcell, Fig. 2.

$$\bar{\mathbf{t}}^{3+} = \begin{bmatrix} \bar{t}_1^{3+} \\ \bar{t}_2^{3+} \\ \bar{t}_3^{3+} \end{bmatrix}, \quad \bar{\mathbf{u}}^{3+} = \begin{bmatrix} \bar{u}_1^{3+} \\ \bar{u}_2^{3+} \\ \bar{u}_3^{3+} \end{bmatrix}$$

$$\bar{\mathbf{t}}^{2+} = \begin{bmatrix} \bar{t}_1^{2+} \\ \bar{t}_2^{2+} \\ \bar{t}_3^{2+} \end{bmatrix}, \quad \bar{\mathbf{u}}^{2+} = \begin{bmatrix} \bar{u}_1^{2+} \\ \bar{u}_2^{2+} \\ \bar{u}_3^{2+} \end{bmatrix}$$
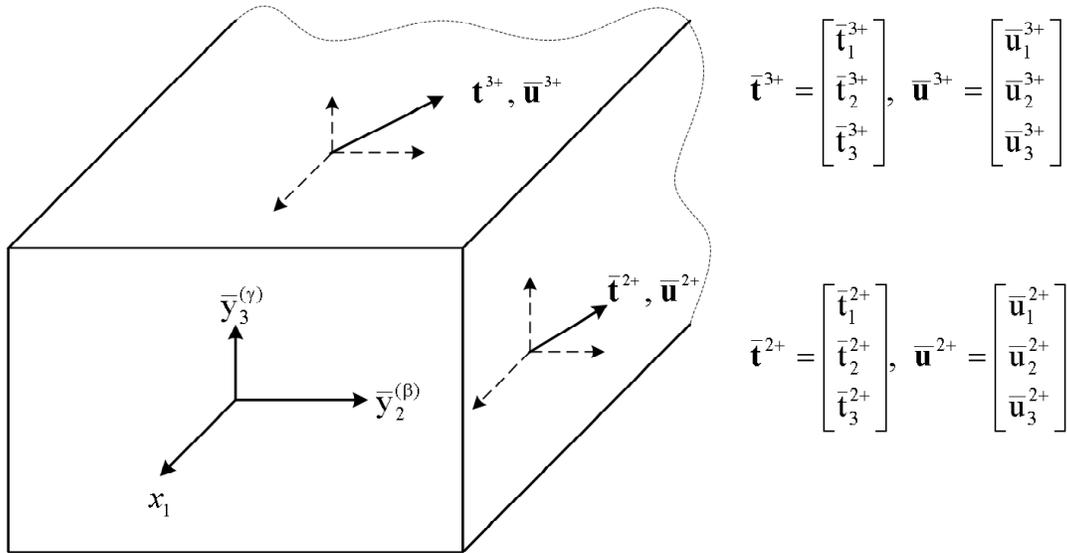
Figure 2. A view of a subcell illustrating the convention employed in designating the surface-averaged displacement and traction components employed in the reformulation.

Substituting Eqs. $(8)-(10)$ into Eqs. $(12)-(13)$, performing the required integration and assembling the resulting equations in matrix form, we obtain

$$\begin{bmatrix} \bar{t}_1^{2+} \\ \bar{t}_1^{2-} \end{bmatrix}^{(\beta,\gamma)} = C_{66}^{(\beta,\gamma)} \begin{bmatrix} 1 & \frac{3h_\beta}{2} \\ -1 & \frac{3h_\beta}{2} \end{bmatrix} \begin{bmatrix} W_{1(10)} \\ W_{1(20)} \end{bmatrix}^{(\beta,\gamma)} + 2C_{66}^{(\beta,\gamma)} \begin{bmatrix} \bar{\varepsilon}_{12} \\ -\bar{\varepsilon}_{12} \end{bmatrix} \tag{14}$$

$$\begin{bmatrix} \bar{t}_1^{3+} \\ \bar{t}_1^{3-} \end{bmatrix}^{(\beta,\gamma)} = C_{55}^{(\beta,\gamma)} \begin{bmatrix} 1 & \frac{3l_\gamma}{2} \\ -1 & \frac{3l_\gamma}{2} \end{bmatrix} \begin{bmatrix} W_{1(01)} \\ W_{1(02)} \end{bmatrix}^{(\beta,\gamma)} + 2C_{55}^{(\beta,\gamma)} \begin{bmatrix} \bar{\varepsilon}_{13} \\ -\bar{\varepsilon}_{13} \end{bmatrix} \tag{15}$$

$$\begin{bmatrix} \bar{t}_2^{2+} \\ \bar{t}_2^{2-} \end{bmatrix}^{(\beta,\gamma)} = C_{22}^{(\beta,\gamma)} \begin{bmatrix} 1 & \frac{3h_\beta}{2} \\ -1 & \frac{3h_\beta}{2} \end{bmatrix} \begin{bmatrix} W_{2(10)} \\ W_{2(20)} \end{bmatrix}^{(\beta,\gamma)} + C_{23}^{(\beta,\gamma)} \begin{bmatrix} W_{3(01)} \\ -W_{3(01)} \end{bmatrix}^{(\beta,\gamma)} + \sum_{i=1}^{3} C_{i2}^{(\beta,\gamma)} \begin{bmatrix} \bar{\varepsilon}_{ii} \\ -\bar{\varepsilon}_{ii} \end{bmatrix} \tag{16}$$

$$\begin{bmatrix} \bar{t}_3^{2+} \\ \bar{t}_3^{2-} \end{bmatrix}^{(\beta,\gamma)} = C_{44}^{(\beta,\gamma)} \begin{bmatrix} 1 & \frac{3h_\beta}{2} \\ -1 & \frac{3h_\beta}{2} \end{bmatrix} \begin{bmatrix} W_{3(10)} \\ W_{3(20)} \end{bmatrix}^{(\beta,\gamma)} + C_{44}^{(\beta,\gamma)} \begin{bmatrix} W_{2(01)} \\ -W_{2(01)} \end{bmatrix}^{(\beta,\gamma)} + 2C_{44}^{(\beta,\gamma)} \begin{bmatrix} \bar{\varepsilon}_{23} \\ -\bar{\varepsilon}_{23} \end{bmatrix} \tag{17}$$

$$\begin{bmatrix} \bar{t}_2^{3+} \\ \bar{t}_2^{3-} \end{bmatrix}^{(\beta,\gamma)} = C_{44}^{(\beta,\gamma)} \begin{bmatrix} 1 & \frac{3l_\gamma}{2} \\ -1 & \frac{3l_\gamma}{2} \end{bmatrix} \begin{bmatrix} W_{2(01)} \\ W_{2(02)} \end{bmatrix}^{(\beta,\gamma)} + C_{44}^{(\beta,\gamma)} \begin{bmatrix} W_{3(10)} \\ -W_{3(10)} \end{bmatrix}^{(\beta,\gamma)} + 2C_{44}^{(\beta,\gamma)} \begin{bmatrix} \bar{\varepsilon}_{23} \\ -\bar{\varepsilon}_{23} \end{bmatrix} \tag{18}$$

$$\begin{bmatrix} \bar{t}_3^{3+} \\ \bar{t}_3^{3-} \end{bmatrix}^{(\beta,\gamma)} = C_{33}^{(\beta,\gamma)} \begin{bmatrix} 1 & \frac{3l_\gamma}{2} \\ -1 & \frac{3l_\gamma}{2} \end{bmatrix} \begin{bmatrix} W_{3(01)} \\ W_{3(02)} \end{bmatrix}^{(\beta,\gamma)} + C_{23}^{(\beta,\gamma)} \begin{bmatrix} W_{2(10)} \\ -W_{2(10)} \end{bmatrix}^{(\beta,\gamma)} + \sum_{i=1}^{3} C_{i3}^{(\beta,\gamma)} \begin{bmatrix} \bar{\varepsilon}_{ii} \\ -\bar{\varepsilon}_{ii} \end{bmatrix} \tag{19}$$

Equations $(14)-(19)$ relate the surface-averaged tractions to the first- and second-order microvariables. Next, we express the microvariables $W_{i(mn)}^{(\beta,\gamma)}$ in terms of the fluctuating surface-averaged displacements $\bar{\mathbf{u}}'^{(\beta,\gamma)}$

$$\bar{\mathbf{u}}'^{(\beta,\gamma)} = [\bar{u}_1'^{2+}, \bar{u}_1'^{2-}, \bar{u}_2'^{2+}, \bar{u}_2'^{2-}, \bar{u}_3'^{2+}, \bar{u}_3'^{2-}, \bar{u}_1'^{3+}, \bar{u}_1'^{3-}, \bar{u}_2'^{3+}, \bar{u}_2'^{3-}, \bar{u}_3'^{3+}, \bar{u}_3'^{3-}]^{(\beta,\gamma)} \tag{20}$$

where

$$\bar{u}_i'^{2\pm(\beta,\gamma)} = \frac{1}{l_\gamma} \int_{-l_\gamma/2}^{l_\gamma/2} u_i'^{(\beta,\gamma)}(\pm\frac{h_\beta}{2}, \bar{y}_3^{(\gamma)}) d\bar{y}_3^{(\gamma)} \tag{21}$$

$$\bar{u}_i'^{3\pm(\beta,\gamma)} = \frac{1}{h_\beta} \int_{-h_\beta/2}^{h_\beta/2} u_i'^{(\beta,\gamma)}(\bar{y}_2^{(\beta)}, \pm\frac{l_\gamma}{2}) d\bar{y}_2^{(\beta)} \qquad i = 1, 2, 3 \tag{22}$$

and where $\bar{u}_i'^{j\pm(\beta,\gamma)}$ is the fluctuating surface-averaged displacement in the ith direction evaluated on the face of the (β, γ) subcell with normal in the $\pm j^{th}$ direction, Fig. 2. Substituting the expressions for $u_i'^{(\beta,\gamma)}$ given by Eqs. (6) in the above definitions, performing the averaging procedure, and assembling the resulting fluctuating surface-averaged displacements in matrix form yields

$$\begin{bmatrix} \bar{u}_1'^{2+} \\ \bar{u}_1'^{2-} \end{bmatrix}^{(\beta,\gamma)} = \begin{bmatrix} \frac{h_\beta}{2} & \frac{h_\beta^2}{4} \\ -\frac{h_\beta}{2} & \frac{h_\beta^2}{4} \end{bmatrix} \begin{bmatrix} W_{1(10)} \\ W_{1(20)} \end{bmatrix}^{(\beta,\gamma)} + \begin{bmatrix} W_{1(00)} \\ W_{1(00)} \end{bmatrix}^{(\beta,\gamma)} \tag{23}$$

$$\begin{bmatrix} \bar{u}_1'^{3+} \\ \bar{u}_1'^{3-} \end{bmatrix}^{(\beta,\gamma)} = \begin{bmatrix} \frac{l_\gamma}{2} & \frac{l_\gamma^2}{4} \\ -\frac{l_\gamma}{2} & \frac{l_\gamma^2}{4} \end{bmatrix} \begin{bmatrix} W_{1(01)} \\ W_{1(02)} \end{bmatrix}^{(\beta,\gamma)} + \begin{bmatrix} W_{1(00)} \\ W_{1(00)} \end{bmatrix}^{(\beta,\gamma)} \tag{24}$$

$$\begin{bmatrix} \bar{u}_2'^{2+} \\ \bar{u}_2'^{2-} \end{bmatrix}^{(\beta,\gamma)} = \begin{bmatrix} \frac{h_\beta}{2} & \frac{h_\beta^2}{4} \\ -\frac{h_\beta}{2} & \frac{h_\beta^2}{4} \end{bmatrix} \begin{bmatrix} W_{2(10)} \\ W_{2(20)} \end{bmatrix}^{(\beta,\gamma)} + \begin{bmatrix} W_{2(00)} \\ W_{2(00)} \end{bmatrix}^{(\beta,\gamma)} \tag{25}$$

$$\begin{bmatrix} \bar{u}_3'^{2+} \\ \bar{u}_3'^{2-} \end{bmatrix}^{(\beta,\gamma)} = \begin{bmatrix} \frac{h_\beta}{2} & \frac{h_\beta^2}{4} \\ -\frac{h_\beta}{2} & \frac{h_\beta^2}{4} \end{bmatrix} \begin{bmatrix} W_{3(10)} \\ W_{3(20)} \end{bmatrix}^{(\beta,\gamma)} + \begin{bmatrix} W_{3(00)} \\ W_{3(00)} \end{bmatrix}^{(\beta,\gamma)} \tag{26}$$

$$\begin{bmatrix} \bar{u}_2'^{3+} \\ \bar{u}_2'^{3-} \end{bmatrix}^{(\beta,\gamma)} = \begin{bmatrix} \frac{l_\gamma}{2} & \frac{l_\gamma^2}{4} \\ -\frac{l_\gamma}{2} & \frac{l_\gamma^2}{4} \end{bmatrix} \begin{bmatrix} W_{2(01)} \\ W_{2(02)} \end{bmatrix}^{(\beta,\gamma)} + \begin{bmatrix} W_{2(00)} \\ W_{2(00)} \end{bmatrix}^{(\beta,\gamma)} \tag{27}$$

$$\begin{bmatrix} \bar{u}_3'^{3+} \\ \bar{u}_3'^{3-} \end{bmatrix}^{(\beta,\gamma)} = \begin{bmatrix} \frac{l_\gamma}{2} & \frac{l_\gamma^2}{4} \\ -\frac{l_\gamma}{2} & \frac{l_\gamma^2}{4} \end{bmatrix} \begin{bmatrix} W_{3(01)} \\ W_{3(02)} \end{bmatrix}^{(\beta,\gamma)} + \begin{bmatrix} W_{3(00)} \\ W_{3(00)} \end{bmatrix}^{(\beta,\gamma)} \tag{28}$$

Adding and subtracting rows in each of the above equations, we obtain the following relations

$$\begin{bmatrix} W_{1(10)} \\ W_{1(20)} \end{bmatrix}^{(\beta,\gamma)} = \begin{bmatrix} \frac{1}{h_\beta} & -\frac{1}{h_\beta} \\ \frac{2}{h_\beta^2} & \frac{2}{h_\beta^2} \end{bmatrix} \begin{bmatrix} \bar{u}_1'^{2+} \\ \bar{u}_1'^{2-} \end{bmatrix}^{(\beta,\gamma)} - \frac{4}{h_\beta^2} \begin{bmatrix} 0 \\ W_{1(00)} \end{bmatrix}^{(\beta,\gamma)} \tag{29}$$

$$\begin{bmatrix} W_{1(01)} \\ W_{1(02)} \end{bmatrix}^{(\beta,\gamma)} = \begin{bmatrix} \frac{1}{l_\gamma} & -\frac{1}{l_\gamma} \\ \frac{2}{l_\gamma^2} & \frac{2}{l_\gamma^2} \end{bmatrix} \begin{bmatrix} \bar{u}_1'^{3+} \\ \bar{u}_1'^{3-} \end{bmatrix}^{(\beta,\gamma)} - \frac{4}{l_\gamma^2} \begin{bmatrix} 0 \\ W_{1(00)} \end{bmatrix}^{(\beta,\gamma)} \tag{30}$$

$$\begin{bmatrix} W_{2(10)} \\ W_{2(20)} \end{bmatrix}^{(\beta,\gamma)} = \begin{bmatrix} \frac{1}{h_\beta} & -\frac{1}{h_\beta} \\ \frac{2}{h_\beta^2} & \frac{2}{h_\beta^2} \end{bmatrix} \begin{bmatrix} \bar{u}_2'^{2+} \\ \bar{u}_2'^{2-} \end{bmatrix}^{(\beta,\gamma)} - \frac{4}{h_\beta^2} \begin{bmatrix} 0 \\ W_{2(00)} \end{bmatrix}^{(\beta,\gamma)} \tag{31}$$

$$\begin{bmatrix} W_{3(10)} \\ W_{3(20)} \end{bmatrix}^{(\beta,\gamma)} = \begin{bmatrix} \frac{1}{h_\beta} & -\frac{1}{h_\beta} \\ \frac{2}{h_\beta^2} & \frac{2}{h_\beta^2} \end{bmatrix} \begin{bmatrix} \bar{u}_3'^{2+} \\ \bar{u}_3'^{2-} \end{bmatrix}^{(\beta,\gamma)} - \frac{4}{h_\beta^2} \begin{bmatrix} 0 \\ W_{3(00)} \end{bmatrix}^{(\beta,\gamma)} \tag{32}$$

$$\begin{bmatrix} W_{2(01)} \\ W_{2(02)} \end{bmatrix}^{(\beta,\gamma)} = \begin{bmatrix} \frac{1}{l_\gamma} & -\frac{1}{l_\gamma} \\ \frac{2}{l_\gamma^2} & \frac{2}{l_\gamma^2} \end{bmatrix} \begin{bmatrix} \bar{u}_2'^{3+} \\ \bar{u}_2'^{3-} \end{bmatrix}^{(\beta,\gamma)} - \frac{4}{l_\gamma^2} \begin{bmatrix} 0 \\ W_{2(00)} \end{bmatrix}^{(\beta,\gamma)} \tag{33}$$

$$\begin{bmatrix} W_{3(01)} \\ W_{3(02)} \end{bmatrix}^{(\beta,\gamma)} = \begin{bmatrix} \frac{1}{l_\gamma} & -\frac{1}{l_\gamma} \\ \frac{2}{l_\gamma^2} & \frac{2}{l_\gamma^2} \end{bmatrix} \begin{bmatrix} \bar{u}_3'^{3+} \\ \bar{u}_3'^{3-} \end{bmatrix}^{(\beta,\gamma)} - \frac{4}{l_\gamma^2} \begin{bmatrix} 0 \\ W_{3(00)} \end{bmatrix}^{(\beta,\gamma)} \tag{34}$$

Equations $(29) - (34)$ relate the first- and second-order microvariables to the fluctuating surface-averaged displacements and the zeroth-order microvariables. In order to express the microvariables explicitly in terms of the surface-averaged quantities, the local stress equilibrium equations are satisfied in a volumetric sense. We note that the reformulation eliminates the need to consider the first and second moments of these equations, simplifying the volume averaging procedure of the equilibrium equations to the zeroth moments as shown below

$$\frac{1}{h_\beta l_\gamma} \int_{-l_\gamma/2}^{l_\gamma/2} \int_{-h_\beta/2}^{h_\beta/2} \sigma_{ji,j}^{(\beta,\gamma)} d\bar{y}_2^{(\beta)} d\bar{y}_3^{(\gamma)} = 0, \qquad i = 1, 2, 3 \tag{35}$$

Expressing the subcell stresses $\sigma_{ij}^{(\beta,\gamma)}$ in terms of the fluctuating surface-averaged displacement using the expressions for the first- and second-order microvariables $W_{i(mn)}^{(\beta,\gamma)}$ given by Eqs. $(29) - (34)$ in Eqs. (8) and the resulting relations in Eqs. (9), and performing the required integration in the above equation yields after simplification

$$W_{1(00)}^{(\beta,\gamma)} = \frac{C_{66}^{(\beta,\gamma)}}{2\bar{C}_{11}^{(\beta,\gamma)}}(\bar{u}_1'^{2+} + \bar{u}_1'^{2-})^{(\beta,\gamma)} + \frac{h_\beta^2 C_{55}^{(\beta,\gamma)}}{2l_\gamma^2 \bar{C}_{11}^{(\beta,\gamma)}}(\bar{u}_1'^{3+} + \bar{u}_1'^{3-})^{(\beta,\gamma)} \tag{36}$$

$$W_{2(00)}^{(\beta,\gamma)} = \frac{C_{22}^{(\beta,\gamma)}}{2\bar{C}_{22}^{(\beta,\gamma)}}(\bar{u}_2'^{2+} + \bar{u}_2'^{2-})^{(\beta,\gamma)} + \frac{h_\beta^2 C_{44}^{(\beta,\gamma)}}{2l_\gamma^2 \bar{C}_{22}^{(\beta,\gamma)}}(\bar{u}_2'^{3+} + \bar{u}_2'^{3-})^{(\beta,\gamma)} \tag{37}$$

$$W_{3(00)}^{(\beta,\gamma)} = \frac{C_{33}^{(\beta,\gamma)}}{2\bar{C}_{33}^{(\beta,\gamma)}}(\bar{u}_3'^{3+} + \bar{u}_3'^{3-})^{(\beta,\gamma)} + \frac{l_\gamma^2 C_{44}^{(\beta,\gamma)}}{2h_\beta^2 \bar{C}_{33}^{(\beta,\gamma)}}(\bar{u}_3'^{2+} + \bar{u}_3'^{2-})^{(\beta,\gamma)} \tag{38}$$

where

$$\bar{C}_{11}^{(\beta,\gamma)} = C_{66}^{(\beta,\gamma)} + \frac{h_\beta^2}{l_\gamma^2} C_{55}^{(\beta,\gamma)} \tag{39}$$

$$\bar{C}_{22}^{(\beta,\gamma)} = C_{22}^{(\beta,\gamma)} + \frac{h_\beta^2}{l_\gamma^2} C_{44}^{(\beta,\gamma)} \tag{40}$$

$$\bar{C}_{33}^{(\beta,\gamma)} = C_{33}^{(\beta,\gamma)} + \frac{l_\gamma^2}{h_\beta^2} C_{44}^{(\beta,\gamma)} \tag{41}$$

Substituting the zeroth-order microvariables $W_{i(00)}^{(\beta,\gamma)}$ back into Eqs. $(29) - (34)$ and then the resulting equations for the first- and second-order microvariables $W_{i(mn)}^{(\beta,\gamma)}$ into the equations for surface-averaged tractions, Eqs. $(14) - (19)$, we obtain the expressions for the surface-averaged tractions exclusively in terms of the fluctuating surface-averaged displacements and the applied macroscopic strains. We observe that the inplane surface averaged tractions $\bar{t}_i^{j\pm}$ $(i, j = 2, 3)$ are solely functions of the inplane fluctuating surface-averaged displacements $\bar{u}_i'^{j\pm}$ $(i, j = 2, 3)$, and are related through the local stiffness matrix as shown below

$$\begin{bmatrix} \bar{t}_2^{2+} \\ \bar{t}_2^{2-} \\ \bar{t}_3^{2+} \\ \bar{t}_3^{2-} \\ \bar{t}_2^{3+} \\ \bar{t}_2^{3-} \\ \bar{t}_3^{3+} \\ \bar{t}_3^{3-} \end{bmatrix}^{(\beta,\gamma)} = \begin{bmatrix} K_{11} & K_{12} & 0 & 0 & K_{15} & K_{16} & K_{17} & K_{18} \\ K_{21} & K_{22} & 0 & 0 & K_{25} & K_{26} & K_{27} & K_{28} \\ 0 & 0 & K_{33} & K_{34} & K_{35} & K_{36} & K_{37} & K_{38} \\ 0 & 0 & K_{43} & K_{44} & K_{45} & K_{46} & K_{47} & K_{48} \\ K_{51} & K_{52} & K_{53} & K_{54} & K_{55} & K_{56} & 0 & 0 \\ K_{61} & K_{62} & K_{63} & K_{64} & K_{65} & K_{66} & 0 & 0 \\ K_{71} & K_{72} & K_{73} & K_{74} & 0 & 0 & K_{77} & K_{78} \\ K_{81} & K_{82} & K_{83} & K_{84} & 0 & 0 & K_{87} & K_{88} \end{bmatrix}^{(\beta,\gamma)} \begin{bmatrix} \bar{u}_2'^{2+} \\ \bar{u}_2'^{2-} \\ \bar{u}_3'^{2+} \\ \bar{u}_3'^{2-} \\ \bar{u}_2'^{3+} \\ \bar{u}_2'^{3-} \\ \bar{u}_3'^{3+} \\ \bar{u}_3'^{3-} \end{bmatrix}^{(\beta,\gamma)} +$$

$$
\begin{bmatrix}
C_{12} & C_{22} & C_{23} & 0 \\
-C_{12} & -C_{22} & -C_{23} & 0 \\
0 & 0 & 0 & 2C_{44} \\
0 & 0 & 0 & -2C_{44} \\
0 & 0 & 0 & 2C_{44} \\
0 & 0 & 0 & -2C_{44} \\
C_{13} & C_{23} & C_{33} & 0 \\
-C_{13} & -C_{23} & -C_{33} & 0
\end{bmatrix}^{(\beta,\gamma)}
\begin{bmatrix}
\bar{\varepsilon}_{11} \\
\bar{\varepsilon}_{22} \\
\bar{\varepsilon}_{33} \\
\bar{\varepsilon}_{23}
\end{bmatrix}
\tag{42}
$$

where the elements of the local stiffness matrix K_{ij} are given explicitly in terms of the mechanical properties and subcell dimensions in the Appendix. Similarly, the out-of-plane surface-averaged tractions $\bar{t}_1^{j\pm}$ $(j=2,3)$ are related to the out-of-plane displacements $\bar{u}_1'^{j\pm}$ $(j=2,3)$ through the local stiffness matrix as shown below

$$
\begin{bmatrix}
\bar{t}_1^{2+} \\
\bar{t}_1^{2-} \\
\bar{t}_1^{3+} \\
\bar{t}_1^{3-}
\end{bmatrix}^{(\beta,\gamma)}
=
\begin{bmatrix}
L_{11} & L_{12} & L_{13} & L_{14} \\
L_{21} & L_{22} & L_{23} & L_{24} \\
L_{31} & L_{32} & L_{33} & L_{34} \\
L_{41} & L_{42} & L_{43} & L_{44}
\end{bmatrix}^{(\beta,\gamma)}
\begin{bmatrix}
\bar{u}_1'^{2+} \\
\bar{u}_1'^{2-} \\
\bar{u}_1'^{3+} \\
\bar{u}_1'^{3-}
\end{bmatrix}^{(\beta,\gamma)}
+ 2
\begin{bmatrix}
C_{66} & 0 \\
-C_{66} & 0 \\
0 & C_{55} \\
0 & -C_{55}
\end{bmatrix}^{(\beta,\gamma)}
\begin{bmatrix}
\bar{\varepsilon}_{12} \\
\bar{\varepsilon}_{13}
\end{bmatrix}
\tag{43}
$$

where the elements of the local stiffness matrix L_{ij} are also given explicitly in terms of the mechanical properties and subcell dimensions in the Appendix.

3.2   Global Stiffness Matrix

The local stiffness matrices are used to construct the global stiffness matrix using first the interfacial displacement and tractions continuity conditions, and then the periodic boundary conditions, all imposed in a surface-averaged sense across adjacent subcell interfaces. We start with the displacement continuity conditions. Considering the βth interface, the fluctuating surface-averaged displacements in the x_1 direction, $\bar{u}_1'^{2+(\beta,\gamma)}$, $\bar{u}_1'^{2-(\beta+1,\gamma)}$, and the corresponding displacements in the x_2 and x_3 directions, $\bar{u}_2'^{2+(\beta,\gamma)}$, $\bar{u}_2'^{2-(\beta+1,\gamma)}$, and $\bar{u}_3'^{2+(\beta,\gamma)}$, $\bar{u}_3'^{2-(\beta+1,\gamma)}$, respectively, must be equal. Hence, we represent them using common unknown quantities, i.e.,

$$
\bar{u}_1'^{2+(\beta,\gamma)} = \bar{u}_1'^{2-(\beta+1,\gamma)} = \bar{u}_1'^{2(\beta+1,\gamma)}
\tag{44}
$$

$$
\bar{u}_2'^{2+(\beta,\gamma)} = \bar{u}_2'^{2-(\beta+1,\gamma)} = \bar{u}_2'^{2(\beta+1,\gamma)}
\tag{45}
$$

$$
\bar{u}_3'^{2+(\beta,\gamma)} = \bar{u}_3'^{2-(\beta+1,\gamma)} = \bar{u}_3'^{2(\beta+1,\gamma)}
\tag{46}
$$

Similarly, applying displacement continuity at the γth interface in the x_1, x_2 and x_3 directions, respectively, in a surface-average sense we have

$$\bar{u}_1'^{3+(\beta,\gamma)} = \bar{u}_1'^{3-(\beta,\gamma+1)} = \bar{u}_1'^{3(\beta,\gamma+1)} \tag{47}$$

$$\bar{u}_2'^{3+(\beta,\gamma)} = \bar{u}_2'^{3-(\beta,\gamma+1)} = \bar{u}_2'^{3(\beta,\gamma+1)} \tag{48}$$

$$\bar{u}_3'^{3+(\beta,\gamma)} = \bar{u}_3'^{3-(\beta,\gamma+1)} = \bar{u}_3'^{3(\beta,\gamma+1)} \tag{49}$$

Equations $(44)-(46)$ and $(47)-(49)$ hold true for $\beta = 1, ..., N_\beta-1$ and $\gamma = 1, ..., N_\gamma-1$, respectively. This gives rise to $3(N_\beta - 1)N_\gamma + 3(N_\gamma - 1)N_\beta$ unknown surface-averaged displacements defined at the subcell interfaces along the x_2 and x_3 directions. The remaining $6(N_\beta + N_\gamma)$ surface-averaged displacements at the external boundaries of the repeating unit cell

$$\bar{u}_1'^{2(1,\gamma)}, \ \bar{u}_2'^{2(1,\gamma)}, \ \bar{u}_3'^{2(1,\gamma)}, \ \bar{u}_1'^{2(N_\beta+1,\gamma)}, \ \bar{u}_2'^{2(N_\beta+1,\gamma)}, \ \bar{u}_3'^{2(N_\beta+1,\gamma)},$$
$$\bar{u}_1'^{3(\beta,1)}, \ \bar{u}_2'^{3(\beta,1)}, \ \bar{u}_3'^{3(\beta,1)}, \ \bar{u}_1'^{3(\beta,N_\gamma+1)}, \ \bar{u}_2'^{3(\beta,N_\gamma+1)}, \ \bar{u}_3'^{3(\beta,N_\gamma+1)} \tag{50}$$

are related to the corresponding surface-averaged boundary tractions. These surface-averaged boundary quantities are related through the periodic boundary conditions which will be incorporated into the global stiffness matrix.

Next, the traction continuity conditions at the interfaces between adjacent subcells are imposed. Considering the βth interface, the continuity of tractions in the x_1, x_2 and x_3 directions, respectively, is ensured by

$$\bar{t}_1^{2+(\beta,\gamma)} + \bar{t}_1^{2-(\beta+1,\gamma)} = 0 \tag{51}$$

$$\bar{t}_2^{2+(\beta,\gamma)} + \bar{t}_2^{2-(\beta+1,\gamma)} = 0 \tag{52}$$

$$\bar{t}_3^{2+(\beta,\gamma)} + \bar{t}_3^{2-(\beta+1,\gamma)} = 0 \tag{53}$$

where $\bar{t}_i^{2+(\beta,\gamma)}$ $(i = 1, 2, 3)$ are the surface-averaged traction components on the right face ($\overline{x}_2 = h_\beta/2$) of the (β,γ) subcell and $\bar{t}_i^{2-(\beta+1,\gamma)}$ $(i = 1, 2, 3)$ are the surface-averaged traction components on the left face ($x_2 = -h_{\beta+1}/2$) of the $(\beta+1,\gamma)$ subcell , defined by Eq. (12). Similarly, applying traction continuity at the γth interface in the x_1, x_2 and x_3 directions, respectively, in an average sense we obtain

$$\bar{t}_1^{3+(\beta,\gamma)} + \bar{t}_1^{3-(\beta,\gamma+1)} = 0 \tag{54}$$

$$\bar{t}_2^{3+(\beta,\gamma)} + \bar{t}_2^{3-(\beta,\gamma+1)} = 0 \tag{55}$$

$$\bar{t}_3^{3+(\beta,\gamma)} + \bar{t}_3^{3-(\beta,\gamma+1)} = 0 \tag{56}$$

Equations (52)-(53) and Eqs. (55)-(56) can be written in terms of the common interfacial surface-averaged displacements $\bar{u}_2'^{2(\cdot,\cdot)}$, $\bar{u}_2'^{3(\cdot,\cdot)}$, $\bar{u}_3'^{2(\cdot,\cdot)}$, $\bar{u}_3'^{3(\cdot,\cdot)}$ using the local stiffness matrix that relates the inplane surface-averaged tractions and displacements, Eq. (42), and the displacement continuity conditions given by Eqs. (45)-(46), and Eqs. (48)-(49)

$$K_{12}^{(\beta,\gamma)}\bar{u}_2'^{2(\beta,\gamma)} + (K_{11}^{(\beta,\gamma)} + K_{22}^{(\beta+1,\gamma)})\bar{u}_2'^{2(\beta+1,\gamma)} + K_{21}^{(\beta+1,\gamma)}\bar{u}_2'^{2(\beta+2,\gamma)} + K_{16}^{(\beta,\gamma)}\bar{u}_2'^{3(\beta,\gamma)} +$$
$$K_{15}^{(\beta,\gamma)}\bar{u}_2'^{3(\beta,\gamma+1)} + K_{26}^{(\beta+1,\gamma)}\bar{u}_2'^{3(\beta+1,\gamma)} + K_{25}^{(\beta+1,\gamma)}\bar{u}_2'^{3(\beta+1,\gamma+1)} + K_{18}^{(\beta,\gamma)}\bar{u}_3'^{3(\beta,\gamma)} +$$
$$K_{17}^{(\beta,\gamma)}\bar{u}_3'^{3(\beta,\gamma+1)} + K_{28}^{(\beta+1,\gamma)}\bar{u}_3'^{3(\beta+1,\gamma)} + K_{27}^{(\beta+1,\gamma)}\bar{u}_3'^{3(\beta+1,\gamma+1)} =$$
$$(C_{12}^{(\beta,\gamma)} - C_{12}^{(\beta+1,\gamma)})\bar{\varepsilon}_{11} + (C_{22}^{(\beta,\gamma)} - C_{22}^{(\beta+1,\gamma)})\bar{\varepsilon}_{22} + (C_{23}^{(\beta,\gamma)} - C_{23}^{(\beta+1,\gamma)})\bar{\varepsilon}_{33} \qquad (57)$$

$$K_{34}^{(\beta,\gamma)}\bar{u}_3'^{2(\beta,\gamma)} + (K_{33}^{(\beta,\gamma)} + K_{44}^{(\beta+1,\gamma)})\bar{u}_3'^{2(\beta+1,\gamma)} + K_{43}^{(\beta+1,\gamma)}\bar{u}_3'^{2(\beta+2,\gamma)} + K_{36}^{(\beta,\gamma)}\bar{u}_2'^{3(\beta,\gamma)} +$$
$$K_{46}^{(\beta+1,\gamma)}\bar{u}_2'^{3(\beta+1,\gamma)} + K_{35}^{(\beta,\gamma)}\bar{u}_2'^{3(\beta,\gamma+1)} + K_{45}^{(\beta+1,\gamma)}\bar{u}_2'^{3(\beta+1,\gamma+1)} + K_{38}^{(\beta,\gamma)}\bar{u}_3'^{3(\beta,\gamma)} +$$
$$K_{48}^{(\beta+1,\gamma)}\bar{u}_3'^{3(\beta+1,\gamma)} + K_{37}^{(\beta,\gamma)}\bar{u}_3'^{3(\beta,\gamma+1)} + K_{47}^{(\beta+1,\gamma)}\bar{u}_3'^{3(\beta+1,\gamma+1)} = 2(C_{44}^{(\beta,\gamma)} - C_{44}^{(\beta+1,\gamma)})\bar{\varepsilon}_{23} \qquad (58)$$

$$K_{52}^{(\beta,\gamma)}\bar{u}_2'^{2(\beta,\gamma)} + K_{51}^{(\beta,\gamma)}\bar{u}_2'^{2(\beta+1,\gamma)} + K_{62}^{(\beta,\gamma+1)}\bar{u}_2'^{2(\beta,\gamma+1)} + K_{61}^{(\beta,\gamma+1)}\bar{u}_2'^{2(\beta+1,\gamma+1)} +$$
$$K_{54}^{(\beta,\gamma)}\bar{u}_3'^{2(\beta,\gamma)} + K_{53}^{(\beta,\gamma)}\bar{u}_3'^{2(\beta+1,\gamma)} + K_{64}^{(\beta,\gamma+1)}\bar{u}_3'^{2(\beta,\gamma+1)} + K_{63}^{(\beta,\gamma+1)}\bar{u}_3'^{2(\beta+1,\gamma+1)} +$$
$$K_{56}^{(\beta,\gamma)}\bar{u}_2'^{3(\beta,\gamma)} + (K_{55}^{(\beta,\gamma)} + K_{66}^{(\beta,\gamma+1)})\bar{u}_2'^{3(\beta,\gamma+1)} + K_{65}^{(\beta,\gamma+1)}\bar{u}_2'^{3(\beta,\gamma+2)} = 2(C_{44}^{(\beta,\gamma)} - C_{44}^{(\beta,\gamma+1)})\bar{\varepsilon}_{23} \quad (59)$$

$$K_{72}^{(\beta,\gamma)}\bar{u}_2'^{2(\beta,\gamma)} + K_{71}^{(\beta,\gamma)}\bar{u}_2'^{2(\beta+1,\gamma)} + K_{82}^{(\beta,\gamma+1)}\bar{u}_2'^{2(\beta,\gamma+1)} + K_{81}^{(\beta,\gamma+1)}\bar{u}_2'^{2(\beta+1,\gamma+1)} +$$
$$K_{74}^{(\beta,\gamma)}\bar{u}_3'^{2(\beta,\gamma)} + K_{73}^{(\beta,\gamma)}\bar{u}_3'^{2(\beta+1,\gamma)} + K_{84}^{(\beta,\gamma+1)}\bar{u}_3'^{2(\beta,\gamma+1)} + K_{83}^{(\beta,\gamma+1)}\bar{u}_3'^{2(\beta+1,\gamma+1)} +$$
$$K_{78}^{(\beta,\gamma)}\bar{u}_3'^{3(\beta,\gamma)} + (K_{77}^{(\beta,\gamma)} + K_{88}^{(\beta,\gamma+1)})\bar{u}_3'^{3(\beta,\gamma+1)} + K_{87}^{(\beta,\gamma+1)}\bar{u}_3'^{3(\beta,\gamma+2)} =$$
$$(C_{13}^{(\beta,\gamma)} - C_{13}^{(\beta,\gamma+1)})\bar{\varepsilon}_{11} + (C_{23}^{(\beta,\gamma)} - C_{23}^{(\beta,\gamma+1)})\bar{\varepsilon}_{22} + (C_{33}^{(\beta,\gamma)} - C_{33}^{(\beta,\gamma+1)})\bar{\varepsilon}_{33} \qquad (60)$$

Similarly, Equations (51) and (54) can be written in terms of the common interfacial surface-averaged displacements $\bar{u}_1'^{2(\cdot,\cdot)}$, $\bar{u}_1'^{3(\cdot,\cdot)}$ using the local stiffness matrix that relates the out-of-plane surface-averaged tractions and displacements, Eq. (43), and the displacement continuity conditions given by Eqs. (44) and (47),

$$L_{12}^{(\beta,\gamma)}\bar{u}_1'^{2(\beta,\gamma)} + (L_{11}^{(\beta,\gamma)} + L_{22}^{(\beta+1,\gamma)})\bar{u}_1'^{2(\beta+1,\gamma)} + L_{21}^{(\beta+1,\gamma)}\bar{u}_1'^{2(\beta+2,\gamma)} + L_{14}^{(\beta,\gamma)}\bar{u}_1'^{3(\beta,\gamma)} +$$
$$L_{13}^{(\beta,\gamma)}\bar{u}_1'^{3(\beta,\gamma+1)} + L_{24}^{(\beta+1,\gamma)}\bar{u}_1'^{3(\beta+1,\gamma)} + L_{23}^{(\beta+1,\gamma)}\bar{u}_1'^{3(\beta+1,\gamma+1)} = 2(C_{66}^{(\beta,\gamma)} - C_{66}^{(\beta+1,\gamma)})\bar{\varepsilon}_{12} \qquad (61)$$

$$L_{32}^{(\beta,\gamma)}\bar{u}_1'^{2(\beta,\gamma)} + L_{31}^{(\beta,\gamma)}\bar{u}_1'^{2(\beta+1,\gamma)} + L_{42}^{(\beta,\gamma+1)}\bar{u}_1'^{2(\beta,\gamma+1)} + L_{41}^{(\beta,\gamma+1)}\bar{u}_1'^{2(\beta+1,\gamma+1)} +$$
$$L_{34}^{(\beta,\gamma)}\bar{u}_1'^{3(\beta,\gamma)} + (L_{33}^{(\beta,\gamma)} + L_{44}^{(\beta,\gamma+1)})\bar{u}_1'^{3(\beta,\gamma+1)} + L_{43}^{(\beta,\gamma+1)}\bar{u}_1'^{3(\beta,\gamma+2)} = 2(C_{55}^{(\beta,\gamma)} - C_{55}^{(\beta,\gamma+1)})\bar{\varepsilon}_{13} \quad (62)$$

Equations $(57) - (60)$ and $(61) - (62)$ provide us with a total of $3(N_\beta - 1)N_\gamma + 3(N_\gamma - 1)N_\beta$ equations in terms of the common interfacial surface-averaged displacements and the surface-averaged displacements at the external boundaries of the repeating unit cell.

Assembly and structure of the global stiffness matrix   We first assemble the global stiffness matrices by assuming that the repeating unit cell's boundary is subjected to prescribed surface-averaged tractions. The assembly thus includes the boundary cells $(1,\gamma)$, (N_β,γ) and $(\beta,1)$, (β,N_γ),

which provide the additional $6(N_\beta + N_\gamma)$ equations involving the boundary surface-averaged tractions and displacements, in addition to the application of the interfacial continuity conditions described above for the inplane and out-of-plane surface-averaged interfacial displacements, Eqs. (57)-(60) and Eqs. (61)-(62), respectively. The final system of equations relating the inplane quantities is symbolically written as follows

$$
\begin{bmatrix}
\mathbf{K}_{11} & \mathbf{0} & \mathbf{K}_{13} & \mathbf{K}_{14} \\
\mathbf{0} & \mathbf{K}_{22} & \mathbf{K}_{23} & \mathbf{K}_{24} \\
\mathbf{K}_{31} & \mathbf{K}_{32} & \mathbf{K}_{33} & \mathbf{0} \\
\mathbf{K}_{41} & \mathbf{K}_{42} & \mathbf{0} & \mathbf{K}_{44}
\end{bmatrix}
\begin{bmatrix}
\bar{\mathbf{u}}_2'^2 \\
\bar{\mathbf{u}}_3'^2 \\
\bar{\mathbf{u}}_2'^3 \\
\bar{\mathbf{u}}_3'^3
\end{bmatrix}
=
\begin{bmatrix}
\bar{\mathbf{t}}_2^2 \\
\bar{\mathbf{t}}_3^2 \\
\bar{\mathbf{t}}_2^3 \\
\bar{\mathbf{t}}_3^3
\end{bmatrix}
+
\begin{bmatrix}
\Delta\mathbf{C}_{11} & \Delta\mathbf{C}_{12} & \Delta\mathbf{C}_{13} & \mathbf{0} \\
\mathbf{0} & \mathbf{0} & \mathbf{0} & \Delta\mathbf{C}_{24} \\
\mathbf{0} & \mathbf{0} & \mathbf{0} & \Delta\mathbf{C}_{34} \\
\Delta\mathbf{C}_{41} & \Delta\mathbf{C}_{42} & \Delta\mathbf{C}_{43} & \mathbf{0}
\end{bmatrix}
\begin{bmatrix}
\bar{\varepsilon}_{11} \\
\bar{\varepsilon}_{22} \\
\bar{\varepsilon}_{33} \\
\bar{\varepsilon}_{23}
\end{bmatrix}
\tag{63}
$$

where

$$
\begin{aligned}
\bar{\mathbf{u}}_2'^2 &= [\bar{\mathbf{u}}_2'^{2(1)}, ..., \bar{\mathbf{u}}_2'^{2(N_\gamma)}] & \text{with} & & \bar{\mathbf{u}}_2'^{2(\gamma)} &= [\bar{u}_2'^{2(1,\gamma)}, ..., \bar{u}_2'^{2(N_\beta+1,\gamma)}] \\
\bar{\mathbf{u}}_3'^2 &= [\bar{\mathbf{u}}_3'^{2(1)}, ..., \bar{\mathbf{u}}_3'^{2(N_\gamma)}] & \text{with} & & \bar{\mathbf{u}}_3'^{2(\gamma)} &= [\bar{u}_3'^{2(1,\gamma)}, ..., \bar{u}_3'^{2(N_\beta+1,\gamma)}] \\
\bar{\mathbf{u}}_2'^3 &= [\bar{\mathbf{u}}_2'^{3(1)}, ..., \bar{\mathbf{u}}_2'^{3(N_\beta)}] & \text{with} & & \bar{\mathbf{u}}_2'^{3(\beta)} &= [\bar{u}_2'^{3(\beta,1)}, ..., \bar{u}_2'^{3(\beta,N_\gamma+1)}] \\
\bar{\mathbf{u}}_3'^3 &= [\bar{\mathbf{u}}_3'^{3(1)}, ..., \bar{\mathbf{u}}_3'^{3(N_\beta)}] & \text{with} & & \bar{\mathbf{u}}_3'^{3(\beta)} &= [\bar{u}_3'^{3(\beta,1)}, ..., \bar{u}_3'^{3(\beta,N_\gamma+1)}]
\end{aligned}
$$

and the structure of the surface-averaged traction vectors $\bar{\mathbf{t}}_2^2$, $\bar{\mathbf{t}}_3^2$, $\bar{\mathbf{t}}_2^3$, $\bar{\mathbf{t}}_3^3$ is similar to the above surface-averaged interfacial displacement vectors. In this case, however, the only non-zero surface-averaged traction components are those associated with the external surfaces of the boundary subcells as shown below. This follows from the interfacial traction continuity conditions given by Eqs. (52)-(53) and Eqs. (55)-(56) in the case of the inplane quantities.

$$
\begin{aligned}
\bar{\mathbf{t}}_2^2 &= [\bar{\mathbf{t}}_2^{2(1)}, ..., \bar{\mathbf{t}}_2^{2(N_\gamma)}] & \text{with} & & \bar{\mathbf{t}}_2^{2(\gamma)} &= [\bar{t}_2^{2(1,\gamma)}, 0, ..., 0, \bar{t}_2^{2(N_\beta+1,\gamma)}] \\
\bar{\mathbf{t}}_3^2 &= [\bar{\mathbf{t}}_3^{2(1)}, ..., \bar{\mathbf{t}}_3^{2(N_\gamma)}] & \text{with} & & \bar{\mathbf{t}}_3^{2(\gamma)} &= [\bar{t}_3^{2(1,\gamma)}, 0, ..., 0, \bar{t}_3^{2(N_\beta+1,\gamma)}] \\
\bar{\mathbf{t}}_2^3 &= [\bar{\mathbf{t}}_2^{3(1)}, ..., \bar{\mathbf{t}}_2^{3(N_\beta)}] & \text{with} & & \bar{\mathbf{t}}_2^{3(\beta)} &= [\bar{t}_2^{3(\beta,1)}, 0, ..., 0, \bar{t}_2^{3(\beta,N_\gamma+1)}] \\
\bar{\mathbf{t}}_3^3 &= [\bar{\mathbf{t}}_3^{3(1)}, ..., \bar{\mathbf{t}}_3^{3(N_\beta)}] & \text{with} & & \bar{\mathbf{t}}_3^{3(\beta)} &= [\bar{t}_3^{3(\beta,1)}, 0, ..., 0, \bar{t}_3^{3(\beta,N_\gamma+1)}]
\end{aligned}
$$

The global stiffness matrix in the above system of equations consists of twelve non-zero submatrices. The diagonal submatrices $\mathbf{K}_{11}$, $\mathbf{K}_{22}$, $\mathbf{K}_{33}$ and $\mathbf{K}_{44}$ relate the surface-averaged tractions to displacements along their respective directions (for instance $\mathbf{K}_{11}$ relates $\mathbf{t}_2^2$ to $\mathbf{u}_2'^2$, $\mathbf{K}_{22}$ relates $\mathbf{t}_3^2$ to $\mathbf{u}_3'^2$, etc..) and have entries concentrated along the diagonal. The off-diagonal submatrices couple the surface-averaged quantities along the x_2 and x_3 directions ($\mathbf{K}_{13}$ relates $\mathbf{t}_2^2$ to $\mathbf{u}_2'^3$, $\mathbf{K}_{14}$ relates $\mathbf{t}_2^2$ to $\mathbf{u}_3'^3$, etc..) and have entries scattered throughout. The structure of the diagonal and off-diagonal submatrices, viz. $\mathbf{K}_{11}$, $\mathbf{K}_{13}$ etc. constituting the inplane global stiffness matrix has been described in detail by Bansal and Pindera [29] in the context of reformulated higher-order theory. The size of the global stiffness matrix for the inplane surface-averaged interfacial displacements is

$$
[2N_\beta(N_\gamma + 1) + 2N_\gamma(N_\beta + 1)] \times [2N_\beta(N_\gamma + 1) + 2N_\gamma(N_\beta + 1)]
$$

Finally, the column submatrices $\Delta\mathbf{C}_{11}, , , , \Delta\mathbf{C}_{44}$, which are multiplied by the macroscopic strains on the right hand side of Eqs. (63), represent the differences in the elastic stiffness elements $C_{ij}^{(\beta\gamma)}$ between adjacent subcells in the y_2 and y_3 directions, as shown on the right hand side of the traction continuity equations given by Eqs. (57)-(60).

Similarly, the final system of equations relating the out-of-plane quantities is symbolically written as

$$
\begin{bmatrix} \mathbf{L}_{11} & \mathbf{L}_{12} \\ \mathbf{L}_{21} & \mathbf{L}_{22} \end{bmatrix} \begin{bmatrix} \bar{\mathbf{u}}_1'^2 \\ \bar{\mathbf{u}}_1'^3 \end{bmatrix} = \begin{bmatrix} \bar{\mathbf{t}}_1^2 \\ \bar{\mathbf{t}}_1^3 \end{bmatrix} + \begin{bmatrix} \Delta\mathbf{c}_{11} & \mathbf{0} \\ \mathbf{0} & \Delta\mathbf{c}_{22} \end{bmatrix} \begin{bmatrix} \bar{\varepsilon}_{12} \\ \bar{\varepsilon}_{13} \end{bmatrix}
\tag{64}
$$

where

$$
\begin{aligned}
\bar{\mathbf{u}}_1'^2 &= [\bar{\mathbf{u}}_1'^{2(1)}, ..., \bar{\mathbf{u}}_1'^{2(N_\gamma)}] && \text{with} && \bar{\mathbf{u}}_1'^{2(\gamma)} = [\bar{u}_1'^{2(1,\gamma)}, ..., \bar{u}_1'^{2(N_\beta+1,\gamma)}] \\
\bar{\mathbf{u}}_1'^3 &= [\bar{\mathbf{u}}_1'^{3(1)}, ..., \bar{\mathbf{u}}_1'^{3(N_\beta)}] && \text{with} && \bar{\mathbf{u}}_1'^{3(\beta)} = [\bar{u}_1'^{3(\beta,1)}, ..., \bar{u}_1'^{3(\beta,N_\gamma+1)}]
\end{aligned}
$$

and the structure of the surface-averaged tractions $\bar{\mathbf{t}}_1^2$ and $\bar{\mathbf{t}}_1^3$ is similar to the corresponding inplane quantities. The global stiffness matrix in the above system of equations consists of four submatrices. The diagonal submatrices $\mathbf{L}_{11}$, $\mathbf{L}_{22}$ relate the surface-averaged tractions to displacements in their respective directions i.e., $\mathbf{t}_1^2$ to $\bar{\mathbf{u}}_1'^2$ and $\mathbf{t}_1^3$ to $\bar{\mathbf{u}}_1'^3$, respectively, and have entries concentrated along the diagonal. The submatrices $\mathbf{L}_{12}$, $\mathbf{L}_{21}$ represent coupling of the surface-averaged quantities in the x_2 and x_3 directions, $\mathbf{t}_1^2$ with $\bar{\mathbf{u}}_1'^3$ and $\mathbf{t}_1^3$ with $\bar{\mathbf{u}}_1'^2$, respectively, and have entries scattered throughout. The structure of the submatrices $\mathbf{L}_{11}$ and $\mathbf{L}_{22}$ is similar to the structure of $\mathbf{K}_{11}$ and the structure of $\mathbf{L}_{12}$ and $\mathbf{L}_{21}$ is similar to the structure of $\mathbf{K}_{13}$. The size of the global stiffness matrix for the out-of-plane surface-averaged interfacial displacements is

$$
[N_\beta(N_\gamma + 1) + N_\gamma(N_\beta + 1)] \times [N_\beta(N_\gamma + 1) + N_\gamma(N_\beta + 1)]
$$

Finally, the column submatrices $\Delta\mathbf{c}_{11}, , , , \Delta\mathbf{c}_{22}$, which are multiplied by the macroscopic strains on the right hand side of Eqs. (64), represent the differences in the elastic stiffness elements $C_{ij}^{(\beta\gamma)}$ between adjacent subcells in the y_2 and y_3 directions, as shown on the right hand side of the traction continuity equations given by Eqs. (61)-(62).

Reduction of the global stiffness matrices The global stiffness matrices given in Eqs. (63) and (64) are further reduced using periodicity conditions on the surface-averaged displacements and tractions imposed on the external surfaces of the boundary subcells around the repeating unit cell. The periodicity conditions for the surface-averaged boundary displacements are

$$
\begin{aligned}
\bar{u}_1'^{2(1,\gamma)} &= \bar{u}_1'^{2(N_\beta+1,\gamma)} & \bar{u}_2'^{2(1,\gamma)} &= \bar{u}_2'^{2(N_\beta+1,\gamma)} & \bar{u}_3'^{2(1,\gamma)} &= \bar{u}_3'^{2(N_\beta+1,\gamma)} \\
\bar{u}_1'^{3(\beta,1)} &= \bar{u}_1'^{3(\beta,N_\gamma+1)} & \bar{u}_2'^{3(\beta,1)} &= \bar{u}_2'^{3(\beta,N_\gamma+1)} & \bar{u}_3'^{3(\beta,1)} &= \bar{u}_3'^{3(\beta,N_\gamma+1)}
\end{aligned}
\tag{65}
$$

Similarly, the periodicity conditions for the surface-averaged boundary tractions are

$$
\begin{aligned}
\bar{t}_1^{2(1,\gamma)} + \bar{t}_1^{2(N_\beta+1,\gamma)} &= 0 & \bar{t}_2^{2(1,\gamma)} + \bar{t}_2^{2(N_\beta+1,\gamma)} &= 0 & \bar{t}_3^{2(1,\gamma)} + \bar{t}_3^{2(N_\beta+1,\gamma)} &= 0 \\
\bar{t}_1^{3(\beta,1)} + \bar{t}_1^{3(\beta,N_\gamma+1)} &= 0 & \bar{t}_2^{3(\beta,1)} + \bar{t}_2^{3(\beta,N_\gamma+1)} &= 0 & \bar{t}_3^{3(\beta,1)} + \bar{t}_3^{3(\beta,N_\gamma+1)} &= 0
\end{aligned}
\tag{66}
$$

The imposed periodicity conditions $(65) - (66)$ eliminate the traction vectors on the right hand sides of Eqs. (63) and (64), and provide us with the necessary $3(N_\beta + 1)N_\gamma + 3(N_\gamma + 1)N_\beta$ relations for the $3(N_\beta + 1)N_\gamma + 3(N_\gamma + 1)N_\beta$ unknown subcell surface-averaged displacements, i.e., $3(N_\beta - 1)N_\gamma + 3(N_\gamma - 1)N_\beta$ unknown common interfacial surface-averaged displacements along with $6(N_\beta + N_\gamma)$ unknown surface-averaged displacements at the external boundaries of the repeating unit cell. These relations are obtained from Eqs. (63) and (64) by combining and deleting appropriate rows and columns of the original stiffness matrices appearing in these equations.

The resulting reduced equations relate the unknown surface-averaged interfacial and boundary displacements to the applied macroscopic strains through the reduced stiffness matrix. The final reduction of this singular matrix involves constraining the corner subcell faces to eliminate rigid body motion. In view of the imposed periodicity conditions on the surface-averaged boundary displacements, constraining the external surfaces of one corner subcell and just one appropriate external surface of two corner subcells at opposite ends of the diagonal is sufficient.

3.3   Homogenized Constitutive Equations

The average strains in each subcell are related to the average macroscopic strains through the strain concentration tensor, Aboudi et al. [21],

$$\bar{\boldsymbol{\varepsilon}}^{(\beta,\gamma)} = \mathbb{A}^{(\beta,\gamma)}\,\bar{\boldsymbol{\varepsilon}} \tag{67}$$

The average subcell strains are obtained by averaging Eqs. (8) over the subcell volume, yielding

$$
\begin{aligned}
\bar{\varepsilon}_{11}^{(\beta,\gamma)} &= \bar{\varepsilon}_{11} \\
\bar{\varepsilon}_{22}^{(\beta,\gamma)} &= \bar{\varepsilon}_{22} + W_{2(10)}^{(\beta,\gamma)} \\
\bar{\varepsilon}_{33}^{(\beta,\gamma)} &= \bar{\varepsilon}_{33} + W_{3(01)}^{(\beta,\gamma)} \\
\bar{\varepsilon}_{12}^{(\beta,\gamma)} &= \bar{\varepsilon}_{12} + \frac{1}{2}[W_{1(10)}^{(\beta,\gamma)} \\
\bar{\varepsilon}_{13}^{(\beta,\gamma)} &= \bar{\varepsilon}_{13} + \frac{1}{2}[W_{1(01)}^{(\beta,\gamma)} \\
\bar{\varepsilon}_{23}^{(\beta,\gamma)} &= \bar{\varepsilon}_{23} + \frac{1}{2}[W_{2(01)}^{(\beta,\gamma)} + W_{3(10)}^{(\beta,\gamma)}]
\end{aligned} \tag{68}
$$

The solution of the reduced systems of equations yields the interfacial and boundary surface-averaged displacements as a function of the macroscopic strains. We then calculate the microvariables associated with each subcell in terms of the macroscopic strains using Eqs. $(36) - (38)$ and Eqs. $(29) - (34)$. This makes possible to obtain the average strain components in each subcell in terms of the macroscopic strains from Eqs. (68).

In order to determine the elements of the strain concentration tensor $\mathbb{A}^{(\beta,\gamma)}$ for each subcell, only one component of the macroscopic strain $\bar{\boldsymbol{\varepsilon}}$ is applied at a time when solving the reduced systems of equations. For instance, applying $\bar{\varepsilon}_{11} = 1$ and all others zero, and then solving the reduced systems of equations to obtain $\bar{\boldsymbol{\varepsilon}}^{(\beta,\gamma)}$ for each subcell, we obtain the first column of the

strain concentration tensor using Eq. (67). By successively applying the remaining macroscopic strain components one non-zero component at a time, we obtain the remaining elements of the strain concentration tensor $\mathbb{A}^{(\beta,\gamma)}$ for each subcell.

The average stress in each subcell is given by

$$\bar{\boldsymbol{\sigma}}^{(\beta,\gamma)} = \mathbf{C}^{(\beta,\gamma)}\bar{\boldsymbol{\varepsilon}}^{(\beta,\gamma)} \tag{69}$$

in view of the fact that the material occupying a given (β,γ) subcell is homogeneous. Using Eq. (67) to express $\bar{\boldsymbol{\varepsilon}}^{(\beta,\gamma)}$ in terms of the macroscopic strains, we obtain

$$\bar{\boldsymbol{\sigma}}^{(\beta,\gamma)} = \mathbf{C}^{(\beta,\gamma)}\mathbb{A}^{(\beta,\gamma)}\bar{\boldsymbol{\varepsilon}} \tag{70}$$

Averaging the subcell stresses over the entire repeating unit cell, we then obtain the macroscopic stress in terms of the macroscopic strains for the composite in the form

$$\bar{\boldsymbol{\sigma}} = \frac{1}{HL}\sum_{\gamma=1}^{N_\gamma}\sum_{\beta=1}^{N_\beta} h_\beta l_\gamma \mathbf{C}^{(\beta,\gamma)}\mathbb{A}^{(\beta,\gamma)}\ \bar{\boldsymbol{\varepsilon}} \tag{71}$$

which can be written as

$$\bar{\boldsymbol{\sigma}} = \mathbf{C}^*\ \bar{\boldsymbol{\varepsilon}} \tag{72}$$

where $\mathbf{C}^*$ represents the effective elastic stiffness matrix for the repeating unit cell and is given by

$$\mathbf{C}^* = \frac{1}{HL}\sum_{\gamma=1}^{N_\gamma}\sum_{\beta=1}^{N_\beta} h_\beta l_\gamma \mathbf{C}^{(\beta,\gamma)}\mathbb{A}^{(\beta,\gamma)} \tag{73}$$

4   Numerical Results

We test the high-fidelity model's predictive capability by determining the effective moduli of a unidirectional composite, with a square array of fibers in the $x_2 - x_3$ plane, as a function of the rotation angle θ about the fiber axis x_1. The moduli in the rotated coordinate system are then compared with the standard transformation equations which provide the correct answer. We also generate the local stress fields within the repeating unit cell for the given rotation angle. To highlight the advantages and need for HFGMC, the moduli as well as the local stress fields predicted by this model are compared with the corresponding GMC results. This comparison illustrates the importance of including the effects of shear coupling in heterogeneous materials.

Figure 3 shows the investigated square array of fibers with a fiber volume fraction of 0.35, extending to infinity in the $x_2 - x_3$ plane. Both the fiber and the matrix phases are isotropic. To amplify the influence of shear coupling, we consider two cases with radically different contrast between the fiber and matrix properties. In the first case, the matrix is an epoxy resin and the fibers are glass with typical elastic moduli that produce the Young's moduli ratio $E_f/E_m = 20$. In the second case, we consider an aluminum matrix weakened by holes which are simulated by very
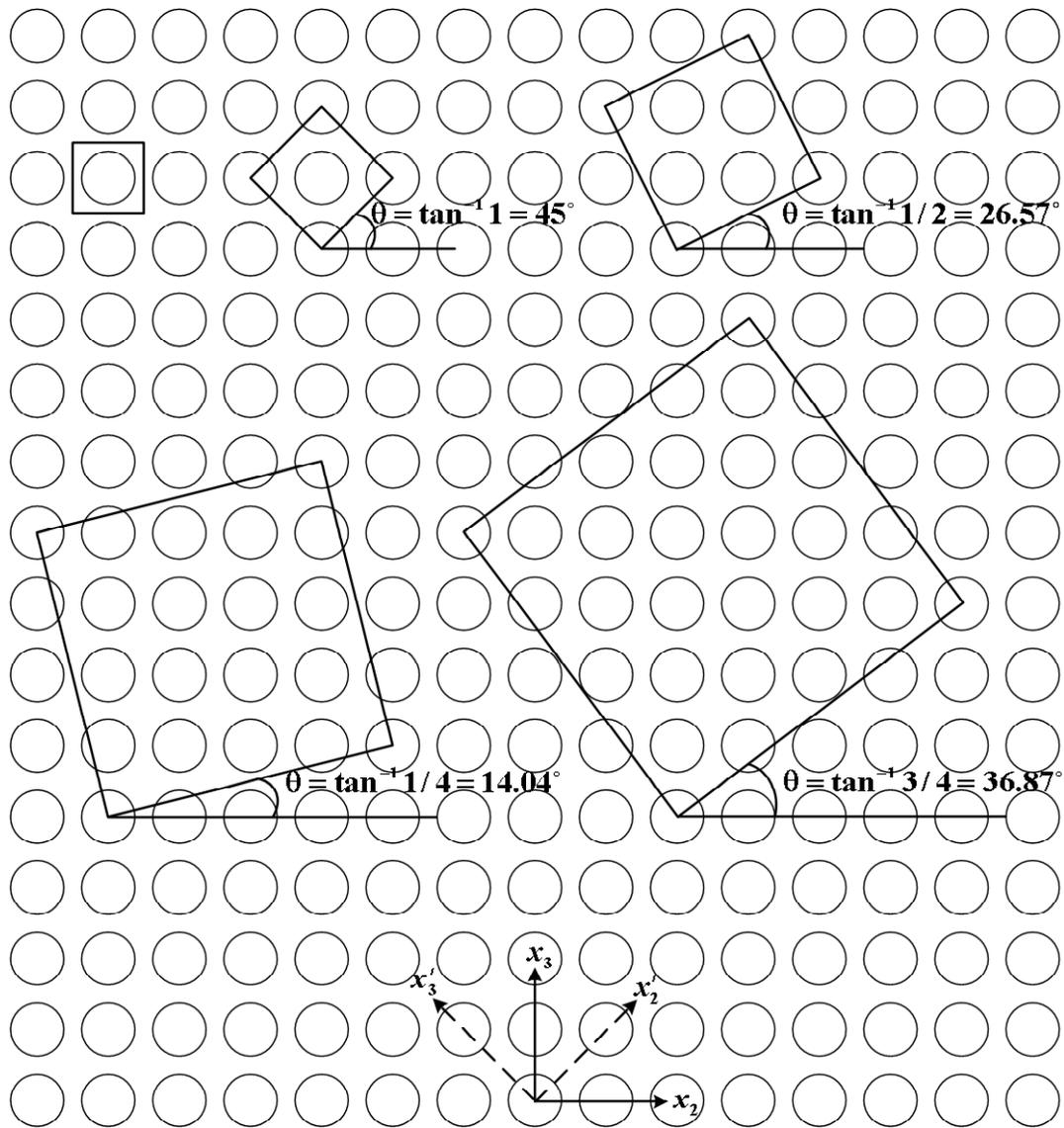
Figure 3. A representation of an infinite, square-packed array of inclusions, showing five repeating unit cells of the same array in different coordinate systems rotated by the indicated angles about the fiber axis, arranged according to increasing number of inclusions contained within each cell.

Material	Young's Modulus (MPa)	Poisson's ratio
Glass fiber	$70,000$	0.25
Epoxy matrix	$3,500$	0.35
Compliant fiber	700	0.33
Aluminum matrix	$70,000$	0.33

Table 1. Material properties of the fiber and matrix constituents.

compliant inclusions that yield the Young's moduli ratio $E_f/E_m = 0.01$. The actual constituent moduli values are given in Table 1. We note that the Young's moduli ratios for ceramic and metal matrix composites fall well within these limits, and therefore the effective moduli of these materials will not be as severely affected by lack of shear coupling.

As shown in Fig. 3, five different repeating unit cells are analyzed which produce homogenized properties of the same fiber array relative to five coordinate systems generated by rotating the principal material coordinate system through an angle θ about the fiber axis. These are arranged in two rows such that the number of fibers in each repeating unit cell increases in each row from left to right. As observed, the rotation angle does not increase monotonically with increasing number of fibers. The first repeating unit cell in the first row of Fig. 3 with the circular fiber in the center, for which $\theta = 0°$, represents the infinite square fiber array in the principal material coordinate system in light of the fact that the orthogonal planes of material symmetry passing through the fiber center coincide with the global $x_1 - x_2 - x_3$ coordinate system. Clearly, this is the simplest repeating unit cell. In order to simulate the response of this square fiber array in the coordinate system rotated by $14.04°$ about the x_1 axis, the first repeating unit cell shown in the second row of Fig. 3 containing a total of 17 fibers is employed. The repeating unit cell representing the composite in the coordinate system rotated by $26.57°$ with respect to the principal material coordinate system is the third cell in the first row of Fig. 3. In this case, there are just 5 fibers. The repeating unit cell for the rotation angle of $36.87°$ that appears last in the second row of Fig. 3 contains 25 fibers, while the one for the rotation angle of $45.0°$ which appears second in the first row of Fig. 3 contains just 2 fibers. These repeating unit cells were constructed by connecting the center of a reference fiber to the center of the fiber a certain number of fibers to the right of the reference fiber and up. This specified both the rotation angle and the length of the lower inclined edge of the repeating unit cell. Completing the square in the same manner produced the entire repeating unit cell for the particular rotation (or inclination) angle. Thus the four rotation angles were obtained from the relations

$$\theta = \tan^{-1}\{\frac{1}{4}, \frac{1}{2}, \frac{3}{4}, \frac{1}{1}\}$$

where the denominator represents the number of fiber distances to the right of the reference fiber, and the numerator the number of fibers up. The fiber distance is the horizontal or vertical distance between adjacent fiber centers. It can easily be observed that the generated repeating unit cells are the basic building blocks of the same fiber array in the five considered coordinate systems, which include the principal material system. It is also clear that three out of the five do not possess planes of material symmetry. This will result in anisotropic behavior in the $x_2 - x_3$ plane, necessitating the use of periodic boundary conditions easily accommodated by the high-fidelity model's framework.

The actual repeating unit cells in the four rotated coordinate systems used in the calculations are shown in Fig. 4 in discretized form. Table 2 provides information on the actual microstructural discretization used for each repeating unit cell, and the volume fraction of the fiber phase. We note that the fiber fraction of each repeating unit cell varied slightly from the nominal fraction of 0.35 due to
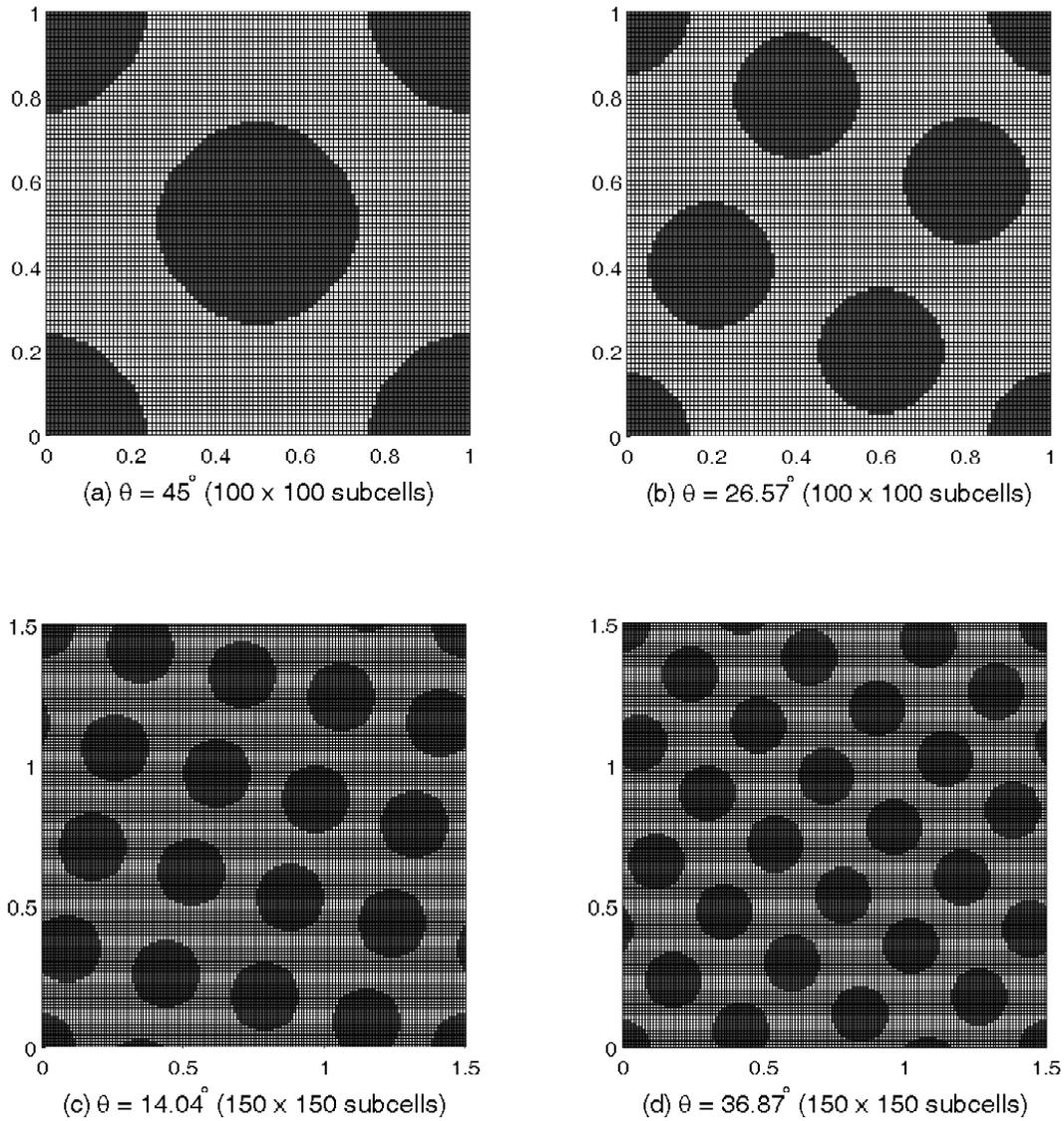
Figure 4. Detailed volume discretizations of the four repeating unit cells in the rotated coordinate systems employed to accurately capture the geometric details within each unit cell.

RUC Rotation Angle	Subcell Discretization	Fiber Volume Fraction
$\theta = \tan^{-1}(\frac{0}{1}) = 0°$	100×100	0.3468
$\theta = \tan^{-1}(\frac{1}{4}) = 14.04°$	150×150	0.3476
$\theta = \tan^{-1}(\frac{1}{2}) = 26.56°$	100×100	0.3440
$\theta = \tan^{-1}(\frac{3}{4}) = 36.87°$	150×150	0.3511
$\theta = \tan^{-1}(\frac{1}{1}) = 45°$	100×100	0.3504

Table 2. Geometric and microstructural details of the investigated repeating unit cells.

the use of square subcells to approximate the fiber shape. The actual subcell dimensions in each unit cell were dictated by the need to capture the circular fiber shape with sufficient detail given the required number of fibers within each repeating unit cell and the targeted fiber volume fraction. In the case of the repeating unit cell in the principal material coordinate system with a single fiber in the center (not shown), the repeating unit cell was discretized into 100×100 subcells in the $x_2 - x_3$ plane. The same number was used for the repeating unit cells rotated by $26.57°$ and $45.0°$ about the x_1 axis, while 150×150 subcells were employed for the unit cells rotated by $14.04°$ and $36.87°$.

The repeating unit cell in the principal material coordinate system ($\theta = 0°$, see the repeating unit cell with a single fiber in the center in Fig. 3) produces the homogenized elastic stiffness matrix $\mathbf{C}^*$ of the form

$$
\mathbf{C}^* = \begin{bmatrix}
C_{11}^* & C_{12}^* & C_{13}^* & 0 & 0 & 0 \\
C_{12}^* & C_{22}^* & C_{23}^* & 0 & 0 & 0 \\
C_{13}^* & C_{23}^* & C_{33}^* & 0 & 0 & 0 \\
0 & 0 & 0 & C_{44}^* & 0 & 0 \\
0 & 0 & 0 & 0 & C_{55}^* & 0 \\
0 & 0 & 0 & 0 & 0 & C_{66}^*
\end{bmatrix}
\tag{74}
$$

where $C_{12}^* = C_{13}^*$, $C_{22}^* = C_{33}^*$, $C_{55}^* = C_{66}^*$ due to the cubic symmetry, but $C_{44}^* \neq \frac{1}{2}(C_{22}^* - C_{23}^*)$ due to the absence of isotropy in the $x_2 - x_3$ plane. These principal stiffness matrix elements can be used in the transformation equations

$$
\bar{\mathbf{C}}^*(\theta) = \mathbf{T}_1 \mathbf{C}^* \mathbf{T}_2^{-1}
\tag{75}
$$

to generate the corresponding homogenized stiffness matrix elements of the effective medium in the rotated coordinate system independently of the micromechanics-based solution for the homogenized stiffness matrix of a repeating unit cell in the rotated coordinate system. The transformation matrices $\mathbf{T}_1$ and $\mathbf{T}_2$ for rotation by the angle θ about the x_1 axis are,

$$
\mathbf{T}_1 = \begin{bmatrix}
1 & 0 & 0 & 0 & 0 & 0 \\
0 & m^2 & n^2 & 2mn & 0 & 0 \\
0 & n^2 & m^2 & -2mn & 0 & 0 \\
0 & -mn & mn & m^2 - n^2 & 0 & 0 \\
0 & 0 & 0 & 0 & m & -n \\
0 & 0 & 0 & 0 & n & m
\end{bmatrix}, \quad
\mathbf{T}_2 = \begin{bmatrix}
1 & 0 & 0 & 0 & 0 & 0 \\
0 & m^2 & n^2 & mn & 0 & 0 \\
0 & n^2 & m^2 & -mn & 0 & 0 \\
0 & -2mn & 2mn & m^2 - n^2 & 0 & 0 \\
0 & 0 & 0 & 0 & m & -n \\
0 & 0 & 0 & 0 & n & m
\end{bmatrix}
$$

where $m = \cos\theta$ and $n = \sin\theta$. They relate stress and strain quantities in the principal coordinate system, $\boldsymbol{\sigma}$ and $\boldsymbol{\varepsilon}$, to the corresponding quantities in the rotated (primed) coordinate system, $\boldsymbol{\sigma}'$ and $\boldsymbol{\varepsilon}'$

$$\boldsymbol{\sigma}' = \mathbf{T}_1\boldsymbol{\sigma}, \qquad \boldsymbol{\varepsilon}' = \mathbf{T}_2\boldsymbol{\varepsilon}$$

and are used to derive Eq. (75) from Hooke's law in the principal material coordinate system. Under the above transformation, the homogenized stiffness matrix $\bar{\mathbf{C}}^*(\theta)$ acquires the following form in the rotated coordinate system

$$\bar{\mathbf{C}}^*(\theta) = \begin{bmatrix} \bar{C}_{11}^* & \bar{C}_{12}^* & \bar{C}_{13}^* & 0 & 0 & 0 \\ \bar{C}_{12}^* & \bar{C}_{22}^* & \bar{C}_{23}^* & \bar{C}_{24}^* & 0 & 0 \\ \bar{C}_{13}^* & \bar{C}_{23}^* & \bar{C}_{33}^* & \bar{C}_{34}^* & 0 & 0 \\ 0 & \bar{C}_{24}^* & \bar{C}_{34}^* & \bar{C}_{44}^* & 0 & 0 \\ 0 & 0 & 0 & 0 & \bar{C}_{55}^* & \bar{C}_{56}^* \\ 0 & 0 & 0 & 0 & \bar{C}_{56}^* & \bar{C}_{66}^* \end{bmatrix} \tag{76}$$

where $\bar{C}_{12}^* = \bar{C}_{13}^*$, $\bar{C}_{22}^* = \bar{C}_{33}^*$, $\bar{C}_{55}^* = \bar{C}_{66}^*$, and $\bar{C}_{24}^* = -\bar{C}_{34}^*$.

The knowledge of the effective stiffness matrix elements in the rotated coordinate system makes it possible to generate the corresponding transformed compliance matrix elements from the inverse relationship

$$\bar{\mathbf{S}}^*(\theta) = [\bar{\mathbf{C}}^*(\theta)]^{-1} \tag{77}$$

The transformed compliance matrix $\bar{\mathbf{S}}^*(\theta)$ has the same structural form as the stiffness matrix $\bar{\mathbf{C}}^*(\theta)$, with the individual elements $\bar{C}_{ij}^*(\theta)$ replaced by the corresponding elements $\bar{S}_{ij}^*(\theta)$. These elements, in turn, can be used to determine the effective engineering properties in the rotated coordinate system as follows

$$
\begin{aligned}
\bar{E}_{11}^*(\theta) &= \frac{1}{\bar{S}_{11}^*}, & \bar{E}_{22}^*(\theta) &= \frac{1}{\bar{S}_{22}^*}, & \bar{E}_{33}^*(\theta) &= \frac{1}{\bar{S}_{33}^*} \\
\bar{\nu}_{12}^*(\theta) &= -\frac{\bar{S}_{12}^*}{\bar{S}_{11}^*}, & \bar{\nu}_{13}^*(\theta) &= -\frac{\bar{S}_{13}^*}{\bar{S}_{11}^*}, & \bar{\nu}_{23}^*(\theta) &= -\frac{\bar{S}_{23}^*}{\bar{S}_{22}^*} \\
\bar{G}_{23}^*(\theta) &= \frac{1}{\bar{S}_{44}^*}, & \bar{G}_{13}^*(\theta) &= \frac{1}{\bar{S}_{55}^*}, & \bar{G}_{12}^*(\theta) &= \frac{1}{\bar{S}_{66}^*} \\
\bar{\eta}_{2,23}^*(\theta) &= \frac{\bar{S}_{24}^*}{\bar{S}_{44}^*}, & \bar{\eta}_{3,23}^*(\theta) &= \frac{\bar{S}_{34}^*}{\bar{S}_{44}^*}, & \bar{\eta}_{23,2}^*(\theta) &= \frac{\bar{S}_{24}^*}{\bar{S}_{22}^*}, & \bar{\eta}_{23,3}^*(\theta) &= \frac{\bar{S}_{34}^*}{\bar{S}_{33}^*}
\end{aligned} \tag{78}
$$

where $\bar{E}_{ii}^*(\theta)$ are the three Young's moduli, $\bar{\nu}_{ij}^*(\theta)$ ($i \neq j$) are the major Poisson's ratios, $\bar{G}_{ij}^*(\theta)$ $i \neq j$) are the three shear moduli, and $\bar{\eta}_{i,23}^*, \bar{\eta}_{23,i}^*$ are Lekhnitskii's coefficients of mutual influence of the 1st and 2nd kind, respectively, Lekhnitskii [30]. These coefficients provide a measure of the extent of anisotropy in the $x_2 - x_3$ plane introduced by the rotation angle θ about the fiber axis. The coefficients of the 1st kind represent ratios of transverse normal to transverse shear strains

due to transverse shear loading only. Similarly, the coefficients of the 2nd kind represent ratios of transverse shear to transverse normal strains due to transverse normal loading only.

In the following sections, we first determine the stiffness matrix elements of the two unidirectional composite systems in the principal material coordinate system by performing the high-fidelity micromechanical analysis on the simple repeating unit cell with the single fiber in the center, Fig. 3. We then use the values of these stiffness matrix elements, which have the form given by Eq. (74), in the transformation equations, Eqs. (75), to determine the homogenized stiffness matrix elements in the coordinate system rotated by the angle θ about the fiber axis in the range $0° \leq \theta \leq 45°$. These are then compared with the corresponding stiffness matrix elements obtained independently from the micromechanical analyses of the four remaining repeating unit cells in the rotated coordinate systems shown in Figs. 3 and 4. The determination of the engineering "constants" is then obtained by first determining the homogenized elastic compliance elements from Eq. (77), and then using the results in the definitions for engineering properties given by Eqs. (78).

In order to further demonstrate the need for the development of the high-fidelity micromechanics model, we compare the results generated in the manner described above with the corresponding results obtained from the re-formulated version of the original GMC model. The reformulated version is required due to the large number of subcells used in the constructed repeating unit cells. In addition, we compare the local stress fields under normal and shear loading in the different repeating unit cells predicted by the high-fidelity model with the original model.

4.1 Glass/Epoxy Unidirectional Composite

Figure 5 illustrates the dependence of the elastic stiffness matrix elements $\bar{C}_{ij}^*$ on the rotation angle θ for the glass/epoxy system with the Young's moduli ratio $E_f/E_m = 20$. The predictions generated by the high-fidelity model for the non-zero elastic stiffness matrix elements of the repeating unit cells shown in Fig. 4 have been normalized by the corresponding stiffness matrix elements C_{ij}^* obtained from the repeating unit cell in the principal material coordinate system (with $\theta = 0°$), with the exception of the $\bar{C}_{24}^*$ and $\bar{C}_{34}^*$ elements which have been normalized by C_{11}^*. The predictions of the original GMC model, which have also been normalized by the corresponding elements C_{ij}^* obtained from the high-fidelity model, are included in the figure. The actual values are given in the Appendix. As observed in the transformation equation results, while $\bar{C}_{11}^*$, $\bar{C}_{12}^*$, and $\bar{C}_{66}^*$ are insensitive to the rotation angle θ, the elements $\bar{C}_{22}^*$, $\bar{C}_{23}^*$, and $\bar{C}_{44}^*$ exhibit substantial dependence, with $\bar{C}_{23}^*$ and $\bar{C}_{44}^*$ increasing as much as 15% and 30%, respectively, as θ increases from 0° to 45°, and $\bar{C}_{22}^*$ decreasing by more than 5%. The dependence of the coupling elements $\bar{C}_{24}^*$ and $\bar{C}_{34}^*$ on the rotation angle is also dramatic, albeit the magnitudes are much smaller relative to C_{11}^*.

The high-fidelity model accurately captures the correct θ dependence of the effective stiffness matrix elements, noting that the vertical scale ranges in the individual figures have been deliberately chosen so as to highlight the differences between the micromechanics-based predictions and the transformation equations. The slight departures from the transformation equation predictions are
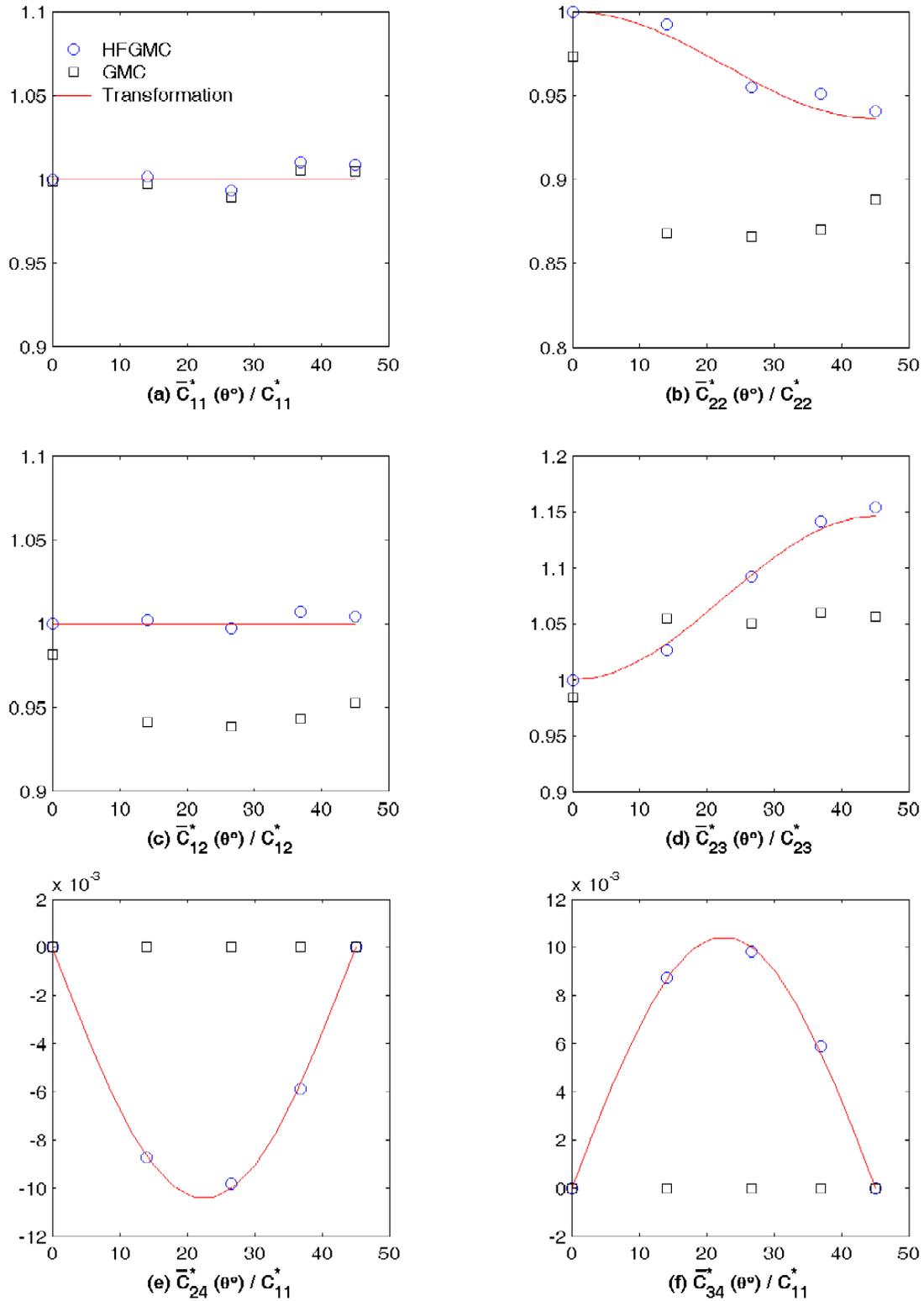
Figure 5. Normalized effective stiffness matrix elements $\bar{C}^{*}_{ij}$ of the glass/epoxy unidirectional composite as a function of the rotation angle θ about the fiber axis. Comparison of the original and the High-Fidelity GMC predictions with the transformation equations.
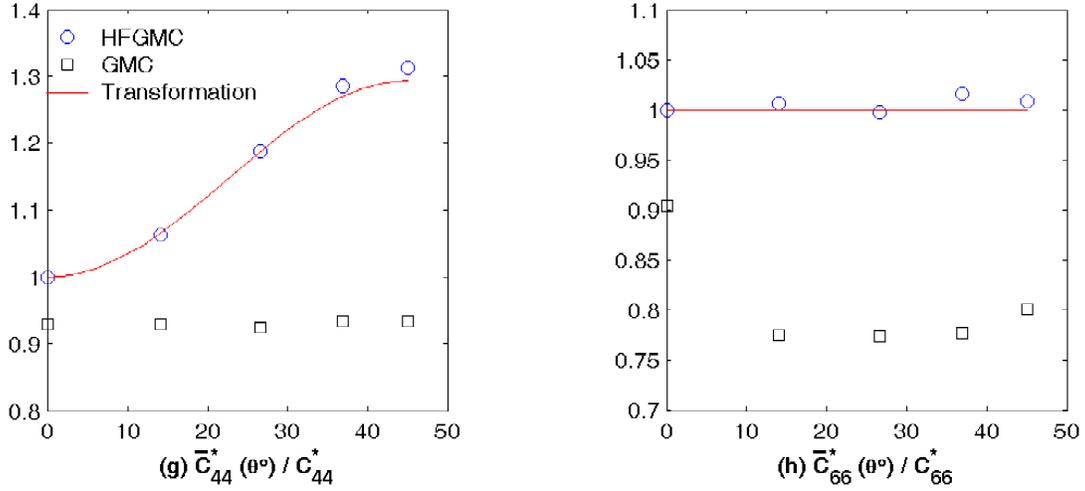
Figure 5. Continued.

most likely due to the small variations in the repeating unit cell fiber volume fractions and the somewhat different circular fiber approximations by the employed square subcell discretizations. It is remarkable, however, that the $\bar{C}_{24}^*$ and $\bar{C}_{34}^*$ behavior is captured so well in view of the relatively small magnitudes of these normal-shear coupling moduli. In contrast, the original GMC model is incapable of capturing the correct θ dependence of the elastic stiffness matrix elements with the exception of $\bar{C}_{11}^*$ which is theoretically insensitive to the rotation angle. In particular, the dependence of $\bar{C}_{22}^*$ is predicted to rapidly decrease with increasing θ and then increase in the considered range, which contrasts with the monotonically decreasing behavior exhibited by both the transformation equations and the high-fidelity model. Further, the actual magnitudes of this stiffness matrix element at the different off-axis angles are substantially lower relative to the high-fidelity model results, despite similar values for the repeating unit cell in the principal coordinate system ($\theta = 0°$). Similar anomalous behavior is observed in the remaining elements of the stiffness matrix which is further discussed below in the context of the engineering moduli. Of particular importance is the original GMC model's failure to correctly capture the anisotropic behavior due to the rotation angle manifested by the non-zero values of $\bar{C}_{24}^*$ and $\bar{C}_{34}^*$. The original model predicts that these elements are identically zero for all rotation angles, effectively suggesting that orthotropic behavior is preserved in the rotated coordinate systems.

The engineering moduli dependence on the rotation angle θ, calculated using Eqs. (77) and (78), for these repeating unit cells is illustrated in Fig. 6. As observed, the correlation between the high-fidelity model and transformation equation predictions is remarkable for the three Young's and shear moduli, and the three major Poisson's ratios. As expected, the axial Young's modulus $E_{11}^*(\theta)$ remains nearly constant for the differently-oriented repeating unit cells, as does the major Poisson's ratio $\nu_{12}^*(\theta)$ and the out-of-plane shear modulus $G_{12}^*(\theta)$. The in-plane moduli, on the

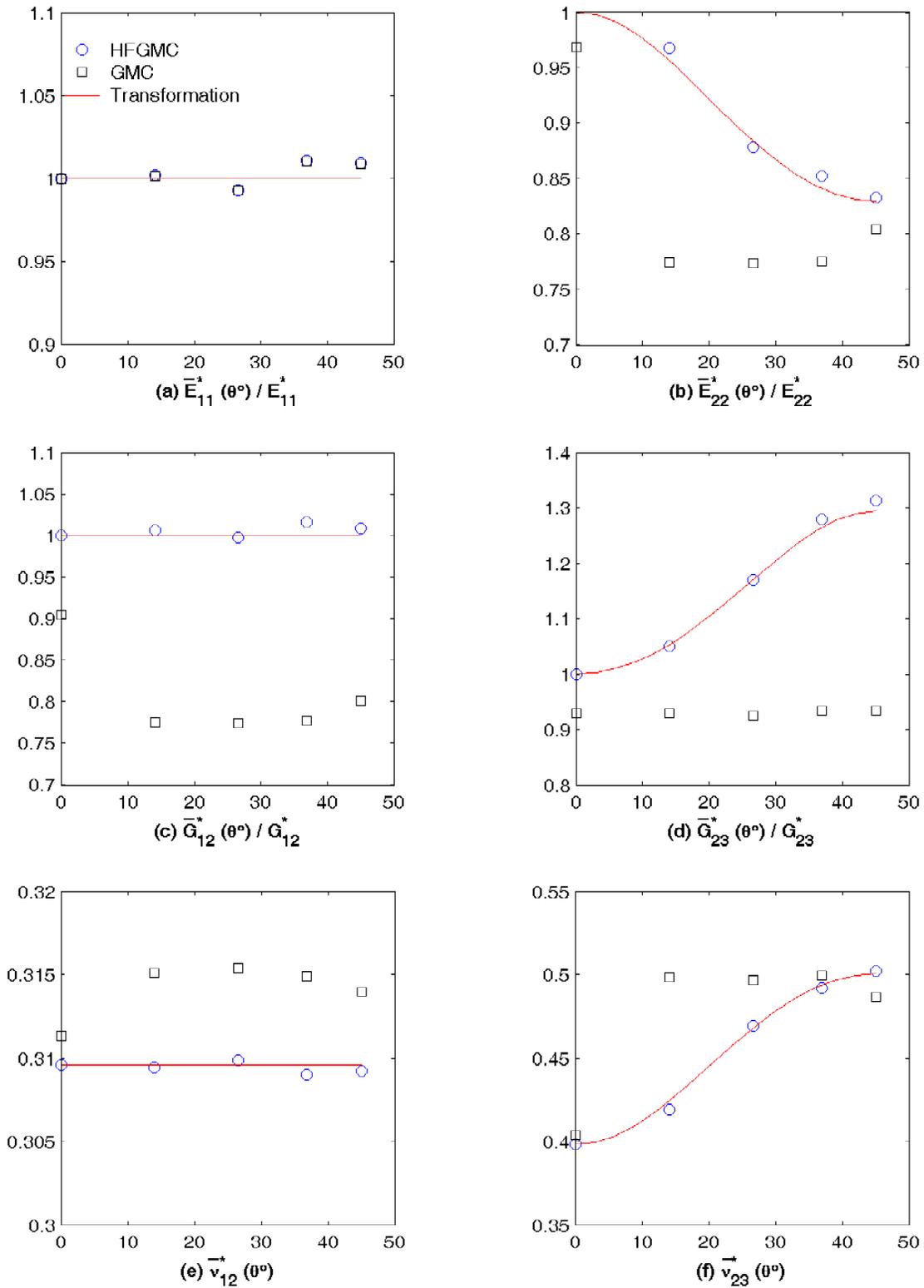Figure 6. Normalized engineering moduli of the glass/epoxy unidirectional composite as a function of the rotation angle θ about the fiber axis. Comparison of the original and the High-Fidelity GMC predictions with the transformation equations.
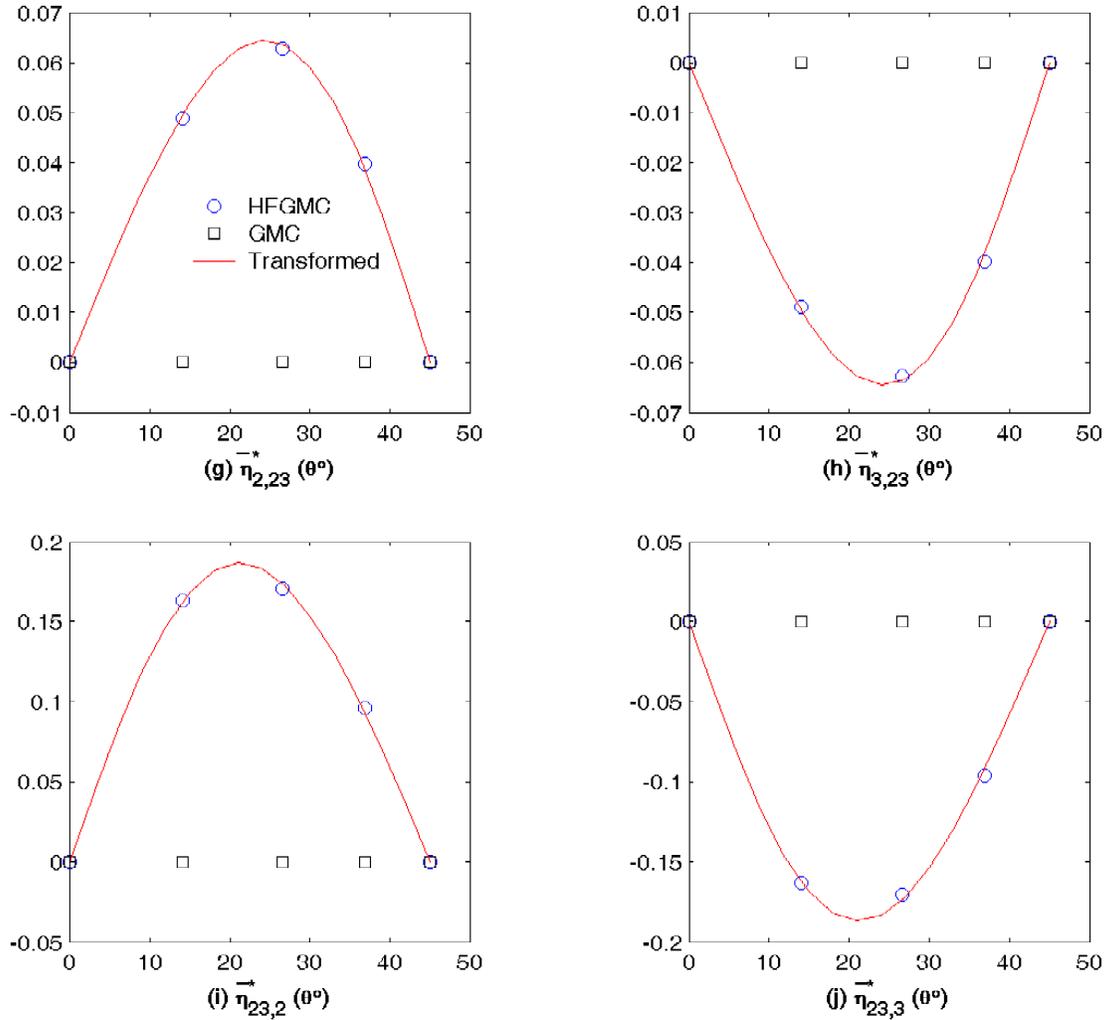
Figure 6. Continued.

other hand, exhibit substantial θ dependence. While the transverse modulus $E_{22}^*(\theta)$ decreases with increasing rotation angle, the transverse Poisson's ratio $\nu_{23}^*(\theta)$ and the transverse shear modulus $G_{23}^*(\theta)$ increase. For the rotation angle $\theta = 45°$, the decrease in the transverse Young's modulus is more than 15% of the principal material coordinate system value. For the same rotation angle, the increase in the transverse shear modulus and Poisson's ratio is more dramatic, with increases of approximately 30% and 25%, respectively. Equally remarkable is the correlation for the coefficients of mutual influence $\eta_{2,23}^*$, $\eta_{3,23}^*$, $\eta_{23,2}^*$, and $\eta_{23,3}^*$ which couple the normal and shear responses. These coefficients give a measure of the extent of anisotropy in the $x_2 - x_3$ plane caused by the absence of material planes of symmetry.

In contrast, the predictions of the original GMC model are quite poor, with the exception of the Young's modulus $E_{11}^*(\theta)$, as suggested by the results in Fig. 5. In particular, the transverse modulus $E_{22}^*(\theta)$ in the low off-axis angle range differs from the transformation and high-fidelity

model predictions by over 20% which is greater than the difference in the corresponding stiffness matrix element $\bar{C}^*_{22}$ in view of the pronounced differences in the transverse Poisson's ratio $\nu^*_{23}(\theta)$ in the low off-axis angle. The differences in the out-of-plane shear modulus $G^*_{12}(\theta)$ are also on the order of 20% in the entire off-axis range excluding $\theta = 0°$. An even greater difference is obtained for the transverse shear modulus $G^*_{23}(\theta)$ for rotation angles greater than 30° due to the original model's failure to predict any variation for all rotation angles. The differences between the high-fidelity and the original models is rooted in the absence of shear coupling due to the use of a linear displacement field in the original model, which results in constant strain and stress fields in the individual subcells. As discussed in the Introduction, the application of traction continuity conditions in an average sense between individual subcells in each row and column of subcells renders the corresponding traction components constant and their magnitudes are dictated by the most compliant subcell. In the case of the transverse shear stress this effect is further enhanced and results in a uniform shear stress throughout the entire repeating unit cell. The comparison of microscale stress fields discussed below illustrates this point more clearly.

To illustrate the influence of shear coupling, microscale stress distributions predicted by the high-fidelity and original models are compared for the repeating unit cell rotated by $\theta = 26.57°$ about the fiber axis and subjected to axial and transverse *normal* loading, and axial and transverse *shear* loading. Similar results have been observed for other rotation angles. Figure 7 compares the microscale σ_{11}, σ_{22} and σ_{23} stress fields in this repeating unit cell for uniaxial loading by the average axial normal strain $\bar{\varepsilon}_{11} = 0.1\%$, with the remaining faces of the repeating unit cell traction-free in the average sense. As observed, the axial σ_{11} stress distributions predicted by both models are nearly identical, thereby producing essentially the same values of the axial Young's modulus. This is not the case for the σ_{22} and σ_{23} stress distributions. In particular, the σ_{22} distribution predicted by original GMC model consists of parallel strips along the y_2 direction of the repeating unit cell, with the strips alternating in sign such that the average stress $\bar{\sigma}_{22}$ remains zero due to equilibrium considerations. The parallel strip pattern arises due to the fact that the normal stress σ_{22} is a traction component in each row of subcells along the y_2 direction, which must remain constant in that row due to the linear displacement field approximation in each subcell and the imposition of traction continuity in a surface-averaged sense across subcell interfaces. The actual magnitude of σ_{22} in each row is dictated by the relative content of the individual phases in that row, which represents the actual fiber arrangement only in a very approximate manner. This is a direct consequence of the lack of shear coupling and clearly reveals GMC to be a spring-like model with coupling only among the normal stress (strain) components. The absence of shear coupling results in the vanishing of the transverse shear stress σ_{23} predicted by GMC in view of the vanishing of the average transverse shear stress on the external faces of each boundary subcell. In contrast, the high-fidelity model predictions of the microscale σ_{22} and σ_{23} stress distributions are consistent with the actual fiber arrangement. In particular, the distributions of both stress components within the individual fibers exhibit small departures from uniform distributions (as would be expected for the
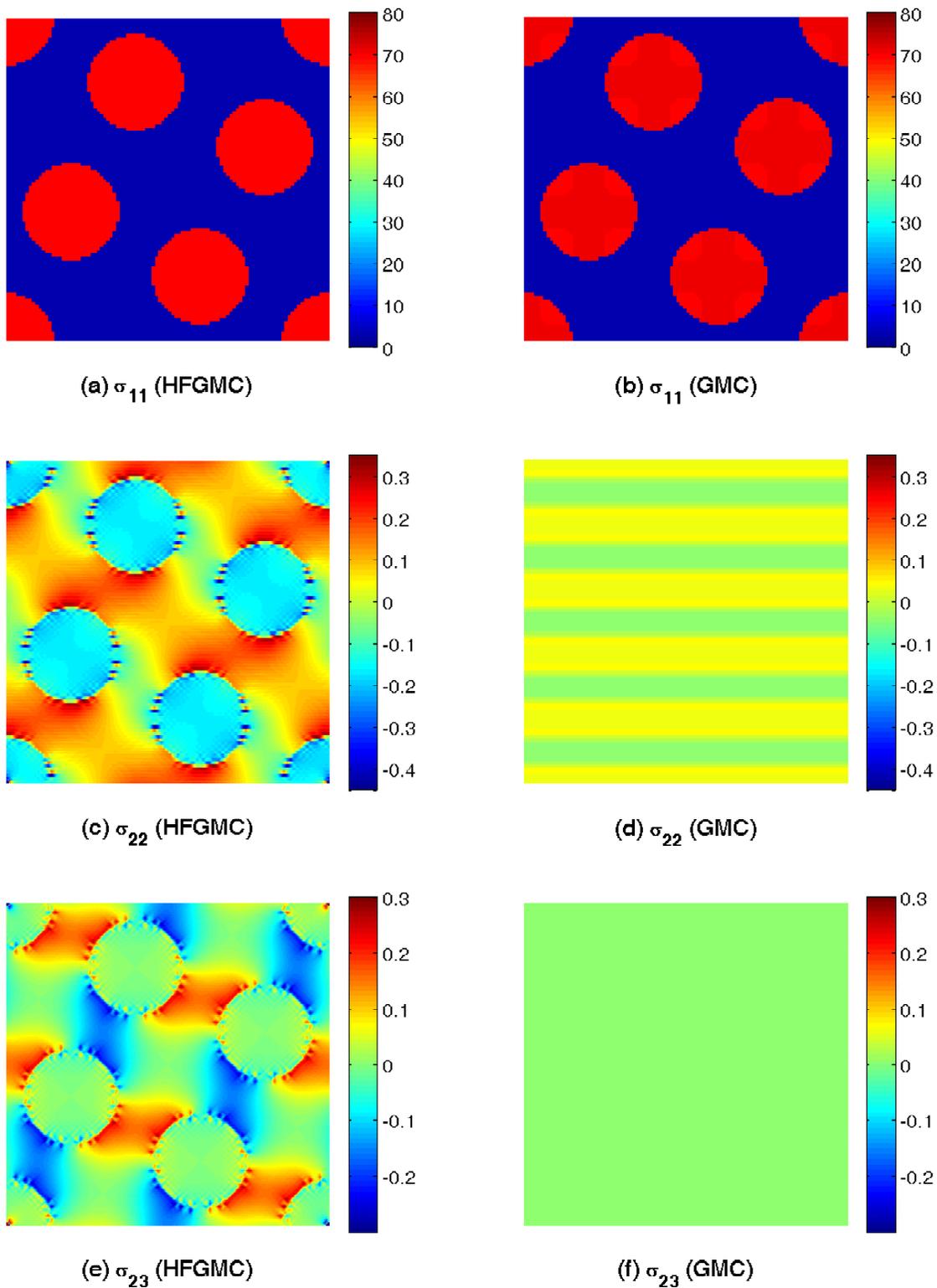
Figure 7. Comparison of the σ_{11}, σ_{22} and σ_{23} stress fields within the repeating unit cell of the glass/epoxy composite rotated by 26.57° about the fiber axis and subjected to the average axial normal strain $\bar{\varepsilon}_{11} = 0.1\%$. High-Fidelity (left column) vs original GMC (right column) predictions.

dilute case), with highly nonuniform distributions in the matrix phase which follows the geometric fiber pattern. Substantially higher magnitudes of these stress components relative to the GMC predictions, characterized by localized stress concentrations along the fiber/matrix interfaces, are observed due to the fiber/matrix elastic moduli mismatch and geometric fiber arrangement. It is remarkable that the transverse normal and shear stress components, induced by the application of just the axial stress, are reproduced with such good fidelity despite their substantially smaller magnitudes relative to the axial stress σ_{11}.

Figure 8 compares the microscale σ_{12} and σ_{13} stress fields in this repeating unit cell for loading by the average axial shear strain $\bar{\varepsilon}_{12} = 0.1\%$, with the remaining faces of the repeating unit cell traction-free in the average sense. In the case of the σ_{12} stress component, the high-fidelity model predicts small departures from uniform stress distributions within the individual fibers, with magnitudes substantially greater than in the surrounding matrix due to the large fiber/matrix moduli mismatch. High stress concentrations are evident along certain segments of the fiber/matrix interfaces which may or may not be due to the step-wise discretization of the circular interface. This aspect requires further investigation which is beyond the scope of the present study (see Bednarcyk et al. [25] for related discussion about the mesh sensitivity of HFGMC). The σ_{13} stress distributions within the individual fibers also exhibit small departures from uniform distributions, although their magnitudes are nearly zero. In the matrix phase, however, this stress component is not insignificant relative to σ_{12}. In contrast, the σ_{12} distribution predicted by the original GMC model consists of a parallel strip pattern along the y_2 axis, as was the case with the σ_{22} distribution for loading by the axial normal stress. Significantly lower magnitudes, with little variation from strip to strip, are observed in the σ_{12} distribution due to the weakest link effect caused by the application of the traction continuity conditions in an average sense in the presence of constant subcell stress field. This produces significantly lower axial shear modulus as already observed in Fig. 6. Further, while the high-fidelity model predicts the presence of non-zero σ_{13}, this stress component is zero according to the original model.

Figure 9 compares the microscale σ_{22}, σ_{33} and σ_{23} stress fields in this repeating unit cell for loading by the average transverse normal strain $\bar{\varepsilon}_{22} = 0.1\%$, with the remaining faces of the repeating unit cell traction-free in the average sense. The σ_{22} stress distribution predicted by the high-fidelity model is qualitatively similar to the σ_{12} distribution of the preceding example, while the σ_{33} stress distribution is similar to σ_{13}. Significant σ_{33} stress concentrations are present in the matrix phase at the fiber/matrix interfaces at points along the fiber diametral planes lined up with the load axis. Significant σ_{23} stress magnitudes are also evident in oval regions surrounded by four fibers aligned with the rotated fiber rows. In contrast, and as expected from the previous results, the normal σ_{22} and σ_{33} stress distributions generated by the original GMC model exhibit parallel strip patterns along the y_2 and y_3 directions, respectively. Little variation in the respective stress magnitudes is observed in the adjacent strips and the low magnitudes relative to the high-fidelity results produce a low value of the average normal stress $\bar{\sigma}_{22}$, thereby resulting in a low value of the
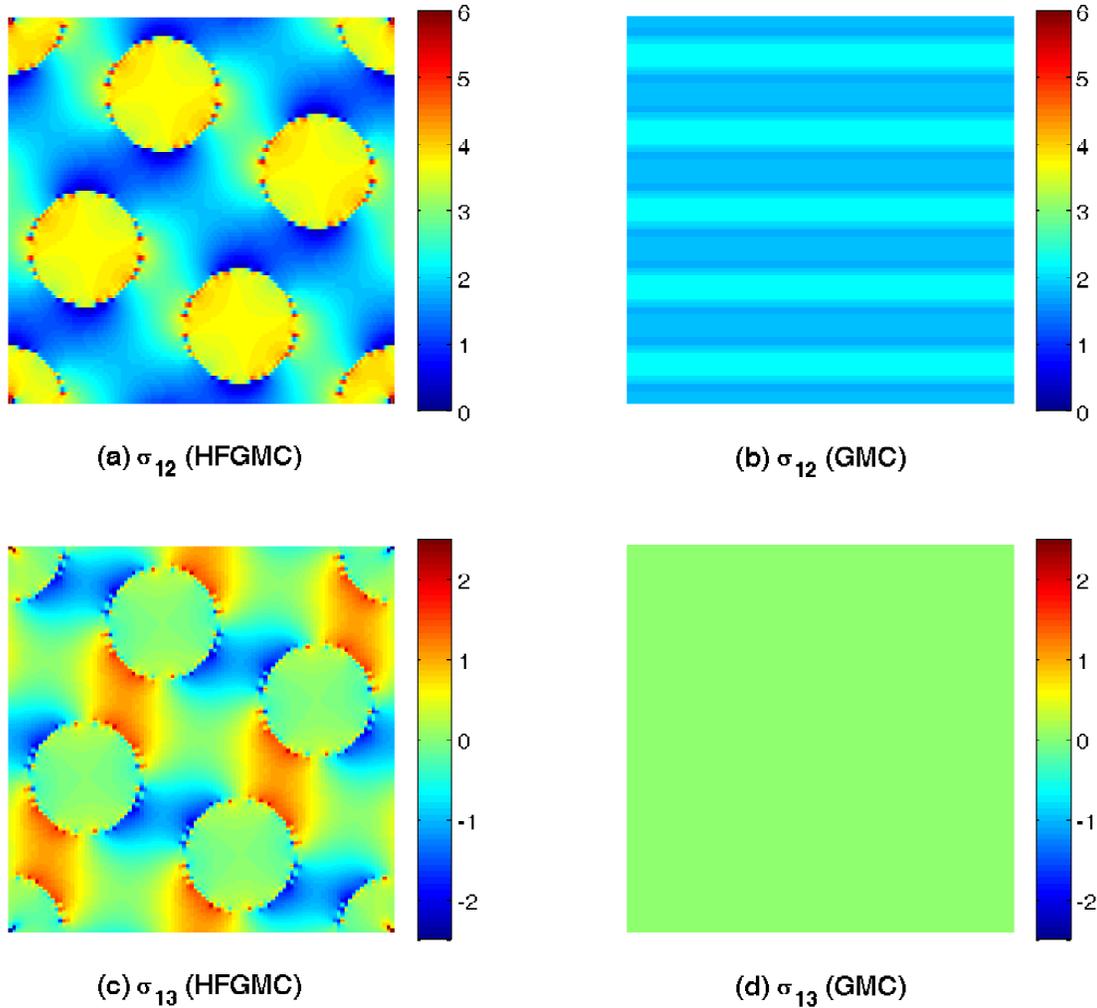
Figure 8. Comparison of the σ_{12} and σ_{13} stress fields within the repeating unit cell of the glass/epoxy composite rotated by 26.57° about the fiber axis and subjected to the average axial shear strain $\bar{\varepsilon}_{12} = 0.1\%$. High-Fidelity (left column) vs original GMC (right column) predictions.

transverse Young's modulus for this rotation angle observed in Fig. 6. Further, the transverse shear stress σ_{23} is identically zero due to the absence of shear coupling.

Finally, Figure 10 compares the microscale σ_{23} and σ_{22} stress fields in this repeating unit cell for loading by the average transverse shear strain $\bar{\varepsilon}_{23} = 0.1\%$, with the remaining faces of the repeating unit cell traction-free in the average sense. This loading case highlights the differences in the two stress distributions predicted by the original and the high-fidelity GMC models. The uniform σ_{23} stress distribution throughout the entire repeating unit cell irrespective of location (i.e., whether the particular point lies within the hard fiber or much softer matrix phase) predicted by the original GMC model is a direct consequence of the imposition of shear traction continuity in the surface-average sense across subcell interfaces in the y_2 and y_3 directions, given the linear

Figure 9. Comparison of the σ_{22}, σ_{33} and σ_{23} stress fields within the repeating unit cell of the glass/epoxy composite rotated by 26.57° about the fiber axis and subjected to the average transverse normal strain $\bar{\varepsilon}_{22} = 0.1\%$. High-Fidelity (left column) vs original GMC (right column) predictions.
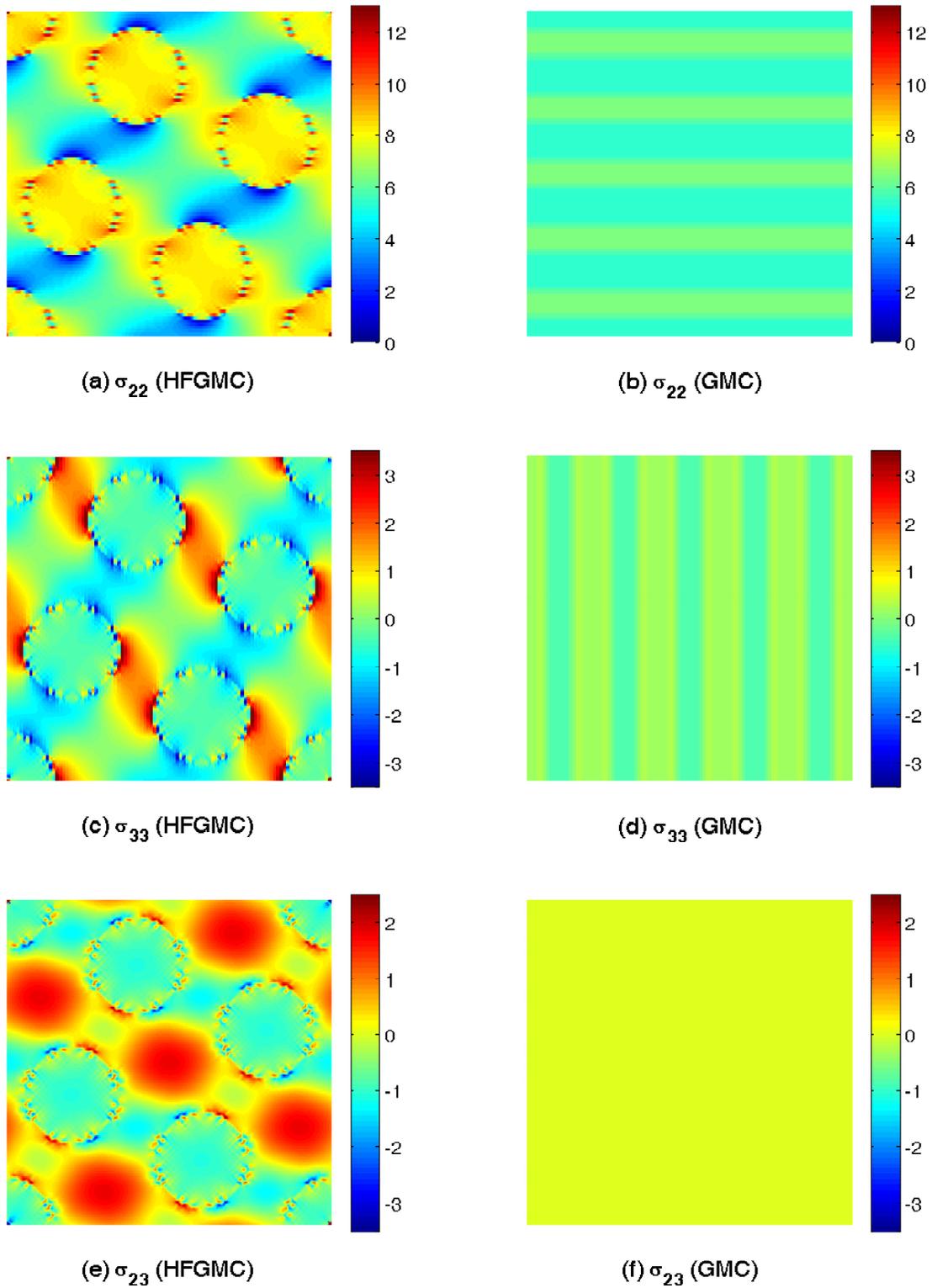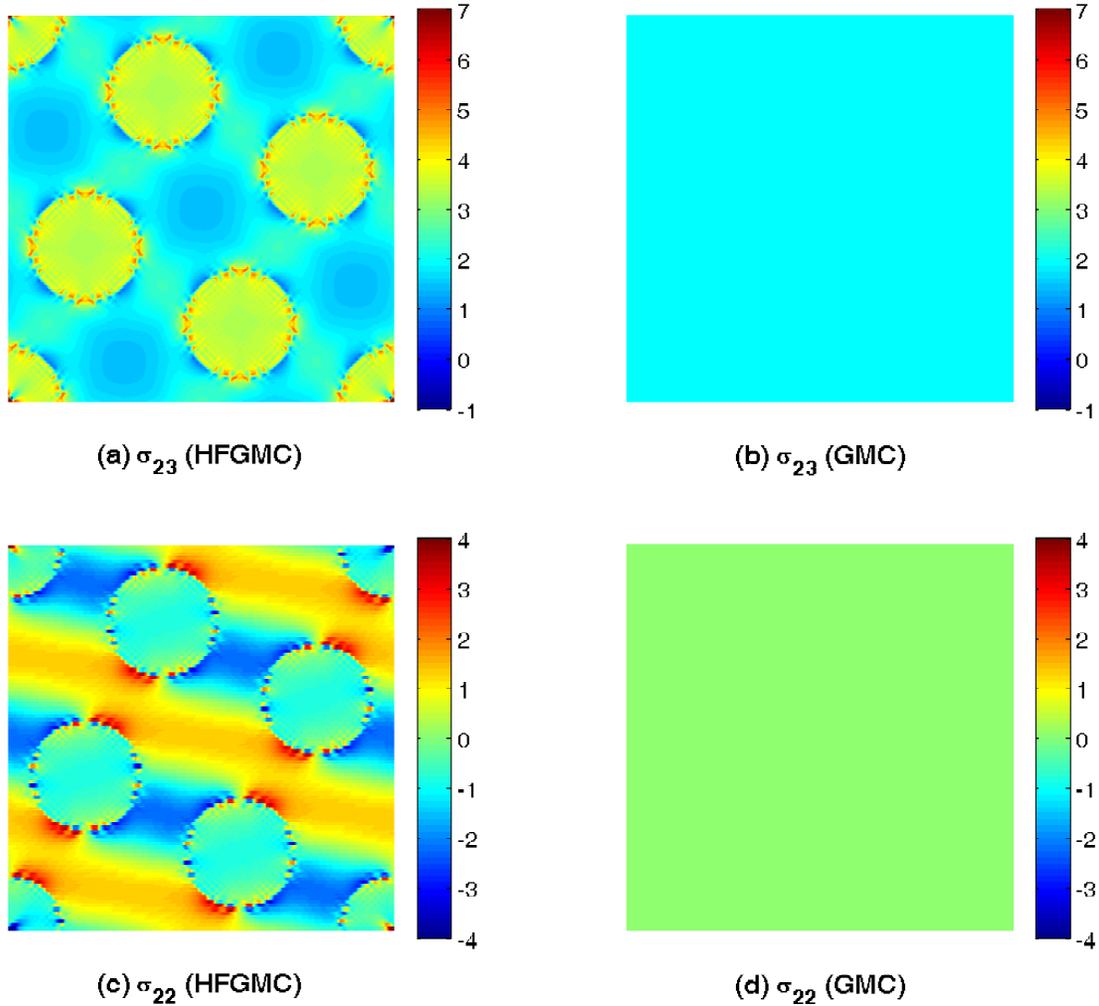
Figure 10. Comparison of the σ_{23} and σ_{22} stress fields within the repeating unit cell of the glass/epoxy composite rotated by $26.57°$ about the fiber axis and subjected to the average transverse shear strain $\bar{\varepsilon}_{23} = 0.1\%$. High-Fidelity (left column) vs original GMC (right column) predictions.

displacement field approximation within each subcell. The low magnitude of this stress component relative to the high-fidelity prediction produces a substantially lower value of the transverse shear modulus observed in Fig. 6. The linear displacement field approximation also uncouples the shear and normal stress fields at the local level, thereby producing vanishing σ_{22} stresses in the individual subcells. In contrast, the second-order displacement field approximation employed by the high-fidelity model is sufficient to correctly capture the stress transfer mechanism between the two phases, enabling the fibers to carry substantially higher shear stresses, thereby producing a higher average shear stress that the repeating unit cell can support for the same applied average shear strain. This results in the higher effective transverse shear modulus seen in Fig. 6. The

second-order displacement field approximation also couples the normal and shear stress fields at the local level, resulting in the observed σ_{22} stress distribution which is nearly uniform in the individual fibers and highly nonuniform in the matrix phase. The matrix σ_{22} stress nonuniformity is characterized by substantial stress concentrations at opposite locations around the fiber/matrix interface that are aligned with the diametral fiber planes coincident with the rotated fiber rows.

4.2   Aluminum Weakened by Axially Oriented Cylindrical Porosities

Figures 11 through 16 present the corresponding results for the aluminum matrix with substantially softer cylindrical inclusions, with the actual stiffness matrix and engineering moduli values given in the Appendix. In this case, the Young's moduli ratio is $E_f/E_m = 0.01$. For such a low ratio, the compliant cylindrical inclusions effectively behave as porosities.

Figure 11 illustrates the dependence of the elastic stiffness matrix elements $\bar{C}_{ij}^*$ on the rotation angle θ. The transformation equation predictions follow the trends presented in Fig. 5 for the glass/epoxy composite, but the variations are greater. In particular, the presence of porosities produces a degradation in $\bar{C}_{22}^*$ greater than 15% as the rotation angle increases from $0°$ to $45°$, which is roughly three times larger than the corresponding 5% decrease observed for the glass/epoxy system. The increases in the $\bar{C}_{23}^*$ and $\bar{C}_{44}^*$ stiffness elements, which are more than 50% and nearly 100% respectively, are also substantially greater relative to the glass/epoxy system. The normal/shear coupling elements $\bar{C}_{24}^*$ and $\bar{C}_{34}^*$ also experience greater variations, with the maximum values being approximately five-fold greater relative to the glass/epoxy composite. The high-fidelity GMC model predictions follow the transformation equation variations very closely, with the observed small departures most likely due to the small variations in the porosity content among the five different repeating unit cells containing different numbers of porosities.

In contrast, the original GMC model is not capable of accurately predicting the magnitude and variation of any of the stiffness elements with the rotation angle. The determination of the individual stiffness matrix elements involves the application of one nonzero macroscopic strain component at a time which gives rise to tractions whose line of action traverses the porous or compliant phase even in the case of the axial strain. Under transverse loading, the stress cannot be transferred effectively around the compliant inclusions due to the absence of shear coupling, and the load supported by any row of subcells coincident with the applied load is governed by the most compliant subcell in that row. This produces substantial degradation in the values of the stiffness elements in the principal coordinate system, which is greatly compounded by the rotation angle, including the $\bar{C}_{11}^*$ stiffness element which was so accurately predicted for the glass/epoxy composite. It is clear that for this porous material, the original GMC predictions for all stiffness matrix elements at any non-zero rotation angle are either significantly different or completely erroneous. It is only for the stiffness elements which directly relate the normal stress-strain pairs at the zero rotation angle, C_{11}^*, C_{22}^*, and the axial shear pairs, C_{55}^*, C_{66}^*, that the predictions are not dramatically different. In contrast, the stiffness element that relates the transverse shear stress-strain pair, C_{44}^*, is completely
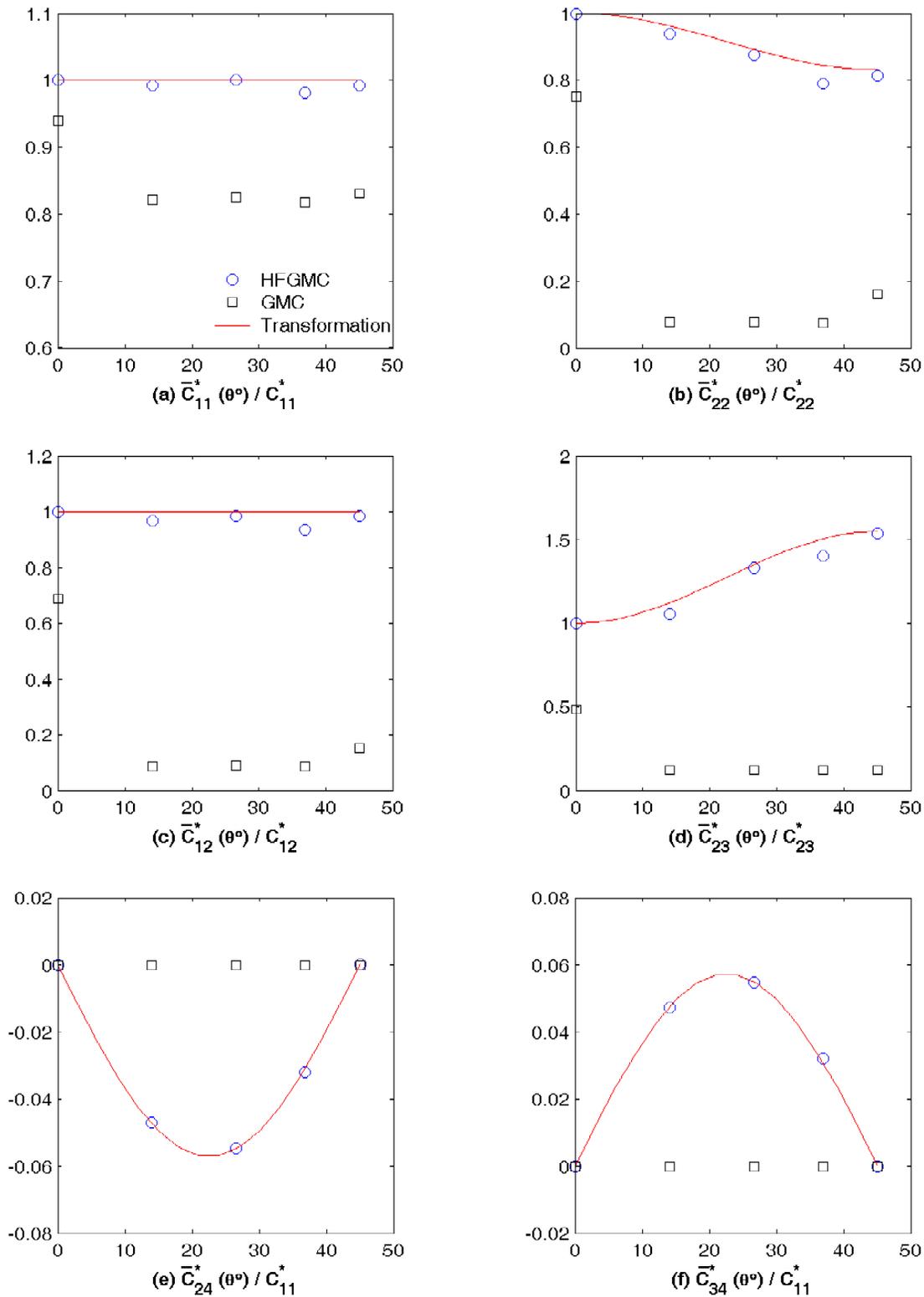
Figure 11. Normalized effective stiffness matrix elements $\bar{C}_{ij}^*$ of the aluminum matrix weakened by cylindrical porosities as a function of the rotation angle θ about the porosity axis. Comparison of the original and the High-Fidelity GMC predictions with the transformation equations.
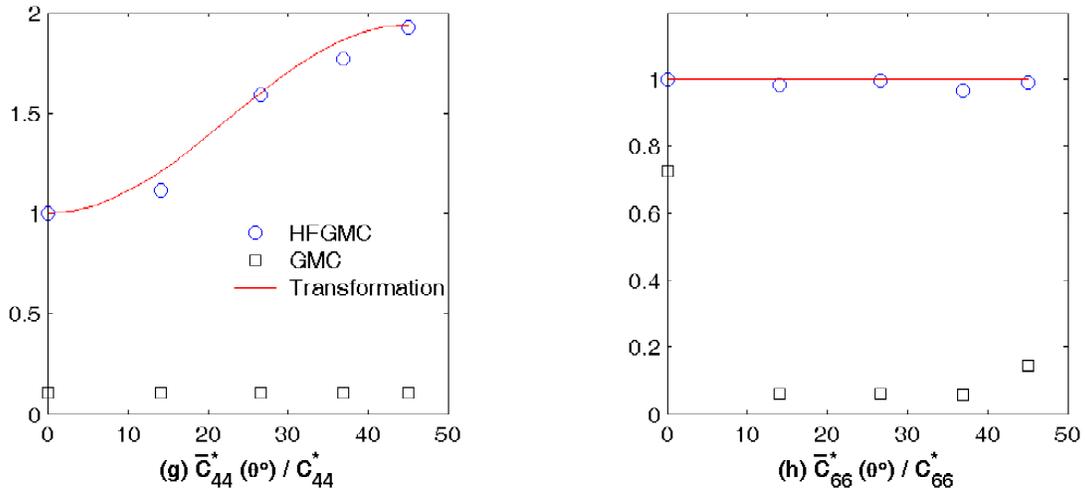
Figure 11. Continued.

erroneous even at the zero rotation angle. This will be further examined in the Discussion section in the context of using an alternative method to determine the off-axis stiffness element behavior using the original GMC model.

The greater variations in the elastic stiffness matrix elements with the rotation angle for this material system translate into correspondingly greater moduli variations shown in Fig. 12. As in the case of the glass/epoxy composite, the transformation equations predict variations only for the transverse moduli and the normal/shear coupling coefficients. In particular, the transverse modulus $\bar{E}_{22}^*(\theta)$ decreases by nearly 40% at the rotation angle of $45°$ relative to its value in the principal material coordinate system, compared to just a little more than 15% for the glass/epoxy system. The increase in the transverse modulus $\bar{G}_{23}^*(\theta)$ is almost 100%, which is the same as the increase in $\bar{C}_{44}^*(\theta)$. The increase in the transverse Poisson's ratio $\bar{\nu}_{23}^*(\theta)$ is even more dramatic, being around 150%. These large variations with the rotation angle are captured very well by the high-fidelity GMC model, as expected from the stiffness matrix element results. In contrast, the original GMC model results are completely erroneous for almost all engineering moduli at non-zero rotation angles as also suggested by the preceding stiffness matrix element results. The exception is the axial Young's modulus $\bar{E}_{11}^*(\theta)$ and the related Poisson's ratio $\bar{\nu}_{12}^*$ which are predicted very accurately for all rotation angles. In the case of pure axial loading in the porosity direction, the matrix phase is continuous along this direction, and thus effective in supporting the entire axial load without the need for stress transfer through the shear-normal coupling mechanism, while the transverse contraction which affects $\bar{\nu}_{12}^*$ occurs unconstrained due to porosity's presence.

The above results are explained by microscale stress distributions predicted by the high-fidelity and original models presented in Figs. 13 through 16. As in the case of the glass/epoxy composite, these distributions have been generated for the repeating unit cell rotated by $\theta = 26.57°$ and
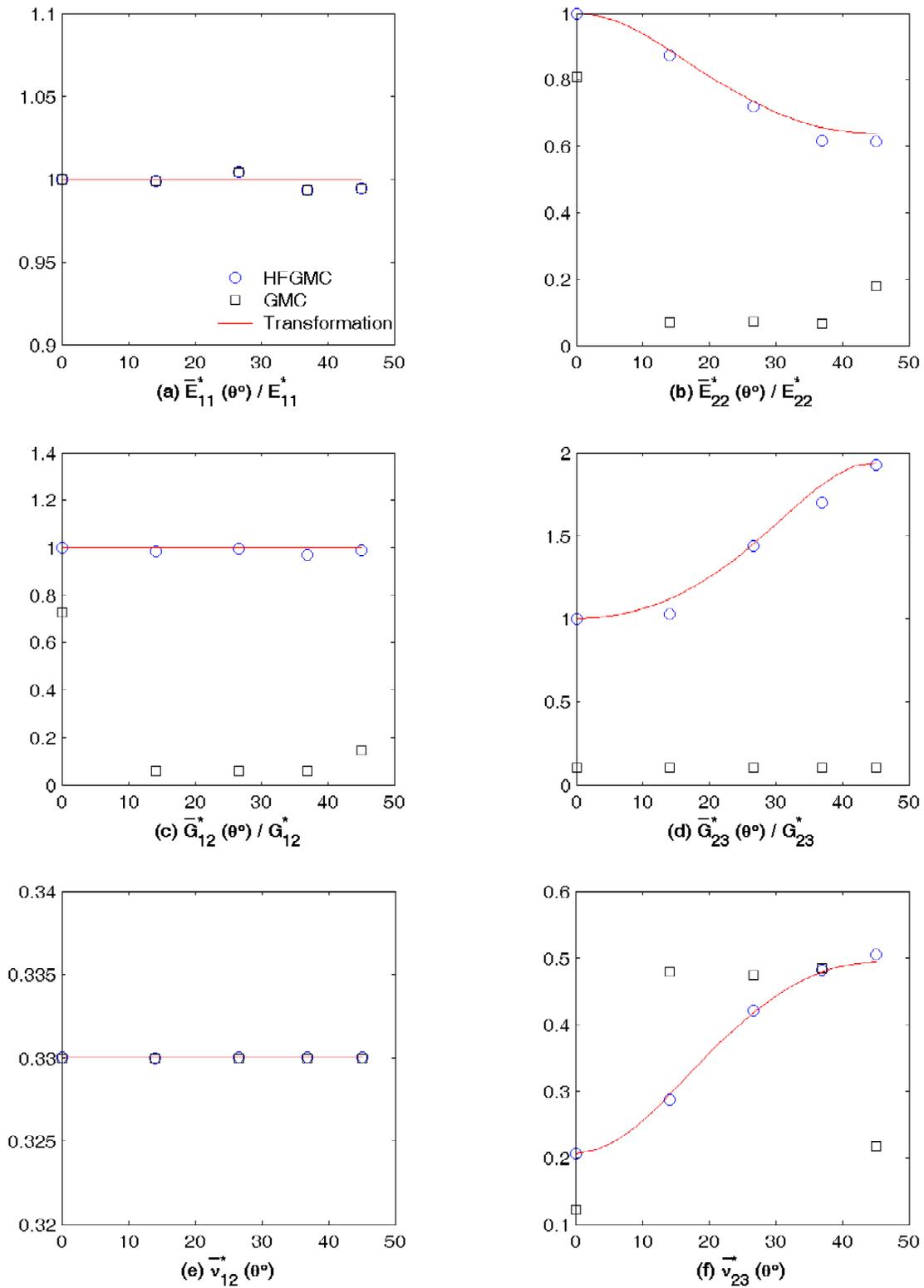
Figure 12. Normalized engineering moduli of the aluminum matrix weakened by cylindrical porosities as a function of the rotation angle θ about the porosity axis. Comparison of the original and the High-Fidelity GMC predictions with the transformation equations.
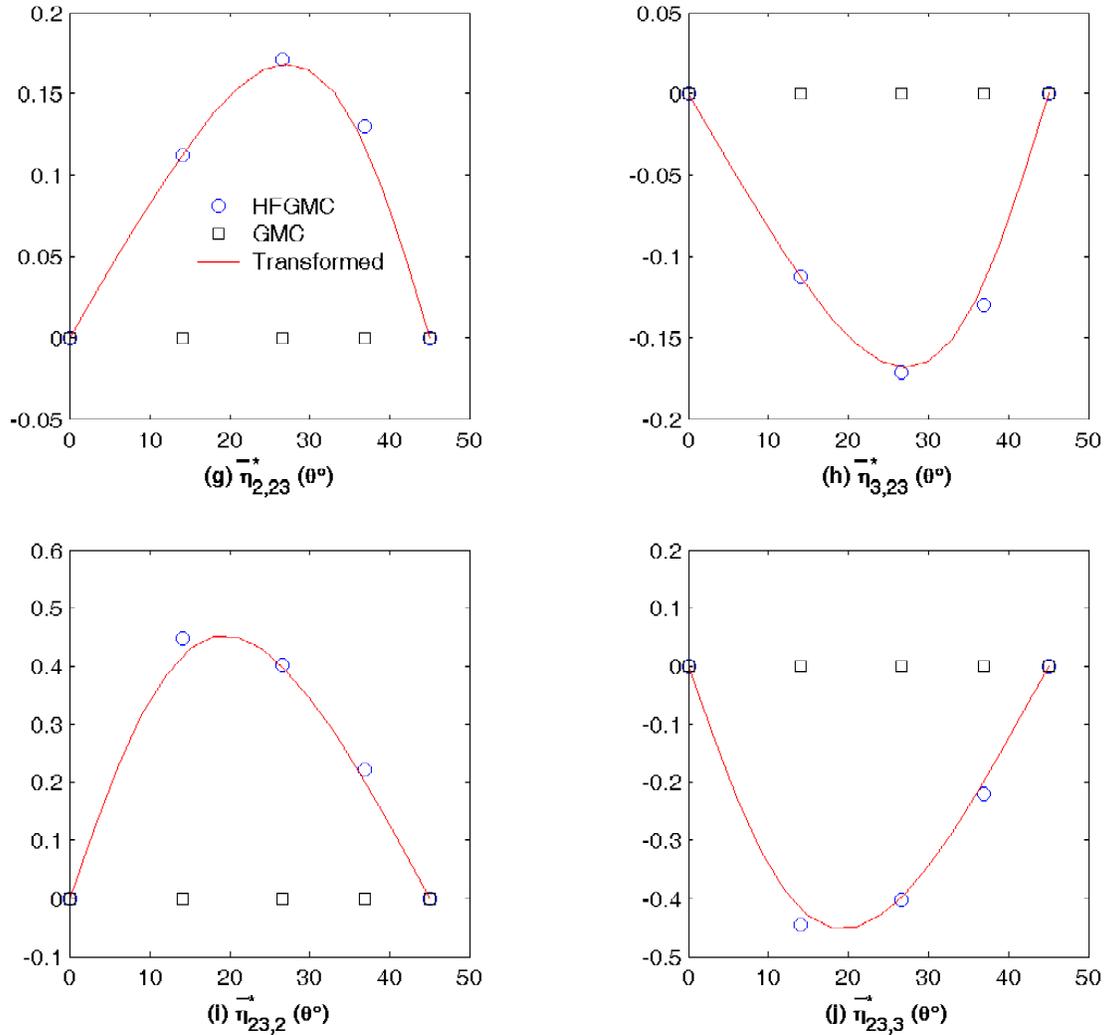
Figure 12. Continued.

subjected to axial and transverse normal loading, and transverse and axial shear loading. Figure 13 compares the microscale σ_{11}, σ_{22} and σ_{23} stress fields in this repeating unit cell for loading by the average axial normal strain $\bar{\bar{\varepsilon}}_{11} = 0.1\%$, with the remaining faces of the repeating unit cell traction-free in the average sense. As in the preceding case, virtually no difference is observed in the σ_{11} stress distributions predicted by both models. In contrast to the preceding case, no differences are observed in the σ_{22} and σ_{23} stress fields as well. These stress components are, in fact, very small due to the absence of constraint on the transverse deformation of the matrix under pure axial loading in the presence of porosities. This lack of constraint allows the matrix phase to contract freely without inducing transverse normal and shear stresses. This is one instance when the original GMC model correctly predicts the microscale stress fields which, in turn, produce the correct variation in the axial modulus $\bar{E}_{11}^*(\theta)$.
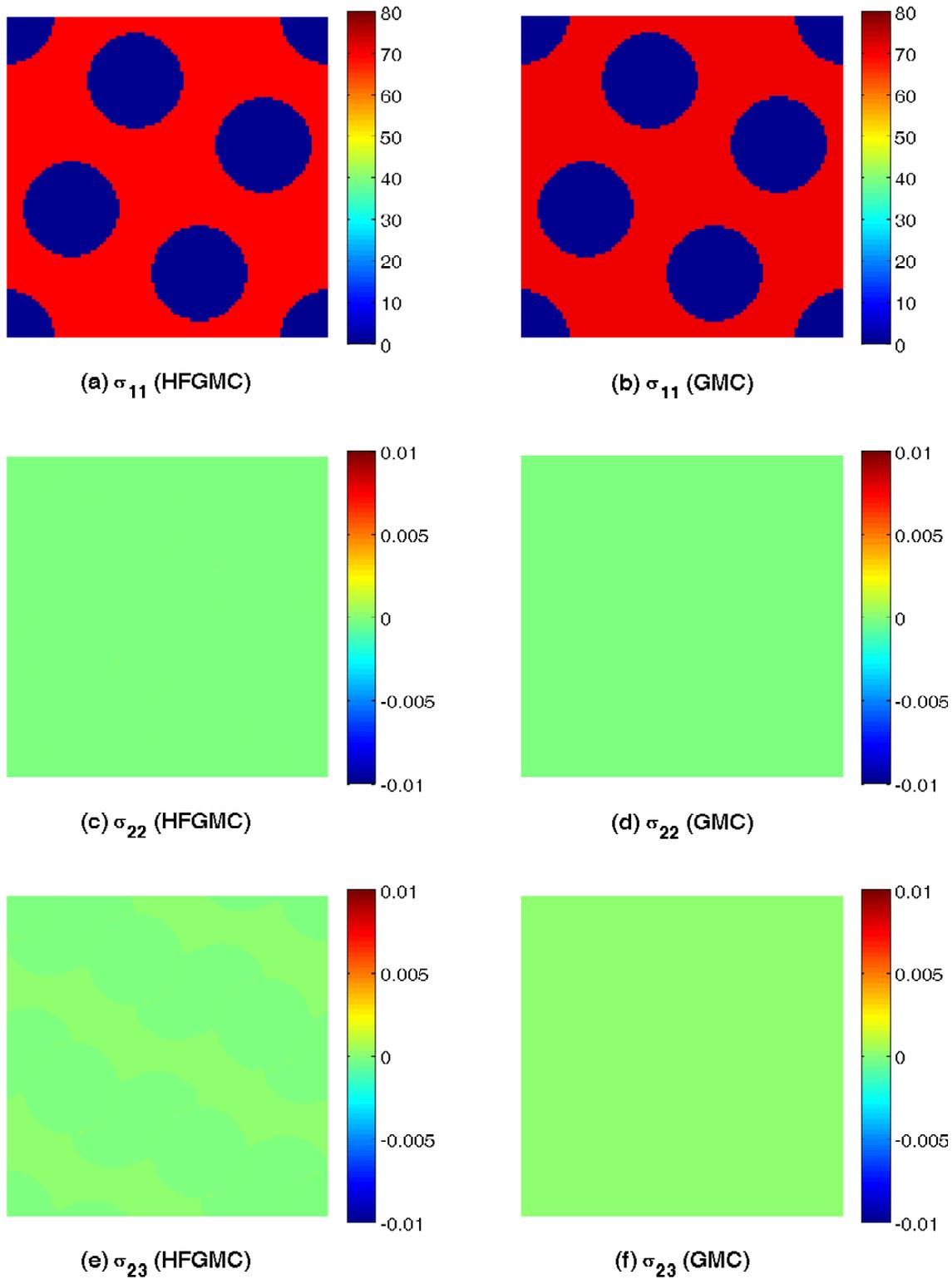
Figure 13. Comparison of the σ_{11}, σ_{22} and σ_{23} stress fields within the repeating unit cell of porous aluminum matrix rotated by 26.57° about the porosity axis and subjected to the average axial normal strain $\bar{\varepsilon}_{11} = 0.1\%$. High-Fidelity (left column) vs original GMC (right column) predictions.

(a) σ_{12} (HFGMC)

(b) σ_{12} (GMC)

(c) σ_{13} (HFGMC)

(d) σ_{13} (GMC)

Figure 14. Comparison of the σ_{12} and σ_{13} stress fields within the repeating unit cell of porous aluminum matrix rotated by $26.57°$ about the porosity axis and subjected to the average axial shear strain $\bar{\varepsilon}_{12} = 0.1\%$. High-Fidelity (left column) vs original GMC (right column) predictions.

Figure 14 compares the microscale σ_{12} and σ_{13} stress fields in this repeating unit cell for loading by the average axial shear strain $\bar{\varepsilon}_{12} = 0.1\%$, with the remaining faces of the repeating unit cell traction-free in the average sense. While the compliant inclusions or porosities cannot support appreciable axial shear stresses, the matrix phase does support these stress components. This is correctly predicted by the high-fidelity model where appreciable levels of both stress components are carried by the matrix phase. The highly nonuniform stress distributions are a direct result of the shear coupling effect which is responsible for transferring the two stress components around porosities. This stress transfer mechanism is absent in the original GMC model, resulting in very low values of the axial shear stress σ_{12} (noting that the axial shear modulus $\bar{G}^*_{12}(\theta)$ is not quite zero), and zero values of the axial shear stress σ_{13} due to decoupling of the axial shear response in the $y_1 - y_2$ and $y_1 - y_3$ planes in the case of isotropic or orthotropic phases.

Figure 15 compares the microscale σ_{22}, σ_{33} and σ_{23} stress fields in this repeating unit cell for loading by the average transverse normal strain $\bar{\varepsilon}_{22} = 0.1\%$, with the remaining faces of the repeating unit cell traction-free in the average sense. The detrimental effect of the shear coupling's absence in the original GMC model on these stress components is clearly observed, with the σ_{22} stress field characterized by essentially uniform and very low magnitudes, and thus a low transverse Young's modulus $\bar{E}_{22}^*(\theta)$ seen in Fig. 12. The same holds true for the σ_{33} stress field, while the transverse shear stress σ_{23} vanishes completely. In contrast, the shear coupling effects necessary to internally support the applied transverse load are clearly evident in the high-fidelity GMC model predictions for the three stress fields. Highly nonuniform distributions are observed for the three stress components in the matrix phase, characterized by significant concentrations at the fiber/matrix interfaces at specific locations as in the preceding case.

Similar trends in the stress distributions predicted by the two models are observed for loading by the average transverse shear strain $\bar{\varepsilon}_{23} = 0.1\%$, with the remaining faces of the repeating unit cell traction-free in the average sense. This is seen Fig. 16 which compares the microscale σ_{23} and σ_{22} stress fields within the considered repeating unit cell. Interestingly, large concentrations of the normal stress σ_{22} are observed at the fiber/matrix interface due to the transverse shear loading in the high-fidelity GMC model predictions. These are higher than the corresponding transverse shear stress concentrations. The original GMC model is incapable of capturing these nonuniform stress fields due to the absence of shear coupling, and the presence of porosities results in uniform and very low magnitudes of the transverse shear stress, producing a very low value of the transverse shear modulus $\bar{G}_{23}^*(\theta)$ seen in Fig. 12. Furthermore, the normal stress σ_{22} which exhibits high stress concentrations observed in the high-fidelity result completely vanishes according to the original GMC model.

5 DISCUSSION

As illustrated in the foregoing, for a repeating unit cell without planes of material symmetry parallel to the fiber axis the microscale stress fields predicted by the original GMC model exhibit two characteristic patterns in the plane normal to the fiber axis. The normal σ_{22} and σ_{33} stress distributions are characterized by parallel strips whose magnitude and sign depends on the applied stress orientation and the fiber/matrix Young's modulus ratio. For large ratios the pattern is pronounced while for very low ratios which mimic porosities the patterns are obscured by the very low normal stress magnitudes. Similar strip patterns are observed for repeating unit cells with a single fiber in the center, which possess two orthogonal planes of material symmetry, Bednarcyk et al. [25] and Pindera et al. [26]. In such cases, the strip patterns are wider and fewer due to the absence of overlapping fibers aligned with the load axis. In contrast, the shear σ_{23} stress distributions are uniform within the rotated repeating unit cells as well as within unit cells in the principal material coordinate system. As discussed herein, and also elsewhere, these patterns are a
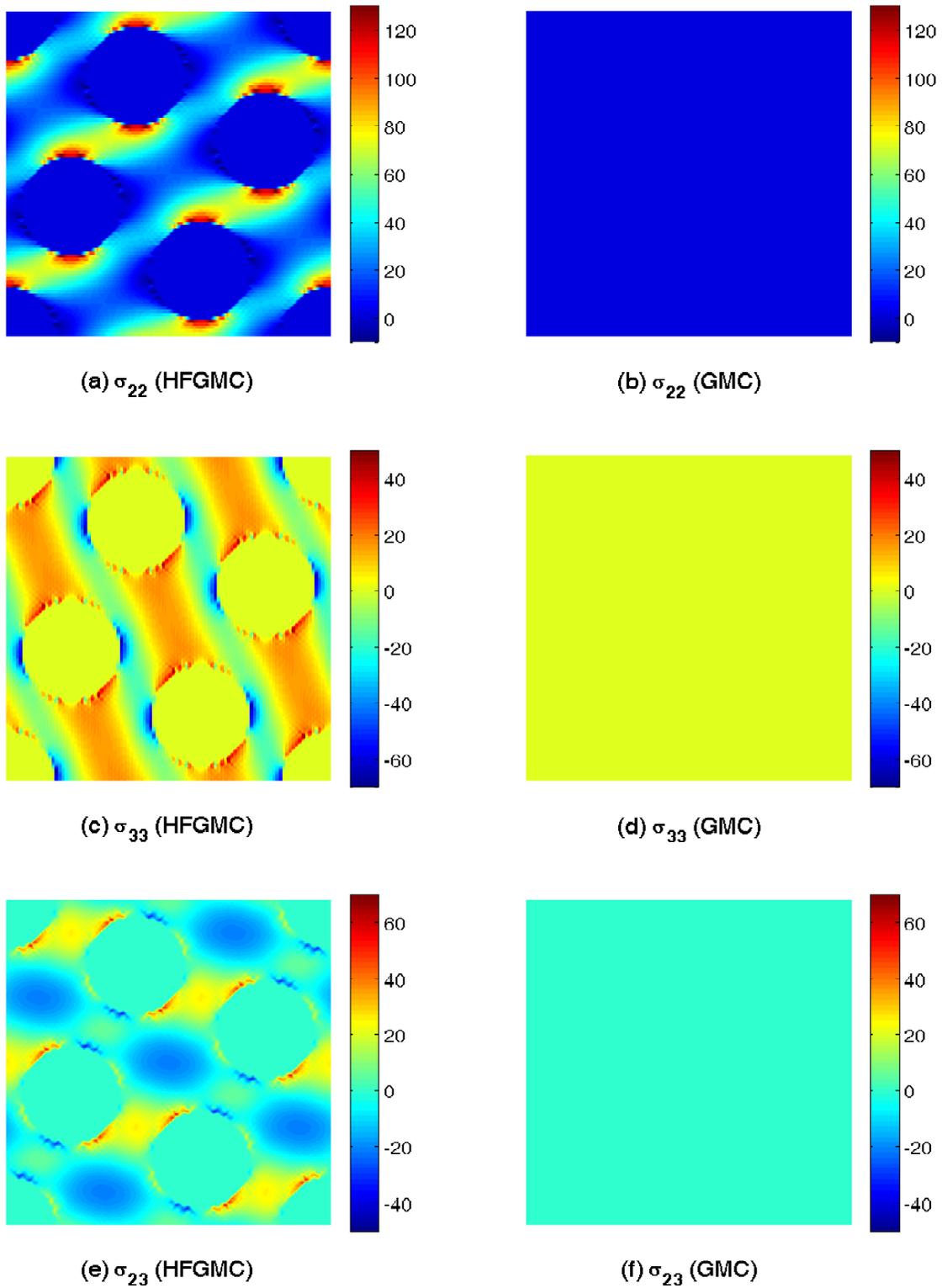
Figure 15. Comparison of the σ_{22}, σ_{33} and σ_{23} stress fields within the repeating unit cell of porous aluminum matrix rotated by $26.57°$ about the porosity axis and subjected to the average transverse normal strain $\bar{\varepsilon}_{22} = 0.1\%$. High-Fidelity (left column) vs original GMC (right column) predictions.
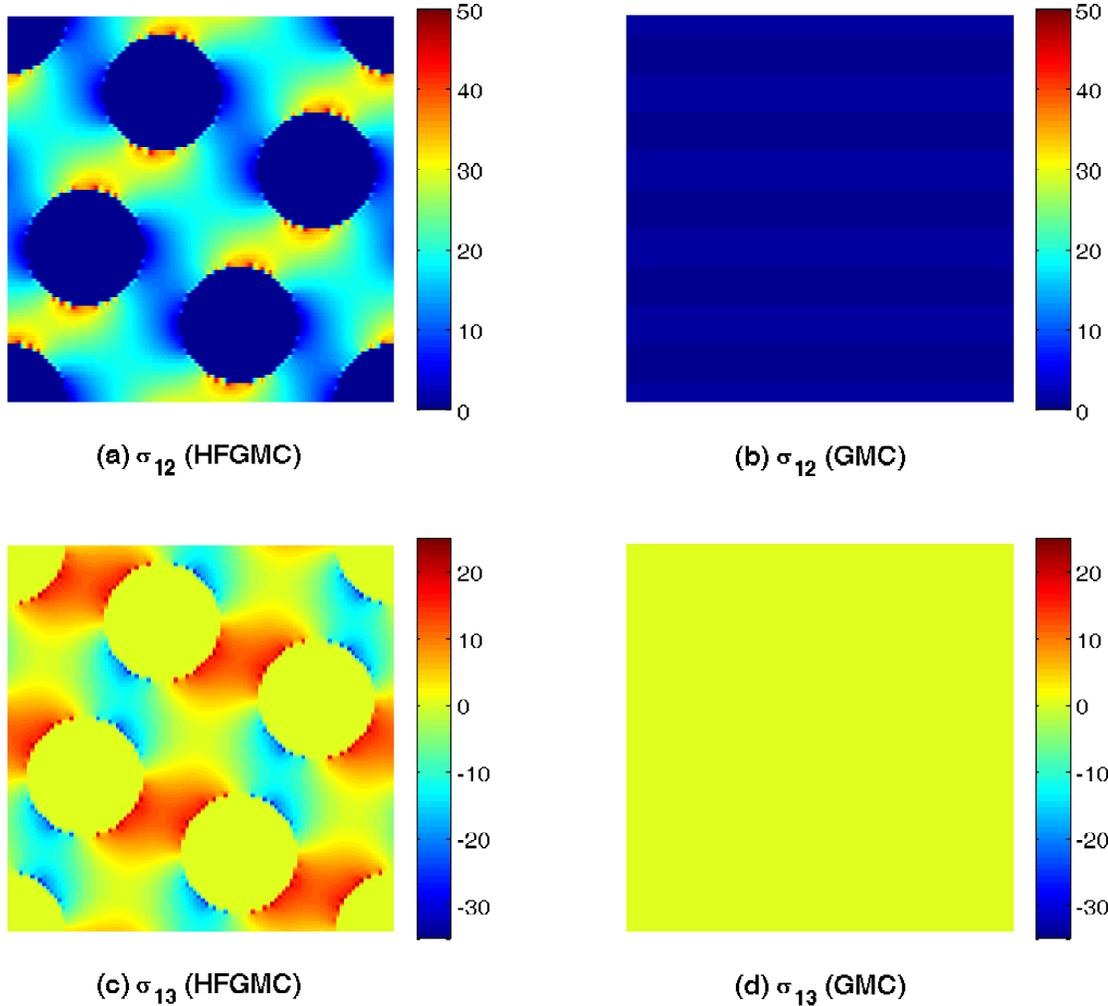
(a) σ_{23} (HFGMC)

(b) σ_{23} (GMC)

(c) σ_{22} (HFGMC)

(d) σ_{22} (GMC)
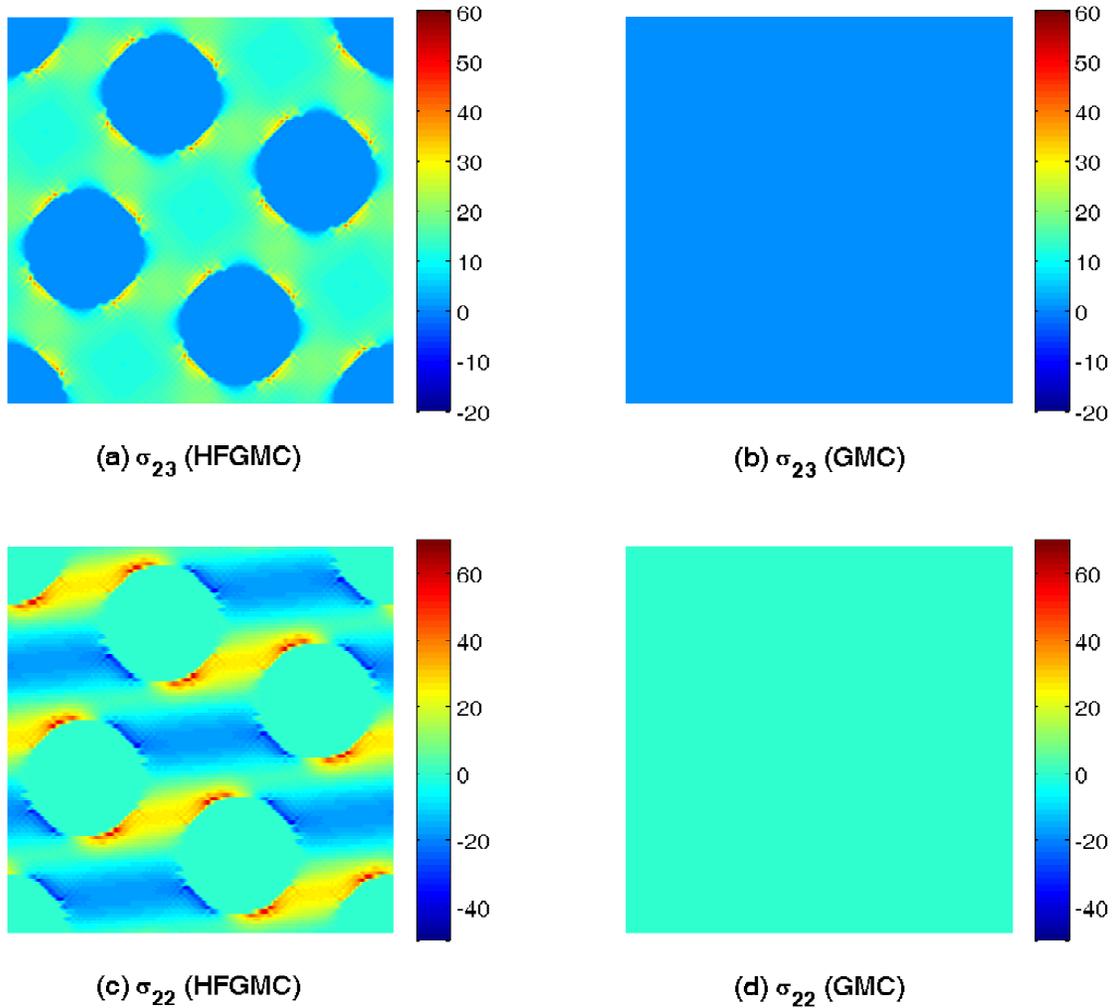
Figure 16. Comparison of the σ_{23} and σ_{22} stress fields within the repeating unit cell of porous aluminum matrix rotated by $26.57°$ about the porosity axis and subjected to the average transverse shear strain $\bar{\varepsilon}_{23} = 0.1\%$. High-Fidelity (left column) vs original GMC (right column) predictions.

direct result of the absence of shear coupling and lead to inaccurate microscale stress fields which cannot be used to predict local fiber or matrix failure caused by stress combinations other than the second stress deviator. As also shown for the porous aluminum case, these characteristic stress distributions produce highly inaccurate engineering moduli in the rotated coordinate system.

In order to mitigate the negative impact of the shear coupling absence, an alternative manner of determining the repeating unit cell response, and thus the engineering moduli, in the rotated coordinate system based on the GMC model can be chosen. First, the applied normal or shear strain in the rotated coordinate system is transformed to the principal coordinate system in order to determine the response in this reference frame. Then the resulting strains and stresses are transformed back to the rotated coordinate system in order to determine the elastic moduli. In

fact, this is the basis for the transformation equations given by Eq. (75), and should yield the same result as direct application of strains in the rotated coordinate system if the micromechanics model is self consistent. This is clearly the case for the HFGMC model. In the case of GMC, however, the observed characteristic stress patterns indicate that this is going to be only partially successful in the presence of very compliant inclusions. In particular, transforming the applied macroscopic strain to the principal material coordinate system will not negate the fact that the transverse shear response, and thus the transverse shear modulus, will be incorrectly predicted in the presence of porosities. In particular, the transverse shear modulus will be zero rendering the resulting macroscopic shear stress zero. Therefore, this contribution will be absent when transforming the stresses to the rotated coordinate system, thereby producing a result that will differ from the transformation equations by an amount that depends on the rotation angle or the magnitude of the absent transverse shear stress in the principal material coordinate system. However, the dramatic differences between GMC predictions and transformation equations observed in Fig. 11 and 12 for the porous aluminum case will be reduced because the contribution of the normal stresses in the principal material coordinate system will not be completely eliminated even in the presence of porosities. This method of calculating the engineering moduli in the rotated coordinate system is in fact equivalent to the use of transformation equations based on the moduli calculated by the GMC model in the principal material coordinate system. The different results obtained from the GMC-based calculations, which depend on whether the calculations are made in the rotated or unrotated coordinate system, point to a fundamental problem which limits this model's range of applicability. This limitation has clearly been overcome by the high-fidelity version which can be used to accurately model the response of a wide range of periodic materials with or without planes of material symmetry in different coordinate systems.

6   SUMMARY AND CONCLUSIONS

The reformulation of the High-Fidelity Generalized Method of Cells, based on a simplified volume discretization involving only subcells as the fundamental subvolumes together with the use of the local/global stiffness matrix approach, facilitates the analysis of repeating unit cells with complex microstructural details characteristic of realistic microstructures of multiphase materials. This is a direct result of the elimination of redundant continuity conditions present in the original formulation, which in turn produces substantial reduction in the size of the system of equations governing the response of the repeating unit cell. The reformulation also reveals the high-fidelity micromechanical analysis to be an approximate elasticity technique based on a direct volume averaging of the stress equilibrium equations and the imposition of the displacement and traction continuity conditions in a surface-averaged sense across the interfaces between adjacent subcells. This, in turn, simplifies the derivation of the volume-averaged equilibrium equations governing the individual subcell response as well as the derivation of the traction continuity conditions.

In the present investigation, the reformulation was employed to determine the elastic moduli of a square array of stiff fibers embedded in a substantially more compliant matrix, representative of a unidirectional glass/epoxy composite, under rotation about the fiber axis. A stiff matrix weakened by cylindrical porosities was also considered. The rotation about the fiber axis necessitates the analysis of repeating unit cells in the rotated coordinate system, representative of the same square array, which may contain many fibers, in contrast with the single fiber of the repeating unit cell in the principal material coordinate system. Such repeating unit cells typically do not possess planes of material symmetry, rendering them anisotropic in the rotated coordinate system. The elastic moduli of these unit cells can also be obtained from the standard transformation equations once the effective composite properties have been calculated in the principal material coordinate system. These transformation equations can therefore be employed to validate the predictive capability of a micromechanics model that admits periodic boundary conditions required in the absence of material planes of symmetry. The effective moduli predicted by the High-Fidelity Generalized Method of Cells based on the unit cells in the rotated coordinates systems have been shown herein to correlate extremely well with the transformation equations for both material systems considered. In contrast, the predictions of the original Generalized Method of Cells exhibited substantial departures from the transformation equations for the glass/epoxy system, which became unacceptably large for the porous aluminum. This is a direct result of the absence of shear coupling in the original method which produces erroneous results when normal/shear interaction dominates in the presence of porosities or inclusion phases that are substantially more compliant than the matrix phase. The high-fidelity version circumvents this problem, albeit at an increased computational cost which, however, is mitigated to a certain extent by the implemented reformulation. The microscale stress distributions generated by both models for different uniaxial loading situations provided additional insight supporting the predicted moduli results.

7 REFERENCES

1. Christensen, R. M. (1979). *Mechanics of Composite Materials*, John Wiley & Sons, New York.

2. Aboudi, J. (1991). *Mechanics of Composite Materials: A Unified Micromechanical Approach*, Elsevier, The Netherlands.

3. Nemat-Nasser, S. and Horii, M. (1993). *Micromechanics: Overall Properties of Heterogeneous Materials*, North-Holland, New York.

4. Kalamkarov, A. L. and Kolpakov, A. G. (1997). *Analysis, Design and Optimization of Composite Structures*, John Wiley & Sons, New York.

5. Markov, K. and Preziosi, L. (2000). Heterogeneous Media: Micromechanics Modeling Methods and Simulations, Birkhauser, Berlin.

6. Paley, M. and Aboudi, J. (1992). Micromechanical Analysis of Composites by the Generalized Method of Cells, *Mechanics of Materials*, **14**, 127-139.

7. Aboudi, J., (1996). Micromechanical Analysis of Composites by the Method of Cells - Update, *Applied Mechanics Reviews*, **49(**10), Part 2, S83-S91.

8. Pindera, M-J. and Bednarcyk, B. A. (1999). An Efficient Implementation of the GMC Micromechanics Model for Multi-Phased Materials with Complex Microstructures, *Composites: Part B (Engineering)*, **30**(1), 87-105.

9. Bednarcyk, B. A. and Pindera, M-J. (2000). Inelastic Response of a Woven Carbon/Copper Composite. Part 2: Micromechanics Model, *J. Composite Materials*, **34**(4), 299-331.

10. Bednarcyk, B. A. and Arnold, S. M. (2002). MAC/GMC 4.0 User's Manual: Theory (Vol. 1), Keywords Manual (Vol. 2), and Example Problem Manual (Vol. 3), *NASA TM 2002-212077.*

11. Hill, R. (1963). Elastic properties of Reinforced Solids: Some Theoretical Principles, *J. Mechanics and Physics of Solids*, **11**, 357-372.

12. Pindera, M-J. and Aboudi, J. (1988). Micromechanical Analysis of Yielding of Metal Matrix Composites, I*nt. J. Plasticity*, **4**, 195-214.

13. Pindera, M-J., Herakovich, C. T., Becker, W. and Aboudi, J. (1990). Nonlinear Response of Unidirectional Boron/Aluminum, J*. Composite Materials*, **24**(1), 2-21.

14. Arnold, S. M., Wilt, T.E., Saleeb, A.F., and Castelli, M.G. (1993). An Investigation of Macro and Micromechanical Approaches for a Model MMC System, *HITEMP Review 1993: CP 1911*7, 52.1-52.11

15. Iyer, S.K., Lissenden, C.J., and Arnold, S.M. (2000). Local and Overall Flow in Composites Predicted by Micromechanics, Composites: Part B, **31**, 327-343.

16. Arnold, S. M.; Pindera, M. J.; and Wilt, T.E. (1996). Influence of Fiber Architecture On The Inelastic Response of Metal Matrix Composites, *Int. J. Plasticity*, **12**(4), 507-545.

17. Bednarcyk, B. A., and Arnold, S. M. (2002). Transverse Tensile and Creep Modeling of Continuously Reinforced Titanium Composites with Local Debonding, *Int. J. Solids & Structures*, 39(7) 1987-2017.

18. Pahr, D. H. and Arnold, S. M. (2002). The Applicability of the Generalized Method of Cells for Analyzing Discontinuously Reinforced Composites. *Composites: Part B (Engineering)* **33**(2), 153-170.

19. Bednarcyk, B. and Arnold, S.M. (2003). Micromechanics Based Modeling of Woven Polymer Matrix Composites", *AIAA Journal*, 41(9), 1788-1796.

20. Orozco, C. (1997). Computational Aspects of Modeling Complex Microstructure Composites with GMC, *Composites: Part B*, **28**(1/2), 167-175.

21. Aboudi, J., Pindera, M-J., and Arnold, S.M. (2001). Linear Thermoelastic Higher-Order Theory for Periodic Multiphase Materials, *J. Appl. Mechanics*, **68**(5), 697-707.

22. Aboudi, J., Pindera, M-J., and Arnold, S.M. (2002). High-Fidelity Generalized Method of Cells for Inelastic Periodic Multiphase Materials, *NASA TM 2002-211469*.

23. Aboudi, J., Pindera, M-J, and Arnold, S. M. (2003). Higher-Order Theory for Periodic Multiphase Materials with Inelastic Phases, *Int. J. Plasticity*, **19**(6), 805-847.

24. Aboudi, J., Pindera, M-J., and Arnold, S. M. (1999). Higher-Order Theory for Functionally Graded Materials, *Composites: Part B (Engineering)*, **30**(8), 777-832.

25. Bednarcyk, B. A., Arnold, S. M., Aboudi, J., and Pindera, M-J. (2004). Local Field Effects in Titanium Matrix Composites Subject to Fiber-Matrix Debonding, *Int. J. Plasticity* (in press).

26. Pindera, M-J., Aboudi, J., and Arnold, S. M. (2003). Analysis of Locally Irregular Composites Using High-Fidelity Generalized Method of Cells, *AIAA Journal*, **41**(12), 2331-2340.

27. Bufler, H. (1971). Theory of Elasticity of a Multilayered Medium, *J. Elasticity*, **1**, 125-143.

28. Pindera, M-J. (1991). Local/Global Stiffness Matrix Formulation for Composite Materials and Structures, *Composites Engineering*, **1**(2), 69-83.

29. Bansal, Y. and Pindera, M-J. (2003). Efficient Reformulation of the Thermoelastic Higher-Order Theory for FGMs, *J. Thermal Stresses*, **26**(11/12), 1055-1092. See also: *NASA Contractor Report 2002-211909*, November 2002.

30. Lekhnitskii, S. G. (1981). *Theory of Elasticity of an Anisotropic Body*, Mir Publishers, Moscow.

8 APPENDIX

8.1 Local Stiffness Matrix Elements

Explicit expressions for the non-zero elements of the local stiffness matrix for the (β, γ) subcell, given in terms of the subcell's geometric and mechanical properties, are listed below for loading by normal and shear tractions in the $y_2 - y_3$ plane.

$$K_{11}^{(\beta,\gamma)} = K_{22}^{(\beta,\gamma)} = \frac{C_{22}^{(\beta,\gamma)}}{h_\beta}\left(4 - 3\frac{C_{22}^{(\beta,\gamma)}}{\bar{C}_{22}^{(\beta,\gamma)}}\right)$$

$$K_{12}^{(\beta,\gamma)} = K_{21}^{(\beta,\gamma)} = \frac{C_{22}^{(\beta,\gamma)}}{h_\beta}\left(2 - 3\frac{C_{22}^{(\beta,\gamma)}}{\bar{C}_{22}^{(\beta,\gamma)}}\right)$$

$$K_{15}^{(\beta,\gamma)} = K_{16}^{(\beta,\gamma)} = K_{25}^{(\beta,\gamma)} = K_{26}^{(\beta,\gamma)} = -\frac{3C_{22}^{(\beta,\gamma)}C_{44}^{(\beta,\gamma)}h_\beta}{\bar{C}_{22}^{(\beta,\gamma)}l_\gamma^2}$$

$$K_{17}^{(\beta,\gamma)} = -K_{18}^{(\beta,\gamma)} = -K_{27}^{(\beta,\gamma)} = K_{28}^{(\beta,\gamma)} = \frac{C_{23}^{(\beta,\gamma)}}{l_\gamma}$$

$$K_{33}^{(\beta,\gamma)} = K_{44}^{(\beta,\gamma)} = \frac{C_{44}^{(\beta,\gamma)}}{h_\beta}\left(4 - 3\frac{l_\gamma^2 C_{44}^{(\beta,\gamma)}}{h_\beta^2 \bar{C}_{33}^{(\beta,\gamma)}}\right),$$

$$K_{34}^{(\beta,\gamma)} = K_{43}^{(\beta,\gamma)} = \frac{C_{44}^{(\beta,\gamma)}}{h_\beta}\left(2 - 3\frac{l_\gamma^2 C_{44}^{(\beta,\gamma)}}{h_\beta^2 \bar{C}_{33}^{(\beta,\gamma)}}\right)$$

$$K_{35}^{(\beta,\gamma)} = -K_{36}^{(\beta,\gamma)} = -K_{45}^{(\beta,\gamma)} = K_{46}^{(\beta,\gamma)} = \frac{C_{44}^{(\beta,\gamma)}}{l_\gamma}$$

$$K_{37}^{(\beta,\gamma)} = K_{38}^{(\beta,\gamma)} = K_{47}^{(\beta,\gamma)} = K_{48}^{(\beta,\gamma)} = -\frac{3C_{33}^{(\beta,\gamma)}C_{44}^{(\beta,\gamma)}}{h_\beta \bar{C}_{33}^{(\beta,\gamma)}}$$

$$K_{51}^{(\beta,\gamma)} = K_{52}^{(\beta,\gamma)} = K_{61}^{(\beta,\gamma)} = K_{62}^{(\beta,\gamma)} = -\frac{3C_{22}^{(\beta,\gamma)}C_{44}^{(\beta,\gamma)}}{l_\gamma \bar{C}_{22}^{(\beta,\gamma)}}$$

$$K_{53}^{(\beta,\gamma)} = -K_{54}^{(\beta,\gamma)} = -K_{63}^{(\beta,\gamma)} = K_{64}^{(\beta,\gamma)} = \frac{C_{44}^{(\beta,\gamma)}}{h_\beta}$$

$$K_{55}^{(\beta,\gamma)} = K_{66}^{(\beta,\gamma)} = \frac{C_{44}^{(\beta,\gamma)}}{l_\gamma}\left(4 - 3\frac{h_\beta^2 C_{44}^{(\beta,\gamma)}}{l_\gamma^2 \bar{C}_{22}^{(\beta,\gamma)}}\right)$$

$$K_{56}^{(\beta,\gamma)} = K_{65}^{(\beta,\gamma)} = \frac{C_{44}^{(\beta,\gamma)}}{l_\gamma}\left(2 - 3\frac{h_\beta^2 C_{44}^{(\beta,\gamma)}}{l_\gamma^2 \bar{C}_{22}^{(\beta,\gamma)}}\right)$$

$$K_{71}^{(\beta,\gamma)} = -K_{72}^{(\beta,\gamma)} = -K_{81}^{(\beta,\gamma)} = K_{82}^{(\beta,\gamma)} = \frac{C_{23}^{(\beta,\gamma)}}{h_\beta}$$

$$K_{73}^{(\beta,\gamma)} = K_{74}^{(\beta,\gamma)} = K_{83}^{(\beta,\gamma)} = K_{84}^{(\beta,\gamma)} = -\frac{3C_{33}^{(\beta,\gamma)}C_{44}^{(\beta,\gamma)}l_\gamma}{\bar{C}_{33}^{(\beta,\gamma)}h_\beta^2}$$

$$K_{77}^{(\beta,\gamma)} = K_{88}^{(\beta,\gamma)} = \frac{C_{33}^{(\beta,\gamma)}}{l_\gamma}\left(4 - 3\frac{C_{33}^{(\beta,\gamma)}}{\bar{C}_{33}^{(\beta,\gamma)}}\right)$$

$$K_{78}^{(\beta,\gamma)} = K_{87}^{(\beta,\gamma)} = \frac{C_{33}^{(\beta,\gamma)}}{l_\gamma}\left(2 - 3\frac{C_{33}^{(\beta,\gamma)}}{\bar{C}_{33}^{(\beta,\gamma)}}\right)$$

The elements of the local stiffness matrix for loading by shear tractions in the $y_1 - y_2$ and $y_1 - y_3$ planes are given below.

$$L_{11}^{(\beta,\gamma)} = L_{22}^{(\beta,\gamma)} = \frac{C_{66}^{(\beta,\gamma)}}{h_\beta}\left(4 - 3\frac{C_{66}^{(\beta,\gamma)}}{\bar{C}_{11}^{(\beta,\gamma)}}\right)$$

$$L_{12}^{(\beta,\gamma)} = L_{21}^{(\beta,\gamma)} = \frac{C_{66}^{(\beta,\gamma)}}{h_\beta}\left(2 - 3\frac{C_{66}^{(\beta,\gamma)}}{\bar{C}_{11}^{(\beta,\gamma)}}\right)$$

$$L_{13}^{(\beta,\gamma)} = L_{14}^{(\beta,\gamma)} = L_{23}^{(\beta,\gamma)} = L_{24}^{(\beta,\gamma)} = -\frac{3C_{55}C_{66}^{(\beta,\gamma)}h_\beta}{\bar{C}_{11}^{(\beta,\gamma)}l_\gamma^2}$$

$$L_{31}^{(\beta,\gamma)} = L_{32}^{(\beta,\gamma)} = L_{41}^{(\beta,\gamma)} = L_{42}^{(\beta,\gamma)} = -\frac{3C_{55}C_{66}^{(\beta,\gamma)}}{\bar{C}_{11}^{(\beta,\gamma)}l}$$

$$L_{33}^{(\beta,\gamma)} = L_{44}^{(\beta,\gamma)} = \frac{C_{55}^{(\beta,\gamma)}}{l_\gamma}\left(4 - 3\frac{h_\beta^2 C_{55}^{(\beta,\gamma)}}{l_\gamma^2 \bar{C}_{11}^{(\beta,\gamma)}}\right)$$

$$L_{34}^{(\beta,\gamma)} = L_{43}^{(\beta,\gamma)} = \frac{C_{55}^{(\beta,\gamma)}}{l_\gamma}\left(2 - 3\frac{h_\beta^2 C_{55}^{(\beta,\gamma)}}{l_\gamma^2 \bar{C}_{11}^{(\beta,\gamma)}}\right)$$

8.2 Numerical Results

8.2.1 Glass/Epoxy Composite: HFGMC Predictions

```
ANGLE = 0 degrees


CELL EFFECTIVE STIFFNESS

    2.9214E+04    4.2656E+03    4.2656E+03   -4.6827E-11    0.0000E+00    0.0000E+00
    4.2656E+03    9.5857E+03    4.1918E+03   -9.7567E-11    0.0000E+00    0.0000E+00
    4.2656E+03    4.1918E+03    9.5857E+03   -9.6209E-11    0.0000E+00    0.0000E+00
   -4.6064E-11   -6.7785E-11   -1.2299E-10    2.0856E+03    0.0000E+00    0.0000E+00
    0.0000E+00    0.0000E+00    0.0000E+00    0.0000E+00    2.5070E+03   -4.4269E-11
    0.0000E+00    0.0000E+00    0.0000E+00    0.0000E+00   -4.3698E-11    2.5070E+03

EFFECTIVE MODULI

E11 =    2.6573E+04
E22 =    7.5417E+03
E33 =    7.5417E+03
G23 =    2.0856E+03
G13 =    2.5070E+03
G12 =    2.5070E+03
NU23 =   3.9820E-01
NU13 =   3.0961E-01
NU12 =   3.0961E-01
```

```
ANGLE = 14.04 degrees


CELL EFFECTIVE STIFFNESS

   2.9268E+04    4.2738E+03    4.2738E+03    8.9032E-12    0.0000E+00    0.0000E+00
   4.2738E+03    9.5079E+03    4.3033E+03   -2.5483E+02    0.0000E+00    0.0000E+00
   4.2738E+03    4.3033E+03    9.5079E+03    2.5483E+02    0.0000E+00    0.0000E+00
   1.0230E-11   -2.5483E+02    2.5483E+02    2.2148E+03    0.0000E+00    0.0000E+00
   0.0000E+00    0.0000E+00    0.0000E+00    0.0000E+00    2.5218E+03    1.9721E-11
   0.0000E+00    0.0000E+00    0.0000E+00    0.0000E+00    1.9821E-11    2.5218E+03

EFFECTIVE MODULI

E11 =    2.6623E+04
E22 =    7.3013E+03
E33 =    7.3013E+03
G23 =    2.1899E+03
G13 =    2.5218E+03
G12 =    2.5218E+03
NU23 =   4.1883E-01
NU13 =   3.0944E-01
NU12 =   3.0944E-01


ANGLE = 26.57 degrees


CELL EFFECTIVE STIFFNESS

   2.9023E+04    4.2544E+03    4.2544E+03    5.1096E-12    0.0000E+00    0.0000E+00
   4.2544E+03    9.1527E+03    4.5782E+03   -2.8695E+02    0.0000E+00    0.0000E+00
   4.2544E+03    4.5782E+03    9.1527E+03    2.8695E+02    0.0000E+00    0.0000E+00
   7.6872E-12   -2.8695E+02    2.8695E+02    2.4771E+03    0.0000E+00    0.0000E+00
   0.0000E+00    0.0000E+00    0.0000E+00    0.0000E+00    2.5013E+03    5.9124E-11
   0.0000E+00    0.0000E+00    0.0000E+00    0.0000E+00    5.8265E-11    2.5013E+03

EFFECTIVE MODULI

E11 =    2.6387E+04
E22 =    6.6240E+03
E33 =    6.6240E+03
G23 =    2.4411E+03
G13 =    2.5013E+03
G12 =    2.5013E+03
NU23 =   4.6938E-01
NU13 =   3.0984E-01
NU12 =   3.0984E-01


ANGLE = 36.87 degrees


CELL EFFECTIVE STIFFNESS

   2.9514E+04    4.2947E+03    4.2947E+03   -5.4990E-12    0.0000E+00    0.0000E+00
   4.2947E+03    9.1142E+03    4.7835E+03   -1.7227E+02    0.0000E+00    0.0000E+00
   4.2947E+03    4.7835E+03    9.1142E+03    1.7227E+02    0.0000E+00    0.0000E+00
  -5.5649E-12   -1.7227E+02    1.7227E+02    2.6792E+03    0.0000E+00    0.0000E+00
   0.0000E+00    0.0000E+00    0.0000E+00    0.0000E+00    2.5480E+03    6.7261E-02
   0.0000E+00    0.0000E+00    0.0000E+00    0.0000E+00    7.7051E-12    2.5480E+03
```

```
EFFECTIVE MODULI

E11 =    2.6860E+04
E22 =    6.4275E+03
E33 =    6.4275E+03
G23 =    2.6655E+03
G13 =    2.5480E+03
G12 =    2.5480E+03
NU23 =   4.9181E-01
NU13 =   3.0902E-01
NU12 =   3.0902E-01


ANGLE = 45 degrees


CELL EFFECTIVE STIFFNESS

   2.9462E+04    4.2848E+03    4.2848E+03   -3.1417E-11    0.0000E+00    0.0000E+00
   4.2848E+03    9.0188E+03    4.8382E+03   -3.5367E-11    0.0000E+00    0.0000E+00
   4.2848E+03    4.8382E+03    9.0188E+03   -9.4672E-11    0.0000E+00    0.0000E+00
  -2.6528E-11   -1.9263E-11   -9.1672E-11    2.7397E+03    0.0000E+00    0.0000E+00
   0.0000E+00    0.0000E+00    0.0000E+00    0.0000E+00    2.5268E+03    3.4886E-11
   0.0000E+00    0.0000E+00    0.0000E+00    0.0000E+00    3.4856E-11    2.5268E+03

EFFECTIVE MODULI

E11 =    2.6812E+04
E22 =    6.2794E+03
E33 =    6.2794E+03
G23 =    2.7397E+03
G13 =    2.5268E+03
G12 =    2.5268E+03
NU23 =   5.0206E-01
NU13 =   3.0922E-01
NU12 =   3.0922E-01
```

8.2.2 Glass/Epoxy Composite: GMC Predictions

```
ANGLE = 0 degrees


CELL EFFECTIVE STIFFNESS

   0.2918E+05    0.4186E+04    0.4186E+04    0.0000E+00    0.0000E+00    0.0000E+00
   0.4186E+04    0.9326E+04    0.4124E+04    0.0000E+00    0.0000E+00    0.0000E+00
   0.4186E+04    0.4124E+04    0.9326E+04    0.0000E+00    0.0000E+00    0.0000E+00
   0.0000E+00    0.0000E+00    0.0000E+00    0.1937E+04    0.0000E+00    0.0000E+00
   0.0000E+00    0.0000E+00    0.0000E+00    0.0000E+00    0.2266E+04    0.0000E+00
   0.0000E+00    0.0000E+00    0.0000E+00    0.0000E+00    0.0000E+00    0.2266E+04

EFFECTIVE MODULI

 E11S= 0.2657E+05
 N12S= 0.3113E+00
 E22S= 0.7303E+04
 N23S= 0.4037E+00
 E33S= 0.7303E+04
 G23S= 0.1937E+04
 G13S= 0.2266E+04
 G12S= 0.2266E+04
```

ANGLE = 14.04 degrees

CELL EFFECTIVE STIFFNESS

```
    0.2914E+05   0.4015E+04   0.4015E+04   0.0000E+00   0.0000E+00   0.0000E+00
    0.4015E+04   0.8318E+04   0.4422E+04   0.0000E+00   0.0000E+00   0.0000E+00
    0.4015E+04   0.4422E+04   0.8318E+04   0.0000E+00   0.0000E+00   0.0000E+00
    0.0000E+00   0.0000E+00   0.0000E+00   0.1939E+04   0.0000E+00   0.0000E+00
    0.0000E+00   0.0000E+00   0.0000E+00   0.0000E+00   0.1945E+04   0.0000E+00
    0.0000E+00   0.0000E+00   0.0000E+00   0.0000E+00   0.0000E+00   0.1945E+04
```

EFFECTIVE MODULI

```
  E11S= 0.2661E+05
  N12S= 0.3151E+00
  E22S= 0.5838E+04
  N23S= 0.4982E+00
  E33S= 0.5838E+04
  G23S= 0.1939E+04
  G13S= 0.1945E+04
  G12S= 0.1945E+04
```


ANGLE = 26.57 degrees

CELL EFFECTIVE STIFFNESS

```
    0.2890E+05   0.4005E+04   0.4005E+04   0.0000E+00   0.0000E+00   0.0000E+00
    0.4005E+04   0.8298E+04   0.4400E+04   0.0000E+00   0.0000E+00   0.0000E+00
    0.4005E+04   0.4400E+04   0.8298E+04   0.0000E+00   0.0000E+00   0.0000E+00
    0.0000E+00   0.0000E+00   0.0000E+00   0.1929E+04   0.0000E+00   0.0000E+00
    0.0000E+00   0.0000E+00   0.0000E+00   0.0000E+00   0.1942E+04   0.0000E+00
    0.0000E+00   0.0000E+00   0.0000E+00   0.0000E+00   0.0000E+00   0.1942E+04
```

EFFECTIVE MODULI

```
  E11S= 0.2638E+05
  N12S= 0.3154E+00
  E22S= 0.5834E+04
  N23S= 0.4966E+00
  E33S= 0.5834E+04
  G23S= 0.1929E+04
  G13S= 0.1942E+04
  G12S= 0.1942E+04
```


ANGLE = 36.87 degrees

CELL EFFECTIVE STIFFNESS

```
    0.2938E+05   0.4026E+04   0.4026E+04   0.0000E+00   0.0000E+00   0.0000E+00
    0.4026E+04   0.8342E+04   0.4443E+04   0.0000E+00   0.0000E+00   0.0000E+00
    0.4026E+04   0.4443E+04   0.8342E+04   0.0000E+00   0.0000E+00   0.0000E+00
    0.0000E+00   0.0000E+00   0.0000E+00   0.1949E+04   0.0000E+00   0.0000E+00
    0.0000E+00   0.0000E+00   0.0000E+00   0.0000E+00   0.1949E+04   0.0000E+00
    0.0000E+00   0.0000E+00   0.0000E+00   0.0000E+00   0.0000E+00   0.1949E+04
```

EFFECTIVE MODULI

```
E11S= 0.2685E+05
N12S= 0.3149E+00
E22S= 0.5846E+04
N23S= 0.4996E+00
E33S= 0.5846E+04
G23S= 0.1949E+04
G13S= 0.1949E+04
G12S= 0.1949E+04
```

ANGLE = 45 degrees

CELL EFFECTIVE STIFFNESS

```
0.2936E+05  0.4064E+04  0.4064E+04  0.0000E+00  0.0000E+00  0.0000E+00
0.4064E+04  0.8511E+04  0.4430E+04  0.0000E+00  0.0000E+00  0.0000E+00
0.4064E+04  0.4430E+04  0.8511E+04  0.0000E+00  0.0000E+00  0.0000E+00
0.0000E+00  0.0000E+00  0.0000E+00  0.1947E+04  0.0000E+00  0.0000E+00
0.0000E+00  0.0000E+00  0.0000E+00  0.0000E+00  0.2008E+04  0.0000E+00
0.0000E+00  0.0000E+00  0.0000E+00  0.0000E+00  0.0000E+00  0.2008E+04
```

EFFECTIVE MODULI

```
E11S= 0.2680E+05
N12S= 0.3140E+00
E22S= 0.6066E+04
N23S= 0.4866E+00
E33S= 0.6066E+04
G23S= 0.1947E+04
G13S= 0.2008E+04
G12S= 0.2008E+04
```

8.2.3   Aluminum with Cylindrical Porosities: HFGMC Predictions

ANGLE = 0 degrees

CELL EFFECTIVE STIFFNESS

```
 5.7040E+04   1.6777E+04   1.6777E+04  -2.4291E-11   0.0000E+00   0.0000E+00
 1.6777E+04   3.8902E+04   1.1938E+04  -1.9329E-11   0.0000E+00   0.0000E+00
 1.6777E+04   1.1938E+04   3.8902E+04  -5.3848E-11   0.0000E+00   0.0000E+00
-1.0418E-11  -1.6283E-11  -2.1946E-11   6.9500E+03   0.0000E+00   0.0000E+00
 0.0000E+00   0.0000E+00   0.0000E+00   0.0000E+00   1.2819E+04   7.5322E-11
 0.0000E+00   0.0000E+00   0.0000E+00   0.0000E+00   7.5422E-11   1.2819E+04
```

EFFECTIVE MODULI

```
E11 =    4.5967E+04
E22 =    3.2523E+04
E33 =    3.2523E+04
G23 =    6.9500E+03
G13 =    1.2819E+04
G12 =    1.2819E+04
NU23 =   2.0618E-01
NU13 =   3.3000E-01
NU12 =   3.3000E-01
```

```
ANGLE = 14.04 degrees


CELL EFFECTIVE STIFFNESS

    5.6619E+04    1.6219E+04    1.6219E+04    3.4135E-12    0.0000E+00    0.0000E+00
    1.6219E+04    3.6558E+04    1.2591E+04   -2.6832E+03    0.0000E+00    0.0000E+00
    1.6219E+04    1.2591E+04    3.6558E+04    2.6832E+03    0.0000E+00    0.0000E+00
    1.7596E-12   -2.6832E+03    2.6832E+03    7.7323E+03    0.0000E+00    0.0000E+00
    0.0000E+00    0.0000E+00    0.0000E+00    0.0000E+00    1.2625E+04   -1.1416E-11
    0.0000E+00    0.0000E+00    0.0000E+00    0.0000E+00   -1.1035E-11    1.2625E+04

EFFECTIVE MODULI

E11 =     4.5914E+04
E22 =     2.8437E+04
E33 =     2.8437E+04
G23 =     7.1315E+03
G13 =     1.2625E+04
G12 =     1.2625E+04
NU23 =    2.8651E-01
NU13 =    3.3000E-01
NU12 =    3.3000E-01


ANGLE = 26.57 degrees


CELL EFFECTIVE STIFFNESS

    5.7057E+04    1.6510E+04    1.6510E+04   -1.6233E-11    0.0000E+00    0.0000E+00
    1.6510E+04    3.4149E+04    1.5880E+04   -3.1257E+03    0.0000E+00    0.0000E+00
    1.6510E+04    1.5880E+04    3.4149E+04    3.1257E+03    0.0000E+00    0.0000E+00
   -2.1006E-11   -3.1257E+03    3.1257E+03    1.1053E+04    0.0000E+00    0.0000E+00
    0.0000E+00    0.0000E+00    0.0000E+00    0.0000E+00    1.2762E+04   -7.1498E-13
    0.0000E+00    0.0000E+00    0.0000E+00    0.0000E+00   -8.7295E-13    1.2762E+04

EFFECTIVE MODULI

E11 =     4.6161E+04
E22 =     2.3445E+04
E33 =     2.3445E+04
G23 =     9.9834E+03
G13 =     1.2762E+04
G12 =     1.2762E+04
NU23 =    4.2077E-01
NU13 =    3.3000E-01
NU12 =    3.3000E-01


ANGLE = 36.87 degrees


CELL EFFECTIVE STIFFNESS

    5.6009E+04    1.5668E+04    1.5668E+04   -6.1709E-12    0.0000E+00    0.0000E+00
    1.5668E+04    3.0781E+04    1.6698E+04   -1.8320E+03    0.0000E+00    0.0000E+00
    1.5668E+04    1.6698E+04    3.0781E+04    1.8320E+03    0.0000E+00    0.0000E+00
   -4.6593E-12   -1.8320E+03    1.8320E+03    1.2302E+04    0.0000E+00    0.0000E+00
    0.0000E+00    0.0000E+00    0.0000E+00    0.0000E+00    1.2408E+04   -1.3313E-12
    0.0000E+00    0.0000E+00    0.0000E+00    0.0000E+00   -1.0340E-12    1.2408E+04

EFFECTIVE MODULI
```

```
E11 =     4.5668E+04
E22 =     2.0060E+04
E33 =     2.0060E+04
G23 =     1.1825E+04
G13 =     1.2408E+04
G12 =     1.2408E+04
NU23 =    4.8183E-01
NU13 =    3.3000E-01
NU12 =    3.3000E-01


ANGLE = 45 degrees


CELL EFFECTIVE STIFFNESS

    5.6602E+04    1.6492E+04    1.6492E+04   -6.5033E-12    0.0000E+00    0.0000E+00
    1.6492E+04    3.1628E+04    1.8348E+04    2.3342E-11    0.0000E+00    0.0000E+00
    1.6492E+04    1.8348E+04    3.1628E+04   -4.2766E-11    0.0000E+00    0.0000E+00
   -8.2076E-12    4.6414E-12   -2.5772E-11    1.3374E+04    0.0000E+00    0.0000E+00
    0.0000E+00    0.0000E+00    0.0000E+00    0.0000E+00    1.2681E+04    3.5532E-12
    0.0000E+00    0.0000E+00    0.0000E+00    0.0000E+00    4.1566E-12    1.2681E+04

EFFECTIVE MODULI

E11 =     4.5717E+04
E22 =     1.9985E+04
E33 =     1.9985E+04
G23 =     1.3374E+04
G13 =     1.2681E+04
G12 =     1.2681E+04
NU23 =    5.0491E-01
NU13 =    3.3000E-01
NU12 =    3.3000E-01
```

8.2.4   Aluminum with Cylindrical Porosities: GMC Predictions

```
ANGLE = 0 degrees

CELL EFFECTIVE STIFFNESS

    0.5359E+05    0.1156E+05    0.1156E+05    0.0000E+00    0.0000E+00    0.0000E+00
    0.1156E+05    0.2925E+05    0.5778E+04    0.0000E+00    0.0000E+00    0.0000E+00
    0.1156E+05    0.5778E+04    0.2925E+05    0.0000E+00    0.0000E+00    0.0000E+00
    0.0000E+00    0.0000E+00    0.0000E+00    0.7448E+03    0.0000E+00    0.0000E+00
    0.0000E+00    0.0000E+00    0.0000E+00    0.0000E+00    0.9319E+04    0.0000E+00
    0.0000E+00    0.0000E+00    0.0000E+00    0.0000E+00    0.0000E+00    0.9319E+04

EFFECTIVE MODULI

  E11S= 0.4597E+05
  N12S= 0.3300E+00
  E22S= 0.2635E+05
  N23S= 0.1228E+00
  E33S= 0.2635E+05
  G23S= 0.7448E+03
  G13S= 0.9319E+04
  G12S= 0.9319E+04
```

```
ANGLE = 14.04 degrees

CELL EFFECTIVE STIFFNESS

    0.4687E+05  0.1452E+04  0.1452E+04  0.0000E+00  0.0000E+00  0.0000E+00
    0.1452E+04  0.2958E+04  0.1442E+04  0.0000E+00  0.0000E+00  0.0000E+00
    0.1452E+04  0.1442E+04  0.2958E+04  0.0000E+00  0.0000E+00  0.0000E+00
    0.0000E+00  0.0000E+00  0.0000E+00  0.7432E+03  0.0000E+00  0.0000E+00
    0.0000E+00  0.0000E+00  0.0000E+00  0.0000E+00  0.7528E+03  0.0000E+00
    0.0000E+00  0.0000E+00  0.0000E+00  0.0000E+00  0.0000E+00  0.7528E+03

EFFECTIVE MODULI

  E11S= 0.4591E+05

  N12S= 0.3300E+00
  E22S= 0.2243E+04
  N23S= 0.4796E+00
  E33S= 0.2243E+04
  G23S= 0.7432E+03
  G13S= 0.7528E+03
  G12S= 0.7528E+03


ANGLE = 26.57 degrees

CELL EFFECTIVE STIFFNESS

    0.4713E+05  0.1475E+04  0.1475E+04  0.0000E+00  0.0000E+00  0.0000E+00
    0.1475E+04  0.3016E+04  0.1454E+04  0.0000E+00  0.0000E+00  0.0000E+00
    0.1475E+04  0.1454E+04  0.3016E+04  0.0000E+00  0.0000E+00  0.0000E+00
    0.0000E+00  0.0000E+00  0.0000E+00  0.7507E+03  0.0000E+00  0.0000E+00
    0.0000E+00  0.0000E+00  0.0000E+00  0.0000E+00  0.7699E+03  0.0000E+00
    0.0000E+00  0.0000E+00  0.0000E+00  0.0000E+00  0.0000E+00  0.7699E+03

EFFECTIVE MODULI

  E11S= 0.4616E+05
  N12S= 0.3300E+00
  E22S= 0.2303E+04
  N23S= 0.4740E+00
  E33S= 0.2303E+04
  G23S= 0.7507E+03
  G13S= 0.7699E+03
  G12S= 0.7699E+03


ANGLE = 36.87 degrees

CELL EFFECTIVE STIFFNESS

    0.4661E+05  0.1429E+04  0.1429E+04  0.0000E+00  0.0000E+00  0.0000E+00
    0.1429E+04  0.2901E+04  0.1429E+04  0.0000E+00  0.0000E+00  0.0000E+00
    0.1429E+04  0.1429E+04  0.2901E+04  0.0000E+00  0.0000E+00  0.0000E+00
    0.0000E+00  0.0000E+00  0.0000E+00  0.7359E+03  0.0000E+00  0.0000E+00
    0.0000E+00  0.0000E+00  0.0000E+00  0.0000E+00  0.7361E+03  0.0000E+00
    0.0000E+00  0.0000E+00  0.0000E+00  0.0000E+00  0.0000E+00  0.7361E+03

EFFECTIVE MODULI

  E11S= 0.4567E+05
```

```
N12S= 0.3300E+00
E22S= 0.2186E+04
N23S= 0.4847E+00
E33S= 0.2186E+04
G23S= 0.7359E+03
G13S= 0.7361E+03
G12S= 0.7361E+03


ANGLE = 45 degrees

CELL EFFECTIVE STIFFNESS

   0.4740E+05  0.2557E+04  0.2557E+04  0.0000E+00  0.0000E+00  0.0000E+00
   0.2557E+04  0.6279E+04  0.1469E+04  0.0000E+00  0.0000E+00  0.0000E+00
   0.2557E+04  0.1469E+04  0.6279E+04  0.0000E+00  0.0000E+00  0.0000E+00
   0.0000E+00  0.0000E+00  0.0000E+00  0.7374E+03  0.0000E+00  0.0000E+00
   0.0000E+00  0.0000E+00  0.0000E+00  0.0000E+00  0.1864E+04  0.0000E+00
   0.0000E+00  0.0000E+00  0.0000E+00  0.0000E+00  0.0000E+00  0.1864E+04

EFFECTIVE MODULI

  E11S=   0.4572E+05
  N12S=   0.3300E+00
  E22S=   0.5852E+04
  N23S=   0.2168E+00
  E33S=   0.5852E+04
  G23S=   0.7374E+03
  G13S=   0.1864E+04
  G12S=   0.1864E+04
```

REPORT DOCUMENTATION PAGE

Public reporting burden for this collection of information is estimated to average 1 hour per response, including the time for reviewing instructions, searching existing data sources, gathering and maintaining the data needed, and completing and reviewing the collection of information. Send comments regarding this burden estimate or any other aspect of this collection of information, including suggestions for reducing this burden, to Washington Headquarters Services, Directorate for Information Operations and Reports, 1215 Jefferson Davis Highway, Suite 1204, Arlington, VA 22202-4302, and to the Office of Management and Budget, Paperwork Reduction Project (0704-0188), Washington, DC 20503.

1. AGENCY USE ONLY (Leave blank)	2. REPORT DATE	3. REPORT TYPE AND DATES COVERED
	April 2004	Final Contractor Report

4. TITLE AND SUBTITLE

Testing the Predictive Capability of the High-Fidelity Generalized Method of Cells Using an Efficient Reformulation

5. FUNDING NUMBERS

WBS–22–714–70–11
NAG3–2524

6. AUTHOR(S)

Yogesh Bansal and Marek-Jerzy Pindera

7. PERFORMING ORGANIZATION NAME(S) AND ADDRESS(ES)

University of Virginia
0 Mccormick Road
Charlottesville, Virginia 22904

8. PERFORMING ORGANIZATION REPORT NUMBER

E–14480

9. SPONSORING/MONITORING AGENCY NAME(S) AND ADDRESS(ES)

National Aeronautics and Space Administration
Washington, DC 20546–0001

10. SPONSORING/MONITORING AGENCY REPORT NUMBER

NASA CR—2004-213043

11. SUPPLEMENTARY NOTES

Project Manager, Steven M. Arnold, Structures and Acoustics Division, NASA Glenn Research Center, organization code 5920, 216–433–3334.

12a. DISTRIBUTION/AVAILABILITY STATEMENT

Unclassified - Unlimited
Subject Categories: 24 and 39   Distribution: Nonstandard

Available electronically at http://gltrs.grc.nasa.gov

This publication is available from the NASA Center for AeroSpace Information, 301–621–0390.

12b. DISTRIBUTION CODE

13. ABSTRACT (Maximum 200 words)

The High-Fidelity Generalized Method of Cells is a new micromechanics model for unidirectionally reinforced periodic multiphase materials that was developed to overcome the original model's shortcomings. The high-fidelity version predicts the local stress and strain fields with dramatically greater accuracy relative to the original model through the use of a better displacement field representation. Herein, we test the high-fidelity model's predictive capability in estimating the elastic moduli of periodic composites characterized by repeating unit cells obtained by rotation of an infinite square fiber array through an angle about the fiber axis. Such repeating unit cells may contain a few or many fibers, depending on the rotation angle. In order to analyze such multi-inclusion repeating unit cells efficiently, the high-fidelity micromechanics model's framework is reformulated using the local/global stiffness matrix approach. The excellent agreement with the corresponding results obtained from the standard transformation equations confirms the new model's predictive capability for periodic composites characterized by multi-inclusion repeating unit cells lacking planes of material symmetry. Comparison of the effective moduli and local stress fields with the corresponding results obtained from the original Generalized Method of Cells dramatically highlights the original model's shortcomings for certain classes of unidirectional composites.

14. SUBJECT TERMS

Micromechanics; Elastic; Effective properties; Deformation; Composites; Analysis

15. NUMBER OF PAGES

66

16. PRICE CODE

17. SECURITY CLASSIFICATION OF REPORT	18. SECURITY CLASSIFICATION OF THIS PAGE	19. SECURITY CLASSIFICATION OF ABSTRACT	20. LIMITATION OF ABSTRACT
Unclassified	Unclassified	Unclassified	